Universidade de Aveiro
2019

Departamento de Engenharia de Materiais e Cerâmica

Fátima Gabriela Guedes Faria

Novos compósitos de polioxometalatos para libertação direcionada de fármacos e terapia fototérmica

Novel polyoxometalate composites for targeted drug delivery and photothermal therapy

Universidade de Aveiro Departamento de Engenharia de Materiais e Cerâmica
2019

Fátima Gabriela Guedes Faria

Novos compósitos de polioxometalatos para libertação direcionada de fármacos e terapia fototérmica

Novel polyoxometalate composites for targeted drug delivery and photothermal therapy

Dissertação apresentada à Universidade de Aveiro para cumprimento dos requisitos necessários à obtenção do grau de Mestre em Materiais e Dispositivos Biomédicos, realizada sob a orientação científica da Doutora Filipa Lourosa Sousa, Investigadora Auxiliar do Departamento de Química da Universidade de Aveiro e co-orientação do Doutor Hélder Almeida Santos, Professor Associado da Faculdade de Farmácia da Universidade de Helsínquia

Trabalho financiado pela Bolsa de Investigação BI/UI89/7965/2017 e enquadrado nos projetos ThermoPOMs POCI-01-0145-FEDER-016714 e CICECO-Aveiro Institute of Materials, POCI-01-0145-FEDER-007679 (FCT Ref. UID /CTM /50011/2013), financiados por fundos nacionais pela FCT/MEC e cofinanciado pelo FEDER sob acordo de parceria PT2020.

“You never fail until you stop trying.”

“Genius is 1% talent and 99% percent hard work...”

Albert Einstein

o júri

presidente	Professora Doutora Maria Helena Figueira Vaz Fernandes Professora Associada do Departamento de Engenharia de Materiais e Cerâmica da Universidade de Aveiro
arguente principal	Doutor Vítor Manuel Abreu Gaspar Investigador do Departamento de Química da Universidade de Aveiro
orientador	Doutora Filipa Lourosa Sousa Investigadora Auxiliar do Departamento de Química da Universidade de Aveiro

agradecimentos

O que é que distingue uma pessoa de um animal? O que que nos distingue uns dos outros? Todos somos feitos das mesmas moléculas, dos mesmos átomos, da mesma poeira estelar. O que nos distingue é o nosso meio, as nossas pessoas. As pessoas com que falamos, com quem passamos tempo, com quem trocamos ideias, que nos influenciam e a quem nós influenciamos. Por isso, eu sou uma pessoa muito afortunada pois tenho à minha volta um conjunto de pessoas que me influenciaram e me moldaram, fazendo de mim aquilo que sou hoje, contribuindo de alguma forma no decorrer desta tese. Assim, tenho de vos agradecer, a todos, por fazerem parte “de mim”.

À Doutora Filipa Sousa, por me dar a conhecer o mundo dos polioxometalatos, por toda a orientação, por me abrir os horizontes e perspetivas, e acima de tudo, por sempre acreditar em mim.

Ao Professor Hélder Santos que me proporcionou a oportunidade de trabalhar com ele e uma fantástica equipa multidisciplinar e por me orientar no decurso desta tese, estando sempre disponível para me aconselhar e discutir novas ideias.

To Shiqi, that was always there. More than a supervisor she was my partner. Thanks for all the scientific discussions, for your availability to me and my crazy ideas, and for always listening to me and my opinions.

Ao Doutor Nuno João Silva, que apesar de não ser meu orientador “no papel” sempre o foi na realidade, estando sempre disponível para conversar. Porque uma conversa com ele às vezes vale mais do que uma aula inteira.

Ao Professor João Mano por me ter concedido acesso ao seu laser.

À Celeste, por todo o apoio e atenção prestadas.

À minha família que sempre me apoiou, por mais loucas que fossem as minhas escolhas. Em especial, ao meu pai, que por mais duro que seja por fora, está sempre sedento por um abraço ou por uns miminhos da sua filha mais velha. Que me ensinou a não me contentar com um 99%, a ser perseverante e a honrar os meus valores e aquilo em que acredito. À minha mãe, que apesar de todas as nossas diferenças e desavenças, no final do dia está sempre lá para me apoiar. Que aguenta as lágrimas no aeroporto para eu não ficar ainda mais desesperada na hora da partida. Que se sentava comigo a fazer os trabalhos de casa mesmo depois de uma noite a trabalhar. À minha mãe do coração, Lili, que sempre me acolheu em sua casa e no seu coração como se fosse sua filha do coração. Que me ensinou a não chorar por tudo e por nada e a ser uma pessoa forte e segura. Aos meus avós, Maria e Fernando, que infelizmente não resistiram para estar cá hoje, mas que continuam bem presentes no meu coração e que sei que estejam onde estiverem estarão muito orgulhosos da sua netinha. À avó Tila, que é a melhor avó do coração que podia pedir. Ao meu irmão Francisco que apesar de ser um traquinas, lá no fundo até gosta de mim e até fica feliz quando me vê. Que me deixa os cabelos em pé, mas sem o qual eu não conseguia passar. À minha irmã Beatriz, que me faz derreter com os seus abraços e os seu beijos, e que me ensinou que a família é família independentemente do sangue. À minha madrinha e ao meu padrinho, que são os “pais de Deus” e têm sido mesmo. Não podiam ser outros, não podiam ser melhores. Obrigada por serem quem são e estarem sempre presentes, independentemente de tudo.

À Dona Celeste e ao Senhor João que sempre me receberam na sua casa como se fosse a minha e me trataram como se fosse um dos seus.

Aos meus amigos, que são incansáveis e têm uma paciência do tamanho do universo. Dizem que os amigos são a família que se escolhe, e vocês sem dúvida que já pertencem à minha. À Catarina, que é uma verdadeira mulher do Norte. Não tem pelo na benta, mas é muito bonita, por fora e por dentro. Ao António, que me salva infinitas vezes sempre que ponho um pé no laboratório, que goza comigo até não se conseguir rir mais, mas que no fim está sempre lá haja o que houver. Ao Fábio, que simplesmente é o Fábio. É a pessoa mais direta e cruel que existe no mundo, mas ao mesmo tempo não deixa de ser fofinho e brincalhão. Ao João, que tem sempre uma palavra animadora e está sempre disposto a ajudar o próximo. Obrigada por terem estado sempre lá, mesmo comigo no outro lado da Europa.

À Alexandra que fez com que a minha estadia em Helsínquia fosse muito mais animada. Obrigada por toda a ajuda, por todos os passeios, por todos os momentos. Sei que és uma amiga para a vida independentemente da nossa posição geográfica.

To my roomie, Karro, the best roommate I could ever ask. Thank you for all our conversations, for teaching me about the finish culture, and above all, to be a great friend. Kiitos

Aos meus colegas de laboratório Zé, Eduardo, Rute, João, Francisca e Daniela. Obrigada por toda a disponibilidade e acima de tudo por animarem os dias no laboratório.

To my lab colleagues in Santos Lab, that made everything easier. I would like to thank specially to Patrícia, Giulia, Ariella, Jiachen, Yinggi, and Cheng.

A todos os professores que me acompanharam durante todo o meu percurso académico, incutindo-me o gosto de aprender.

Por último, mas não menos importante, ao Ricardo. Ao Ricardo que não é só o meu namorado, mas é o meu companheiro, o meu melhor amigo, o meu porto de abrigo, o meu tudo. Que me faz sentir segura e me acalma. Obrigada por estares sempre lá, mesmo nos dias mais difíceis, mesmo nos dias em que nem eu tenho paciência para me aturar a mim própria. Obrigada por seres tu, por nunca desistires de mim e por nunca me deixares desistir.

palavras-chave

Entrega direcionada, Hidrogeis; pH, Polioxometalatos; Sistemas responsivos, Temperatura; Terapia Fototérmica.

resumo

Nas últimas décadas, os hidrogéis têm atraído um enorme interesse na área biomédica, nomeadamente como sistemas de libertação direcionada e controlada de moléculas terapêuticas. Uma das propriedades mais interessantes dos hidrogéis é o facto de poderem ser preparados de forma a responder a diferentes estímulos tais como o pH, a temperatura e a concentração iónica. Esta é uma característica fundamental na libertação de compostos terapêuticos uma vez que permite o controlo da libertação do fármaco em resposta a estímulos específicos. Entre os diversos tipos de hidrogéis, os hidrogéis injetáveis capazes de se auto-recuperar têm atraído um enorme interesse devido ao seu carater minimamente invasivo e à sua capacidade de se adaptar facilmente ao local alvo. A terapia fototérmica é uma metodologia de tratamento emergente, conhecida por ser altamente efetiva, seletiva, minimamente invasiva, e capaz de eliminar diversos tipos de cancros. Tendo em vista a associação sinergética entre a libertação controlada e direcionada de moléculas terapêuticas e a terapia fototérmica, esta tese explora o desenvolvimento de um hidrogel injetável e capaz de se auto-reparar, constituído por um copolímero de quitosano (CS-g-PNIPAAm) e incorporando o polioxometalato $\{Mo_{154}\}$ como agente de conversão fototérmica. O hidrogel preparado apresentou propriedades como injectabilidade e uma auto-reparação rápida, tendo ainda mostrado ser responsivo ao pH e à temperatura na libertação de dois tipos distintos de moléculas, nomeadamente a doxorrubicina e a peroxidase de rábano silvestre. Para além disto, o hidrogel demonstrou também possuir uma grande capacidade de conversão fototérmica quando comparado com uma solução de $\{Mo_{154}\}$, causando um aumento de temperatura de cerca de 35 ºC com uma baixa irradiância (0,1 ou 0,82 W/cm^2 com um comprimento de onda de excitação de 785 ou 808 nm, respetivamente). De uma forma geral, o compósito descrito nesta tese apresenta potencialidades para aplicações que exijam uma terapia de combinação dupla, *i.e.,* terapia fototérmica e farmacológica, através de um hidrogel injetável quando é necessária uma administração *in situ*.

keywords

Hydrogels; pH; Photothermal therapy; Polyoxometalates; Responsive systems; Targeted delivery; Temperature.

abstract

In the last decades, hydrogels have attracted great interest in biomedical applications, namely as systems for targeted and controlled release of therapeutic molecules. One of the most exciting properties of hydrogels is their tunability to respond to several stimuli, such as pH, temperature, and ion concentration. In therapeutic release, this is a key feature since it enables a release triggered/ controlled by specific stimuli. Among the hydrogels, injectable and self-healing hydrogels gained special attention due to its minimally invasive character and ability to fit the target easily. Photothermal therapy is an emerging treatment methodology known to be highly effective, selective, minimally invasive and able to eliminate several types of cancers. Aiming the synergistic association of both targeted and controlled release and photothermal therapy, this thesis explores the development of a chitosan copolymer (CS-g-PNIPAAm) hydrogel incorporating the polyoxometalate $\{Mo_{154}\}$ as photothermal conversion agent.

The prepared hydrogel showed fast self-healing and injectability, as well as pH and temperature-responsiveness in the release of two distinct cargo molecules: doxorubicin and horseradish peroxidase. In addition, the developed hydrogel demonstrated to have an enhanced photothermal conversion ability when compared to a $\{Mo_{154}\}$ aqueous solution, causing a temperature increase of around 35 ºC with low irradiance (0.1 or 0.82 W/cm^2 with an excitation wavelength of 785 or 808 nm, respectively). Overall, the composite described herein can be used in applications needing a dual combination therapy, *i.e.*, simultaneous drug and photothermal therapy, delivered through an injectable hydrogel where *in situ* administration is needed.

Index

List of Abbreviations

Abbreviature	
APS	Ammonium Persulfate
ATP	Adenosine Triphosphate
ATR	Attenuated Total Reflection
BSA	Bovine Serum Albumin
CS	Chitosan
CS-g-PNIPAAm	Chitosan grafted with Poly(N-isopropylacrylamide)
DCC	N, N’-Dicyclohexylcarbodiimide
DDS	Drug Delivery System
DF-PEG	Di-functionalized Poly(ethylene glycol)
DLS	Dynamic Light Scattering
DMAP	4-Dimethylaminopyridine
DMSO-d$_6$	Dimethyl Sulfoxide-d$_6$
DOX	Doxorubicin
DSC	Differential Scanning Calorimetry
EDTA	Ethylenediaminetetraacetic Acid
EDS	Energy-Dispersive X-ray Spectroscopy
EPR	Enhanced Permeability and Retention
FBS	Fetal Bovine Serum
FDA	Food and Drug Administration
FTIR	Fourier-Transform Infrared
FTIR-ATR	Fourier-Transform Infrared – Attenuated total reflection
GSH	Glutathione
HBSS	Hank's Balanced Salt Solution

HEPES	4-(2-hydroxyethyl)-1-piperazineethanesulfonic acid
HRP	Horseradish Peroxidase
HSA	Human Serum Albumin
IVCT	Intervalence Charge Transfer
LEP	Liposome-Encapsulated Polyoxometalate
LCST	Lower Critical Solution Temperature
LVR	Linear Viscoelastic Regime
MES	2-(N-morpholino)-ethanesulfonicacid
MSNs	Mesoporous Silica Nanoparticles
MRI	Magnetic Resonance Imaging
NIPAAm	N-isopropylacrylamide
NIR	Near-Infrared
NCs	Nanoclusters
NMR	Nuclear Magnetic Resonance
NPs	Nanoparticles
PA	Photoacoustic
PBS	Phosphate Buffer Saline
PCL	Poly(ε-caprolactone)
PEG	Poly(ethylene glycol)
PLA	Poly(D-lactic acid)
PNIPAAm	Poly(N-isopropylacrylamide)
POMs	Polyoxometalates
PDT	Photodynamic Therapy
PTT	Photothermal Therapy
RT	Radiotherapeutic or Radiotherapy
ROS	Reactive Oxygen Species

SEM	Scanning Electron Microscopy
TEOS	Tetraethyl Orthosilicate
THF	Tetrahydrofuran
TPA	Two-Photon Absorption
UCNPs	Upconversion Nanoparticles
UCST	Upper Critical Solution Temperature
UV	Ultraviolet
UV-Vis	Ultraviolet-Visible
Vis	Visible
W/O	Water-in-Oil

1. Introduction

This chapter firstly introduces polyoxometalates and their relevant features, as well as provides an overview of the recent advances in their biomedical applications, namely polyoxometalate composites for cancer therapies. Secondly, the present chapter offers a comprehensive insight into fundamental concepts of hydrogels, focusing their application as drug delivery systems. Finally, a brief clarification of photothermal therapy is also made.

1.1. Polyoxometalates

Polyoxometalates (POMs) are polyanionic clusters of early transition metals (usually Tungsten, Molybdenum, and Vanadium) and oxygen, at their highest oxidation states. This family of compounds has a broad spectrum of structures and sizes, ranging from 1 to 5.6 nm.[1,2] A great diversity of other elements and molecules (organic and inorganic) can be further incorporated in POM frameworks, giving rise to an astonishing structural diversity, as well as a vast panoply of properties.[3] Moreover, their synthesis is usually straightforward and allow a fine size and shape control of the obtained materials,[4,5] high negative charges, with magnetic, redox, acidity, luminescent, and catalytic properties.[6–8]

The POM's story begins in 1826 with the discovery of the ammonium phosphomolybdate ($(NH_4)_3[PMo_{12}O_{40}]$) by Berzelius, when he noted that a crystalline solid, with a light-yellow colouration, formed upon the reaction between ammonium molybdate and phosphoric acid. The second hallmark in the history of this group of compounds occurs with Keggin in 1933 with the determination of the crystal structure of the 12-phosphotungstic acid ($[H_3PW_{12}O_{40}]$) using X-ray diffraction methods.[4] Over the years, POMs have found several applications, namely in catalysis, photocatalysis, analytical chemistry, and medicine.[1]

This section will focus mainly the classification of POMs, their preparation and some advances made regarding their application in a biomedical context.

1.1.1. Classification

This section introduces a broad classification of POMs widely used that despite their exceptions and limitations tries to clarify the relationship between the distinct building blocks, and structure types.[4,9] One issue to address is the representation of POMs structure. Since POMs are constituted by a huge number of atoms in a compact and three-dimensional structure, the representation of all bonds can become confusing and uninformative. Thus, the polyhedral representation was adopted for simplicity. In this type of representation, the metal ion is placed in the centre of a polyhedron, and its ligands are represented in the vertices. Therefore, a tetracoordinated metal is represented by a tetrahedron and a hexacoordinated metal by an octahedron.[3]

Usually, POMs are comprised of metal-oxide building blocks $\{MO_x\}$, where M corresponds to the addenda atom (typically, Mo, W, V, and sometimes Nb), O to oxygen, and x ranges from 4 to 7. The initial step for POM's formation consists of the expansion from a tetrahedral hydroxide metal complex to an octahedral hydroxide/ oxometal complex. Then, in acidic environments, the octahedral species undergo condensation reactions (Figure 1).[4]

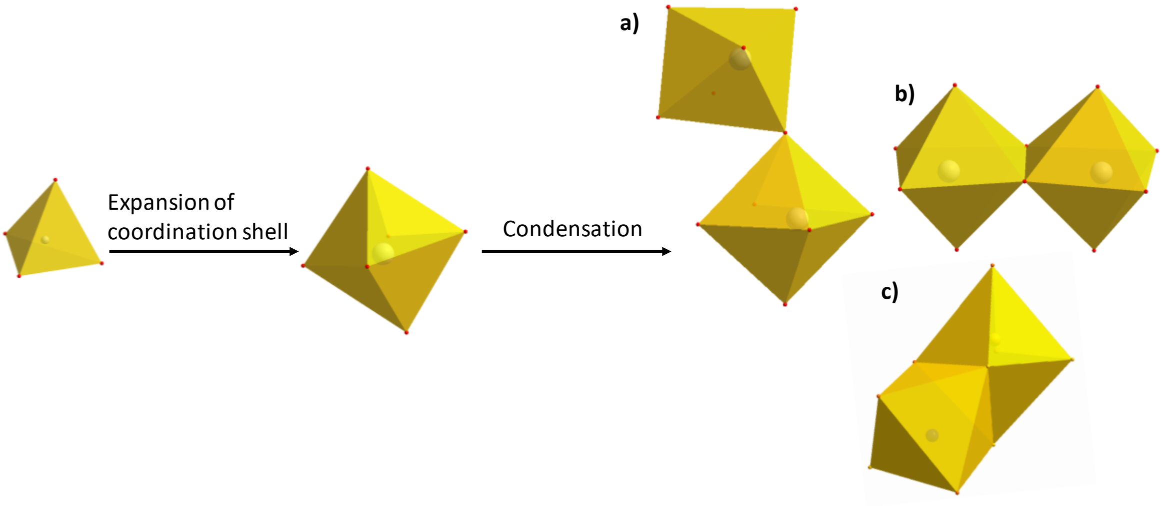

Figure 1 – Scheme illustrating the process of POMs self-assembly. Initially, the tetrahedral metal $\{MO_4\}$ expands into octahedra $\{MO_6\}$. In a further step, the octahedrons assemblies into larger clusters, sharing oxygen ligands. It exists three distinct sharing modes: (a) corner-sharing, (b) edge-sharing, and less frequently, (c) face sharing. Colour scheme: M, gold (polyhedral); O, red. Image adapted from [4].

Since POM clusters are negatively charged, they can complex with further cations, called heteroatoms. If the heteroatom plays a key role in the structure of the POM, the heteroatom is known as primary. It is not mandatory that the primary heteroatom is placed in the centre of the POM. The secondary heteroatoms are cations that fill the external vacancies in lacunary structures, originated from the partial decomposition of parent structures. Furthermore, the secondary heteroatoms can bridge several POM structures to form larger aggregates.[4]

Taking into consideration their structure, POMs can be divided into three distinct classes: heteropolyanions, isopolyanions, and giant polyoxomolybdates.

1.1.1.1. Heteropolyanions

Heteropolyanions are characterized by the presence of a metal oxide framework, where the metal is usually vanadium, tungsten, or molybdenum, and that contains heteroanions, like as PO_4^{3-}, SO_4^{2-} and SiO_4^{2-}.[2] There are three principal heteropolyanions structures:

Anderson, Keggin and Wells-Dawson. The Anderson anion $[XM_6O_{24}]^{n-}$ consists of a central heteroatom surrounded by six edge-sharing octahedra, arranged in a planar hexagon. The Keggin anion $[XM_{12}O_{40}]^{n-}$, exhibits a central tetrahedron surrounded by four trimetallic groups (M_3O_{13}) (Figure 2a). At last, the Wells-Dawson anion $[X_2M_{18}O_{62}]^{n-}$ can be seen as the combination of two lacunary Keggin anions, where one trimetallic group is removed in each unit (Figure 2b).[3] In previous formulas, M=Mo or W, and X= PO_4^{3-}, SiO_4^{2-} and SO_4^{-2}.[2]

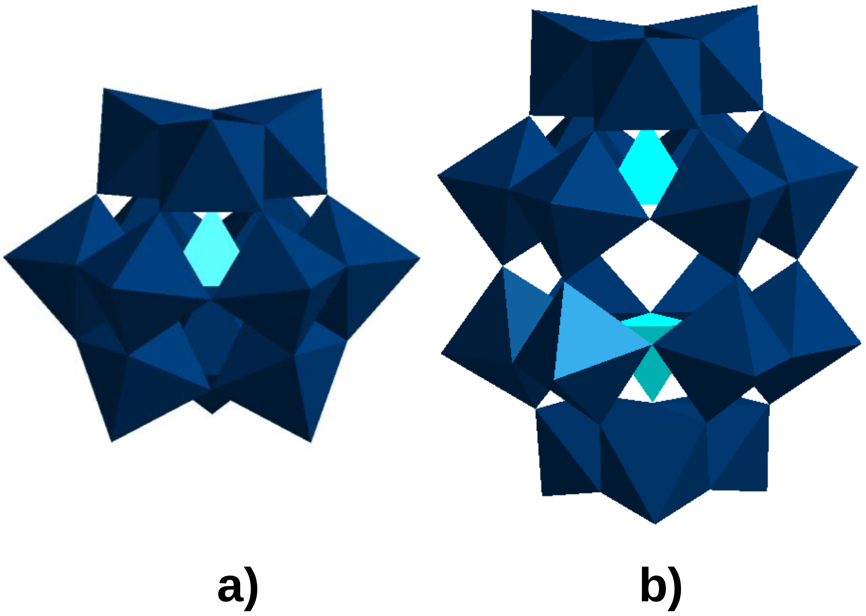

Figure 2 – Polyhedral representation of a) Keggin, and b) Wells-Dawson anions. Colour code: cyan polyhedral, {XO_n} (X=heteroatom); dark blue polyhedral, {MO_6} (M=any addenda atom).

The straightforward synthesis and stability of the heteropolyanions made this class of POMs the most popular and explored one. Its largest field of application is catalysis, with a particular focus given to the Keggin and Wells-Dawson type structures.[6] Furthermore, the high stability of tungsten-based POMs led to the development of lacunary (mono-, di-, and trilacunary) Keggin {M_{12-n}} and Dawson {M_{18-n}} anions. These lacunary POMs can be further used as building blocks for the assembly of larger aggregates, through the use of electrophiles.[9]

1.1.1.2. Isopolyanions

In comparison to heteropolyanions, isopolyanions have no internal heteroatom. Therefore, isopolyanions are less stable than their equivalent heteropolyanions and give rise to smaller clusters. Nevertheless, isopolyanions also exhibit fascinating physical properties, namely strongly basic oxygen surfaces and high charges, making them suitable for use as building blocks.[2,9]

1.1.1.3. Giant Polyoxomolybdates

Giant polyoxomolybdates were firstly described by Scheele in 1783 as molybdenum blue species.[2] However, its structure and composition remained unknown until 1995, when Müller *et al.*[10] unveiled the structure of $[Mo^{VI}_{126}Mo^{V}_{28}O_{462}H_{14}(H_2O)_{70}]^{15-}\equiv\{Mo_{154}\}$, the first member of this family. Besides this cluster, known as “big-wheel”, the family of giant polyoxomolybdates is constituted by several mixed-valence Mo-blue clusters, namely $[Mo_{256}Eu_8O_{776}H_{20}(H_2O)_{162}]^{20-}\equiv\{Mo_{256}\}$, and Mo-brown clusters, *e.g.,* $[Mo^{VI}_{72}Mo^{V}_{60}O_{372}(MeCO_2)_{30}(H_2O)_{72}]^{42-}\equiv\{Mo_{132}\}$, that presents a spherical structure. Mo-blue clusters are characterised by the delocalized Mo^{V}-Mo^{VI}; on the other hand, the Mo-brown clusters have localised Mo^{V}-Mo^{V} units.[6] The cluster of higher nuclearity, known until the moment, also belongs to the family mentioned above, and it corresponds to $[H_xMo_{368}O_{1032}(H_2O)_{240}(SO_4)_{48}]^{48-}\equiv\{Mo_{368}\}$, having a lemon shape.[2]

The basic building blocks that give rise to the diverse giant polyoxomolybdates are slightly the same, namely $\{MoO_6\}$ octahedra (abbreviated as $\{Mo_1\}$), and pentagonal $\{Mo(NO)O_6\}$ bipyramids. These two building blocks lead to other structural units, for example, $\{Mo_2\}$, $\{Mo_8\}$ and $\{Mo_{17}\}$ (Figure 3).[10,11]

Molybdenum-oxide based building blocks	Present in	Molybdenum-oxide based building blocks	Present in
 $\{Mo_1\}$	$\{Mo_{57}V_6\}$, $\{Mo_{154}\}$, $\{Mo_{176}\}$	 $\{Mo_8\}$	$\{Mo_{34}\}$, $\{Mo_{57}V_6\}$, $\{Mo_{154}\}$, $\{Mo_{176}\}$
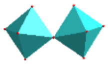 $\{Mo_2\}$	$\{Mo_{154}\}$, $\{Mo_{176}\}$	 $\{Mo_{17}\}$	$\{Mo_{36}\}$, $\{Mo_{57}V_6\}$
 $\{Mo_2'\}$	$\{Mo_{57}V_6\}$		
 $\{Mo(Mo_5)\}$	$\{Mo_{132}\}$		

Figure 3 – Polyhedral representation of the building blocks used in the assembly of the giant polyoxomolybdates: $\{Mo_1\}$ (in yellow), $\{Mo_2\}$ and $\{Mo_2'\}$ constituted by two $\{Mo_1\}$ units linked by the corners or edges, respectively (in cyan), $\{Mo(Mo_5)\}$ (five $\{MoO_6\}$ octahedra in dark-blue, and the central pentagonal bipyramid in orange), $\{Mo_8\}$ (seven $\{MoO_6\}$ octahedra in dark-blue, and the central pentagonal bipyramid in orange), and $\{Mo_{17}\}$, made of two $\{Mo_8\}$ units linked by one $\{Mo_1\}$ unit. Figure adapted from [12].

The $\{Mo_2\}$ type units are constituted by two $\{Mo_1\}$ linked by corners or edges. On the other hand, $\{Mo_8\}$ units are composed of a pentagonal $\{Mo(NO)O_6\}$ bipyramid, linked through the edges to five $\{Mo_1\}$ units. In each $\{Mo_8\}$ unit, four $\{Mo_1\}$ are connected through the corners to two further {Mo_1} units. The {Mo_{17}}≡[{$Mo_{15}(MoNO)_2O_{58}(H_2O)_2$}$_3$]$^{20-}$ type unit is formed by two {Mo_8} units connected by one {Mo_1} unit at the centre of inversion.[10,11]

{Mo_{154}}

Initially, when Müller and co-workers[10] firstly described the isolation of {Mo_{154}}, in 1995, the structural formula proposed was [$Mo_{154}(NO)_{14}O_{420}(OH)_{28}(H_2O)_{70}$]$^{(25\pm5)-}$. The preparation of this cluster consists of the acidification of an aqueous molybdate solution, followed by its reduction. The {Mo_{154}} cluster exhibits a ring-shape with an external and internal diameter of about 3.7 and 2 nm, respectively. Furthermore, the ring high/thickness is about 1.5 nm (Figure 4).[13] The {Mo_{154}} ring is constituted by 140 {Mo_1} units and 14 pentagonal {$Mo(NO)O_6$} bipyramids (Figure 4). The {$Mo(NO)O_6$} units are arranged in fourteen {Mo_8} units, connected to each other via {Mo_2} units. The constituting building blocks are organised below and above an equatorial plane: seven of the {Mo_8} units in the top plane are connected to the other seven {Mo_8} units in the bottom plane through fourteen equatorial {Mo_1} units (two for each pair of {Mo_8}).[14]

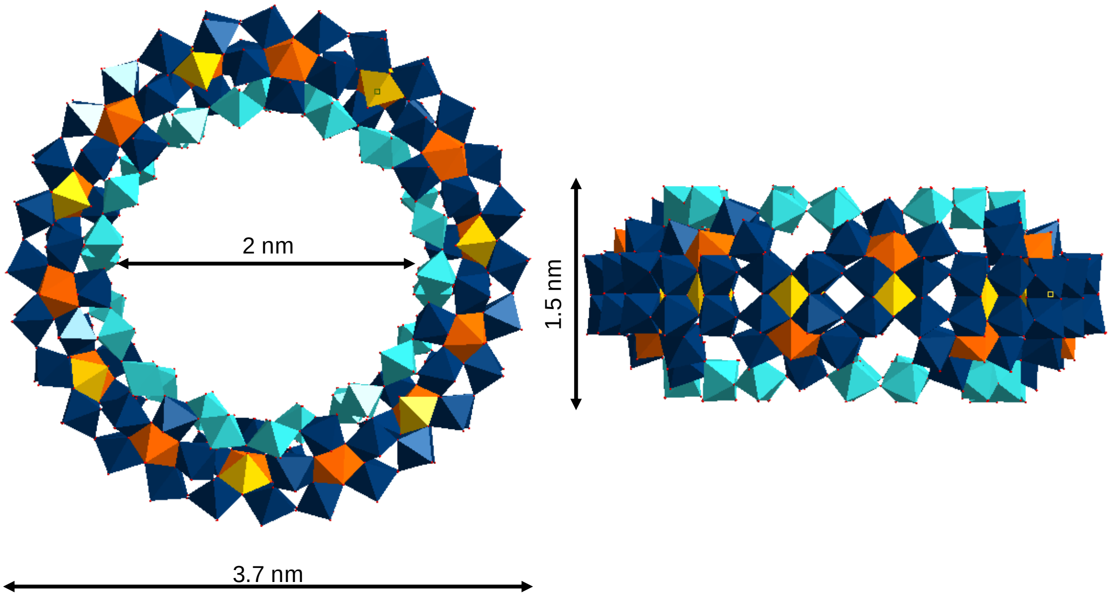

Figure 4 – Top (left) and side (right) polyhedral representation of the {Mo_{154}} cluster, accompanied by the dimensions. Colour code: {Mo_1} (in yellow), {Mo_2} constituted by two {Mo_1} units linked by the corners (in cyan), {Mo_8} (seven {MoO_6} octahedra in dark-blue, and the central pentagonal bipyramid in orange). Figure adapted from [13].

However, the method reported initially for the preparation of {Mo_{154}} presented some issues, which have hindered the isolation of pure compounds or even single crystals by other chemists. To surpass this, in 1999, Müller and his team,[15] reported a simple synthetic route based on the use of a solution with a high electrolyte concentration and the use of sodium dithionite as reducing agent.

$Na_{15}[Mo^{VI}_{126}Mo^{V}_{28}O_{462}H_{14}(H_2O)_{70}]_{0.5}\cdot[Mo^{VI}_{124}Mo^{V}_{28}O_{457}H_{14}\cdot(H_2O)_{68}]_{0.5}\cdot$ca. 400 H_2O ≡ Na_{15}[**1a**]$_{0.5}$[**1b**]$_{0.5}\cdot$ca. 400 H_2O **(1)**

The compound obtained (**1**) was isolated as a mixed-crystal, in which the crystal lattice is composed by two discrete ring-shaped clusters: $\{Mo_{154}\}\equiv$**1a** and $\{Mo_{152}\}\equiv$**1b**, in the proportion 1:1. The structure of the $\{Mo_{154}\}\equiv$**1a** is similar to that described initially,[10] except for the case of the $\{Mo_8\}$ type units. In these building blocks, the central pentagonal-bipyramidal $\{Mo(NO)O_6\}$, is replaced by central pentagonal-bipyramid $\{MoO_7\}$ leading to the formation of a unit $\{Mo_8O_{28}(H_2O)_3\}\equiv\{Mo_8\}$. The structure of anion **1b**, is almost the same as the **1a**, differing only in the presence of a defect on the former, due to the absence of one $\{Mo_2\}$ unit.[15] Thus, in terms of building blocks the independent ring-shaped clusters $\{Mo_{154}\}\equiv$**1a** and $\{Mo_{152}\}\equiv$**1b**, can be expressed as: $[\{Mo_2\}_{14-x}\{Mo_8\}_{14}\{Mo_1\}_{14}]^{(14+2x)-}\equiv[\{Mo^{VI}_2O_5(H_2O)_2\}^{2+}_{14-x}\ \{Mo^{VI/V}_8O_{26}(\mu_3\text{-}O)_2H\cdot(H_2O)_3Mo^{VI/V}\}^{3-}_{14}]^{(14+2x)-}$, where x corresponds to the number of defects, taking the value of 0 or 1, for $\{Mo_{154}\}\equiv$**1a** and $\{Mo_{152}\}\equiv$**1b**, respectively.

$\{Mo_{57}V_6\}$

If an acidified molybdate aqueous solution is reduced in the presence of transition metals ions such as V^{IV} and Fe^{II}/Fe^{III}, $\{Mo_{57}M_6\}$-type clusters are formed. In these $\{Mo_{57}M_6\}$-type species, the M_6 units are occupied by transition metal ions, such as $\{V^{IV}(H_2O)O\}^{2+}$, $\{Fe^{III}(H_2O)_2\}^{3+}$, $\{Fe^{II}(H_2O)_2\}^{2+}$, and $\{Cu^{II}(H_2O)_2\}^{2+}$.[11]

The doughnut-shaped cluster $(NH_4)_{21}[\{V^{IV}(H_2O)O\}_6\{Mo^{V}(\mu\text{-}H_2O)_2(\mu\text{-}OH)Mo^{V}\}_3\{Mo_{15}(MoNO)_2O_{58}(H_2O)_2\}_3]\cdot 65H_2O\equiv\{Mo_{57}V_6\}$, is formed when the M_6 are $\{V^{IV}(H_2O)O\}^{2+}$ type units.[11] Its structure is constituted by three $\{Mo_{17}\}$ building blocks, which are linked through six $\{V^{IV}(H_2O)O\}^{2+}$ units and three $\{Mo^{V}(\mu\text{-}H_2O)_2(\mu\text{-}OH)Mo^{V}\}^{9+}$ units (Figure 5).[11,14,16–19] The $\{Mo^{V}(\mu\text{-}H_2O)_2(\mu\text{-}OH)Mo^{V}\}^{9+}$ units are built of two face-sharing $\{Mo_1\}$ units.[16]

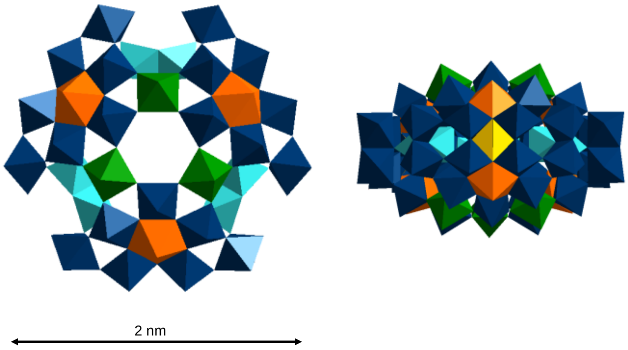

Figure 5 – Top (left) and side (right) polyhedral representation of $\{Mo_{57}V_6\}$. This anion is constituted by three $\{Mo_{17}\}$ units ($\{Mo_1\}$ units in dark-blue, and the central pentagonal $\{Mo(NO)O_6\}$ bipyramid in orange) linked through three $\{Mo^{V}(\mu\text{-}H_2O)_2(\mu\text{-}OH)Mo^{V}\}^{9+}$ units (made of two face-sharing $\{Mo_1\}$ units), in cyan, and six $\{V^{IV}(H_2O)O\}^{2+}$ units, in green.

1.1.2. Electronic Properties

As stated previously, {Mo_{154}} and {$Mo_{57}V_6$} share most of their constituting building blocks. Thus, these two POMs exhibit a great similarity at the structural level, determining a great similarity in their electronic behaviour. {Mo_{154}} have {Mo_8} and {Mo_1} units in its constitution, among which are located the (incomplete) double-cubane-type compartments, highlighted in Figure 6. These (incomplete) double-cubane type compartments are constituted by five Mo centres belonging to {Mo_8} and {Mo_1} units, and six O atoms (denoted as {Mo_5O_6}), carrying two delocalized 4d electrons.[20]

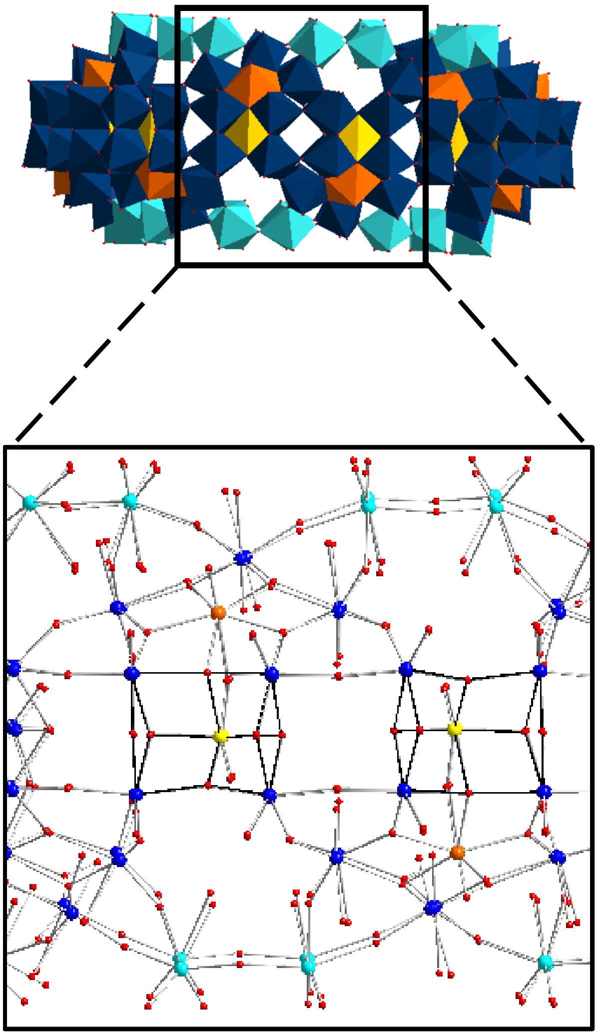

Figure 6 – Polyhedral representation of {Mo_{154}}. The ball-and-stick representation (bottom) highlights two of the 14 (incomplete) double-cubane-type compartments which comprise five Mo centres belonging to {Mo_8} and {Mo_1} units, and six O atoms. Colour code: {Mo_1} (in yellow), {Mo_2} (in cyan), {Mo_8} (in orange), and {MoO_6} octahedra (dark-blue). Figure adapted from [12].

The “big-wheel” exhibits 14 (incomplete) double-cubane type compartments, where the delocalized electrons suffer intervalence charge transfer (IVCT) ($Mo^V \rightarrow Mo^{VI}$), belonging to the class III on the Robin-Day classification. This IVCT is responsible for the presence of two characteristic bands in its Vis (Visible) – NIR (Near Infrared) spectrum: one at about 745 nm, that is responsible for its' characteristic dark-blue colour, and another at 1070 nm.[21] On the other hand, as it is possible to observe in Figure 7, $\{Mo_{57}V_6\}$ has three $\{Mo^V(\mu\text{-}H_2O)_2(\mu\text{-}OH)Mo^V\}^{9+}$ (or $\{Mo_2\}$) type units and its Vis-NIR spectrum exhibits two peaks at 560 and 840 nm corresponding to IVCT transitions.[16,17]

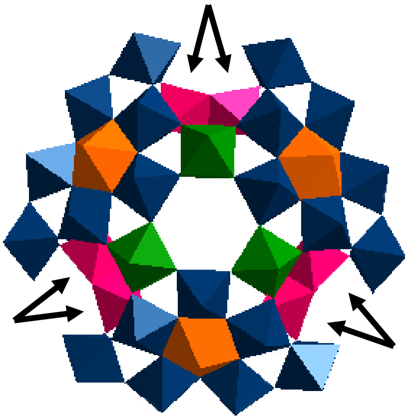

Figure 7 – Polyhedral representation of $Mo_{57}V_6$ highlighting the Mo^V units with arrows. Colour code: $\{MoO_6\}$ octahedra (dark-blue), $\{Mo_2\}$ (in pink), $\{Mo_8\}$ (in orange), and $\{V^{IV}(H_2O)O\}^{2+}$ units (in green).

Thus, it is expected that when irradiated with NIR-light, these POMs will absorb energy and cause a temperature increase due to the IVCT between $Mo^V \rightarrow Mo^{VI}$.

1.1.3. Biomedical Applications

In the context of POM biological applications, the first report of the *in vivo* antitumor activity of POMs dates back to 1965, describing the use of a mixture of $H_3[PW_{12}O_{40}]$, $H_3[PMo_{12}O_{40}]$, and caffeine on patients with gastrointestinal cancer.[22] Similarly, in 1974, Jasmin *et al.*[23] reported the inhibition of sarcoma virus-induced tumours by $(NH_4)_{17}Na[NaSb_9W_{21}O_{86}]$. Since then, the biomedical properties of this class of metal-oxide clusters has been widely explored.[24] In addition to its antitumor activity, it was also reported the antiviral (namely anti-HIV activity)[25–28] and antibacterial[29–32] activity, as well as the insulin-mimetic effect, to control diabetes mellitus,[32–34] and inhibition of Aβ aggregation in Alzheimer disease.[35–37]

Thus, the last years have witnessed significant advances in the development of bioactive POMs, and its synergistic use with other materials and/or drugs. Due to its impact in society, cancer is among the most studied diseases and, therefore, there is a boundless search for its treatment. In this section, are described recent reports focusing on drug delivery systems, antitumor activity and cell toxicity of POM related materials. In addition, the development of POMs based photothermal materials are also addressed.

1.1.3.1. Delivery of POMs with Antitumoral Activity

In vitro and *in vivo* studies have evidenced that several POMs and POM-hybrid systems exhibit antitumoral activity. However, there is no clear correlation between POM's antitumoral activity and its structural/ chemical characteristics. Therefore, it is difficult to predict the bioactivity of a given POM. Moreover, the mechanisms behind the POM-mediated antitumoral activity remains unexplained. Owing to their structural/ chemical diversity, POM-based systems may have several possible mechanisms for tumour inhibition instead of a strict mechanism.[24]

The main approaches used for the delivery of POMs with antitumoral activity consist in their encapsulation in drug carriers such as liposomes, silica, and biopolymers. Besides, novel approaches have emerged based on the organisation of POMs in nanoparticles or the conjugation of the bioactive POMs with biomolecules.

POMs Encapsulation

Although having unique characteristics, POMs present some drawbacks such as their highly negative charge and size, cell toxicity and instability in the water at physiological pH, which can lead to their degradation. An approach adopted to mitigate these issues is encapsulating/embedding the POM in a drug carrier, such as liposomes[38] and biopolymers.[39–43] Besides enhancing the stability in physiological conditions and biocompatibility, consequently reducing cell toxicity, this kind of approach also attempts to improve the anticancer activity.

Wang and co-workers[38] developed a method for the synthesis of liposome-encapsulated polyoxometalate (LEP) nanoparticles (NPs), where they used $K_6SiW_{11}TiO_{40}$, known for its high antitumor activity. The $(SiW_{11}Ti)$LEP NPs exhibited an enhanced cell-membrane penetration, stability, and antitumoral activity in KB and HeLa cancer cell lines. Furthermore, the toxicity of the encapsulated POM diminished relatively to the naked POM, when administrated against HL-60 tumours *in vivo*.

Until today, different POMs were encapsulated using different biopolymers, particularly in starch,[39] chitosan,[40,41,43] and gelatine.[42] One example is the encapsulation of α-$K_8H_6[Si_2W_{18}Ti_6O_{77}]$ ($Si_2W_{18}Ti_6$) in starch, using a water-in-oil (W/O) emulsion approach.[39] The resulting $Si_2W_{18}Ti_6$@starch NPs revealed improved stability, antitumoral activity, and the ability to extend the survival time of the mice.

Menon and co-workers[43] reported the complexation of $[Eu_6As_6W_{63}O_{218}(H_2O)_{14}(OH)_4]^{25-}$ (EuWAs) with chitosan. The EuWAs-chitosan composite exhibited a sustained and slow release profile at physiological pH, as well as enhanced anticancer activity in several cancer cell lines (KB, MCF-7, PC-3, and A549). Another example reporting the formation of a POM-chitosan nanocomposite was reported by Pandya and Joshi.[41] In this work, $K_6H[CoW_{11}O_{39}(CpTi)]\cdot 13H_2O$ ($CoW_{11}CpTi$) was conjugated with biocompatible chitosanYC-100 (CSYC100) through electrostatic interactions. The resulting nanocomposite exhibited a slow-releasing profile of the POM during 11 h, reaching a release of 98% at the end. Relatively to the bare POM, the $CoW_{11}CpTi$-CSYC100 composite exhibited lower toxicity on C2C12 cells (healthy mouse myoblast cell line). Similarly, the assay with A549 cells (lung cancer cell line), revealed a less toxic behaviour from $CoW_{11}CpTi$-CSYC100 composite, showing an increase in cell viability from 10 to 55%.

The encapsulation of $K_6H_2[CoW_{11}TiO_{40}]\cdot 13H_2O$ in chitosan derivatives was reported by Geisberger *et al.*,[44] via electrostatic interactions with carboxymethyl chitosan and trimethyl chitosan (TMC). This study proved the influence of the polymeric matrices charge in the morphology and size of the formed nanocomposites, which ultimately may influence the extent of cellular uptake. The release profile of the POM cluster from the TMC-POM nanocomposite was also evaluated, exhibiting a quicker release (around 10%), in the first 3-4 h, which can be related with its anti-tumoral activity in the first five hours of treatment. Moreover, the prepared nanocomposites exhibited enhanced anti-tumoral activity regarding the pristine POM cluster, which can be ascribed to the higher stability at pH 7.4. Similarly, Shah and collaborators[45] encapsulated three distinct Keggin-type anions, namely $[PW_{12}O_{40}]^{3-}$, $[TiW_{11}CoO_{40}]^{7-}$, and $[Ti_2PW_{10}O_{40}]^{7-}$, in chitosan by ionic gelation. The encapsulated POMs exhibited enhanced antitumor activity towards HeLa cells when compared to the pristine POMs. Furthermore, they found that the chitosan-$TiW_{11}Co$ composite was the most suitable as a potential drug for cancer treatment. Another study following the same approach was described recently by Pérez-Álvarez and co-workers.[46] In this case, nanogels were initially prepared by covalent cross-linking of chitosan with poly(ethylene glycol bis(carboxymethyl)ether) and then allowed to swell in the presence of a solution containing the Wells-Dawson type $[P_2Mo_{18}O_{62}]^{6-}$ phosphomolybdate. The POMs were loaded due to electrostatic interactions between the $[P_2Mo_{18}O_{62}]^{6-}$ anion and the protonated amine groups in chitosan. The prepared nanogels presented a pH-controlled release of the POM cluster, exhibiting release at pH 4.0 and 5.0 but not at 7.4. This approach differs from the previous examples due to the introduction of the covalent cross-linking, which intended to confer improved stability to the nanomaterials. The cytotoxicity and antitumoral activity were not evaluated in this study.

In a distinct study, Guo et al.[42] prepared gelatine/heptamolybdate (HM) hybrid NPs through electrostatic interactions between the anionic HM and the zwitterionic gelatine, dispensing the use of surfactants or organic solvents. The obtained hybrids exhibited a high loading efficiency of the POM (about 70%), and the ability for size tuning. Moreover, the gelatine/HM hybrid presented enhanced antitumor activity when compared to that of an ammonium heptamolybdate aqueous solution, both *in vitro* (Human gastric cancer cell lines BGC-823), and *in vivo* (in H_{22} hepatoma bearing ICR mice).

Two additional studies related to the preparation of responsive hydrogels with lacunary Wells–Dawson anion $[P_2W_{15}O_{56}]^{12-}$ ($\{P_2W_{15}\}$) were reported by Azizullah and co-workers.[47,48] The first study[47] consisted in the preparation of gelatine-POM self-assembled hydrogels, using acrylic acid as a pH-responsive monomer. In a further work,[48] $\{P_2W_{15}\}$-chitosan hydrochloride hydrogels were prepared. The prepared materials exhibited an electrostatically driven pH-responsive behaviour, and both free and embedded POM presented similar dose-dependent toxicity in both cancer cell lines tested (MCF-7 and HeLa), and minimal toxicity on healthy cells (Vero). Furthermore, *in vivo* assays indicated that prepared hydrogel is safe and tolerable. The only adverse effect was the reduction in blood glucose level.

Besides liposomes and biopolymers, POMs (specifically, $K_2Na[As^{III}Mo_6O_{21}(O_2CCH_2NH_3)_3]\cdot 6H_2O$) were also doped in silica nanospheres.[49] In this study, the composite was prepared by the W/O microemulsion method, and the obtained POM@SiO_2 nanospheres exhibited a uniform size (~40 nm) and a slow-release profile in phosphate buffer saline (PBS) solutions during 60 h, at pH 7.4 and 5.5. The *in vitro* assays (MCF-7 cell line, a human breast adenocarcinoma cell line) of POM@SiO_2 revealed improved antitumor activity when compared to the pure POM, which may be due to the surface modification imparted by the silica shells. Flow cytometry analysis unveiled that POM@SiO_2 could induce apoptosis by cell cycle arresting in S phase, and analysis by western blot suggested that the apoptosis was caused by the inhibition of Bcl-2 protein. Furthermore, from the study of interactions between POM@SiO_2 and human serum albumin (HSA), it was inferred that the polyoxometalate doped silica nanospheres were able to bind to HSA and change its conformation. This finding indicates that the POM@SiO_2 can be transported in HSA.

Karimian and co-workers,[50] reported the synthesis of a novel POM $(TBA)_4H_3[GeW_9V_3O_{40}]$, with antitumoral activity against a glioblastoma cell line (U87), and developed a novel multidrug delivery system using mesoporous silica nanoparticles (MSNs) as drug carriers (Figure 8). In this work, the MSNs pores were capped by the POM bearing a tracking fluorophore, through a disulphide bond which is redox-responsive and, therefore, cleaved by glutathione (GSH). The hydrolysis of the disulphide bond leads to the release of the drug entrapped in the MSN pores, in this case, doxorubicin. The presence of the fluorophore attached to the POM and the use of doxorubicin (DOX), allowed the cellular tracking of both POM and DOX. This dual drug delivery system exhibited better performance than the free doxorubicin against U87 cells.

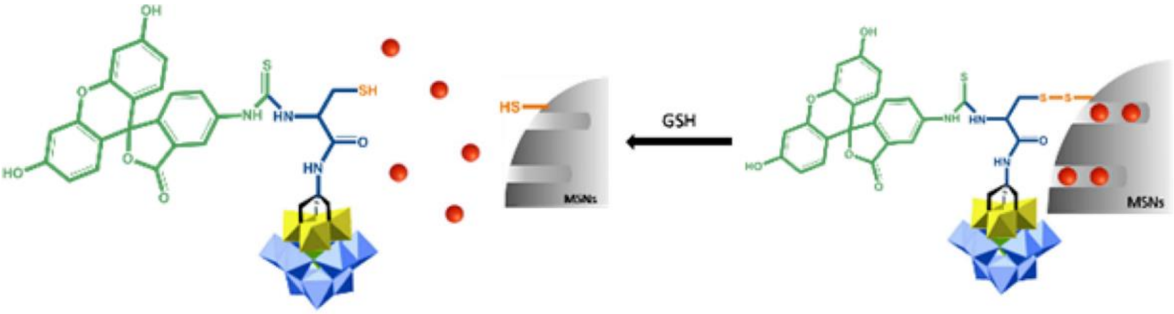

Figure 8 – Schematic representation of disulphide bond established between MSNs and the POM, and its hydrolysis by GSH, leading to the release of DOX (red spheres) entrapped in the MSN pores, and POM bearing a tracking fluorophore. Image reprinted from [50].

Another approach using MSNs to encapsulate a POM with antitumoral activity was described by Sun *et al*.[51] In this study, the $K_8H_2[Ti(H_2O)]_3SiW_9O_{34}$ cluster was encapsulated in two different types of MSNs: MCM-41-type mesoporous silica nanospheres and bimodal mesoporous silica microspheres functionalized with amino groups. The systems developed exhibited a pH-controlled release, showing a burst release of the POM under mild alkaline pH and no release in acidic conditions. Moreover, the encapsulation of the $K_8H_2[Ti(H_2O)]_3SiW_9O_{34}$ cluster improved its antitumor activity. A novel encapsulation strategy was followed by Azizullah and co-workers,[52] who developed a hydrogel composed of polyethyleneimine and the Wells-Dawson-type anion $[P_2W_{15}O_{56}]^{12-}$. Initially, polyacrylic acid was grafted on the polyethyleneimine backbone, to impart pH-responsive properties. Then, the grafted polymer was cross-linked by electrostatic interactions between the $[P_2W_{15}O_{56}]^{12-}$ anion and the amine groups in polyethyleneimine. The release was tested at pH 1.2 and 7.4 having been verified a pH-responsive release with maximum release at pH 7.4. Moreover, the cytotoxicity of the pristine POM and the hydrogel were assessed, and both revealed dose-dependent toxicity against MCF-7 and HeLa cells. The POM exhibited higher toxicity against HeLa cancer cells than doxorubicin, killing a higher number of cells in almost all concentrations. However, the pristine POM exhibited higher toxicity to Normal Vero cells than doxorubicin. Regarding this, a deeper investigation of the anticancer activity and selectivity of this compound is needed.

POM Nanoparticles

Recently, Li *et al.*[53] synthesised nanoparticles, by the freeze-drying method, with the following POMs: $(NH_4)_{11.9}[Nd_{4.7}(MoO_4)(H_2O)_{23}(Mo_7O_{24})_4]\cdot19H_2O$, $(NH_4)_{28}[Ce_8(MoO_4)_2(H_2O)_{31}(Mo_7O_{24})_8]\cdot74H_2O$, $(NH_4)_{11.9}[Pr_{4.7}(MoO_4)(H_2O)_{23}(Mo_7O_{24})_4]\cdot34H_2O$ and $(NH_4)_{26}[CoPr_8(MoO_4)_2(H_2O)_{31}(Mo_7O_{24})_8]\cdot54H_2O$. These NPs exhibited an average diameter of 50 ± 5 nm, improved cytotoxicity and lower side effects against six human cancer cells lines, compared to the respective POMs. These results open new opportunities concerning the production of POM NPs for biomedical applications. Furthermore, this study provides an insight into the improvement of the anti-cancer activity of the pristine POMs by its delivery as NPs.

Conjugation of POMs with Biomolecules

Aiming at the improvement of the delivery of POMs with antitumoral activities, Yang *et al.*[54] reported a new concept based on the conjugation of the amine grafted cluster $[MnMo_6O_{18}[(OCH_2)_3CNH_2]_2]^{3-}$ with biomolecules such as cholic acid, dehydrocholic acid, O-succinyl-cholesterol, 6-O-(3-carboxypropanoyl)-1,2:3,4-di-O-isopropylidene-b-D-galactopyranose, and adipic acid. The cell viability of all conjugates was evaluated in three distinct cell lines: two breast cancer cell lines (MCF-7 and MDA-MB-231) and a noncancerous breast epithelial cell line (MCF-10A). Overall, the POM-biomolecule hybrid exhibited increased antitumoral activity and lower toxicity for the normal cells. Despite, the conjugates with colic acid and dehydrocholic acid stood out, presenting an enhanced antitumoral activity and selectivity.

1.1.3.2. POMs as Building Blocks for the Design of Novel Drug Carriers

Ideal drug carriers must have a high loading efficiency.[55] Therefore, since 3D hierarchical structures exhibit high loading ability, they have potential as drug carriers. Having this in mind, Li and co-workers,[56] reported the preparation of flowerlike 3D hierarchical nanostructures through the co-assembly of dopamine and phosphotungstic acid, mainly through hydrogen bonds and electrostatic interactions. By varying the ratios of the initial components, their concentration and pH of the initial solution, it is possible to tune the size and morphology of the obtained particles. The release profile of doxorubicin from the flowerlike nanocarriers exhibited a pH-dependent behaviour, making them a potential drug carrier for the treatment of some cancers.

1.1.3.3. POMs in Photothermal Cancer Therapy

Photothermal therapy (PTT) is an emerging method for cancer “treatment” that converts the energy from an external electromagnetic field into thermal energy, leading to thermal ablation of cancer cells and culminating in his death.[57] Comparatively to visible and ultraviolet light, NIR light exhibits a deeper tissue penetration and causes relatively low damage.[58] Therefore, there has been a high demand for the development of novel NIR-absorbing photothermal agents. In this scope, four different POMs seem to be very promising PTT agents, namely $[GdW_{10}O_{36}]^{9-}$,[59] $[PMo_{12}O_{40}]^{3-}$,[60–62] $[PMo_2W_{10}O_{40}]^{5-}$,[63] and the big-wheel $\{Mo_{154}\}$.[64]

The anion $[GdW_{10}O_{36}]^{9-}$ ($\{GdW_{10}\}$) was the first POM applied as photothermal agent, and its use was described by Yong et al.[59] In this work, $\{GdW_{10}\}$ was coated with bovine serum albumin (BSA), forming BSA@GdW_{10} nanoclusters (NCs). The *in vivo* toxicity studies suggested that the BSA@GdW_{10} NCs present low toxicity and efficient renal clearance. Furthermore, it was also verified that the prepared NCs exhibit enhanced CT (computed tomography)/MR (magnetic resonance) imaging signals and provoked notable PTT and radiotherapeutic (RT) effects on tumour cells.

Keggin anions such as $[PMo_{12}O_{40}]^{3-}$ were used in three distinct approaches aiming at eradicating tumour cells. In an initial study, Zhang and co-workers[60] developed a system where the acidic tumour microenvironment is used to induce the protonation of the POM, leading to the formation of larger vesicles produced by the self-assembly of several POM mediated by hydrogen bonds (Figure 9). Thus, the $[PMo_{12}O_{40}]^{3-}$ clusters can initially circulate in the bloodstream (due to its small dimensions ~ 1 nm) and show an enhanced accumulation in the tumour due to the formation of large aggregates (tens of nanometres) (designated by “small-big” approach). Moreover, the acidic and reductive tumour microenvironment enhances the photothermal conversion due to the reduction of the $[PMo_{12}O_{40}]^{3-}$ anion, making the photo-hyperthermia specific for the tumour.

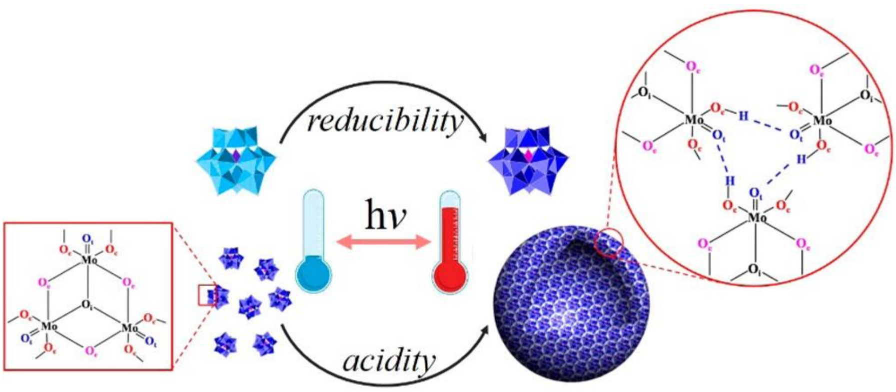

Figure 9 – Schematic representation of the proposed mechanism for the POM self-assembly into larger aggregates, induced by the low pH in the tumour microenvironment. Image reprinted from [60].

In a subsequent study, Ni and collaborators,[61] used the same idea and combined it with photoacoustic (PA) imaging, to allow an imaging-guided PTT. PA imaging is a valuable technique since it combines the high sensitivity of optical imaging and high resolution of ultrasound imaging, being usually combined with PTT because they both use NIR absorbing materials. Both *in vitro* (human embryonic kidney 293 (HEK293) and murine breast cancer 4T1 cells) and *in vivo* (4T1 tumour-bearing mice) assays unveiled the efficacy of the system. In a different study, Xu *et al.*[62] encapsulated $NaGdF_4$:Yb,Er@$NaGdF_4$:Nd,Yb upconversion nanoparticles (UCNPs) in a silica shell doped with Mn^{2+} ions. Keggin anion $[PMo_{12}O_{40}]^{3-}$ and doxorubicin (DOX) were subsequently embedded in the silica shell. In this way, upon NIR light irradiation and in the presence of the acidic and reductive tumour microenvironment, the silica shell is degraded, and DOX released in the tumour. The degradation of silica shell leads to a decrease of the nanocarriers' size, which allows the nanoparticles to penetrate deeper in the tumour, thus improving its eradication. When irradiated with a NIR laser, the UCNPs-DOX exhibits tri-modal imaging capabilities: CT, magnetic resonance imaging (MRI), and upconversion luminescence, derived from $Gd^{3+}/Yb^{3+}/Nd^{3+}/Er^{3+}$. Moreover, the presence of the POM in the system enables the PTT of the tumour upon NIR-light irradiation. Moreover, the *in vitro* biocompatibility assays (L929 fibroblast cells) showed that both POM and the developed nanosystems exhibited low toxicity. The anticancer efficacy was also evaluated (HeLa cells and U14 tumour-bearing mice) and, as expected, the nanoparticles containing both POM and DOX exhibited the highest antitumoral activity. A distinct POM that also exhibits a strong NIR absorption, $[(CH_3)_4N]_5[PMo_2W_{10}O_{40}]$, was used by Yan and co-workers,[63] aiming the simultaneous PTT and PA imaging of tumours. Similarly to the described previously for the encapsulation of POMs in drug carriers, in this work, $[(CH_3)_4N]_5[PMo_2W_{10}O_{40}]$ was loaded in the core of polymeric (P_4VP-b-PEO) nanoparticles. Cell assays exhibited low toxicity (in L929 cells) and good photothermal effect *in vitro* (in 4T1 tumour cells). The assays of PA imaging *in vivo* (in 4T1 tumour mice model) verified the targeting ability (due to EPR effect) and the improved PA signal (about ten times). Moreover, it was obtained a good PTT efficacy *in vivo*.

The strong absorption of the giant molybdenum blue $\{Mo_{154}\}$ in the NIR region makes it a suitable candidate for the development of PTT materials. In this regard, $\{Mo_{154}\}$ anion was used as a photothermal agent to prepare a dendritic nanocomposite (<10 nm) that combines the photothermal-chemotherapy effects.[64] The $\{Mo_{154}\}$ anion was encapsulated with a cationic dendritic surfactant (D-3), forming micellar particles ($D_{15}Mo_{154}$). The encapsulation within a micelle imparts some advantageous properties to $D_{15}Mo_{154}$ complex, namely increased biocompatibility and stability by avoiding unspecific interactions with biomolecules, ability to load drug molecules (DOX) and thermo-triggered drug release. The *in vitro* assays with human hepatocyte cells (QSG-7701) exhibited low cytotoxicity of the $D_{15}Mo_{154}$ complex alone (without laser and DOX). As expected, the $D_{15}Mo_{154}$@DOX complex irradiated with a NIR laser leads to a higher reduction of cell viability, when compared with the results obtained for $D_{15}Mo_{154}$ + laser and $D_{15}Mo_{154}$@DOX, thus indicating the synergistic effect of the PTT and controlled drug release. Furthermore, the *in vivo* assays were performed in female nude mice bearing 4T1 murine breast tumours and showed that the treatment using $D_{15}Mo_{154}$ with and without DOX, upon laser irradiation, presents the best therapeutic effect.

1.2. Hydrogels

The term “hydrogel” denotes a three-dimensional (3D) network formed by cross-linked polymer chains that can swell and hold a large amount of water.[65,66] Hydrogels can be prepared from a great variety of polymers, either synthetic or natural, and its properties can be further tuned for specific applications, endowing this class of materials with uses in a multitude of fields, from soft electronics,[67,68] sensors,[69–71] actuators,[72,73] and biomedicine.[74–76] The story of hydrogels in biomedicine has its onset in the early 60s when Wichterle and Lím[77] firstly reported a synthetic hydrogel for biological use.

Hydrogels are known to exhibit up to 99.9% of water content, relatively low toxicity, excellent biodegradability, and mucoadhesive and bio-adhesive properties.[78,79] Moreover, hydrogel-based drug delivery systems (DDS) allow the concomitant delivery of several drugs at the target site with a relatively high concentration in a sustained way and with reduced toxicity, thus avoiding the drug circulation in the whole body. For these reasons, hydrogels are known to be excellent DDS for targeted therapy, overcoming some of the major drawbacks of traditional oral and intravenous drugs (*e.g.,* rapid metabolism, undesirable drug absorption and distribution, and poor bioavailability).[80]

One of the most exciting properties of hydrogels is the fact that they can be tuned to respond to several stimuli, such as pH, temperature, and ion concentration.[78,79] The properties mentioned above make hydrogels suitable for the development of therapeutic delivery systems and their use in tissue engineering.[79] Traditional hydrogels show big limitations in what it concerns their surgical implantation and all possible issues associated with it, such as infection, pain and scarring. Thus, in the last years, a great interest has arisen in the development of injectable hydrogels due to its minimally invasive character and ability to easily fit the target.[79]

This section aims to give a comprehensive understanding about the basic concepts of hydrogels, from its formation mechanism and classification to the principles of injectability and self-healing mechanisms. Finally, their application as stimuli-responsive DDS is briefly addressed.

1.2.1.Classification of Hydrogels

Hydrogels can be classified according to a multiplicity of parameters, such as physical structure, ionic charge, synthetic route, source, size, cross-linking, mechanical and structural characteristics (Figure 10).[81] Being the most widely used classification based on the cross-linking strategy, this thesis explores only this one.

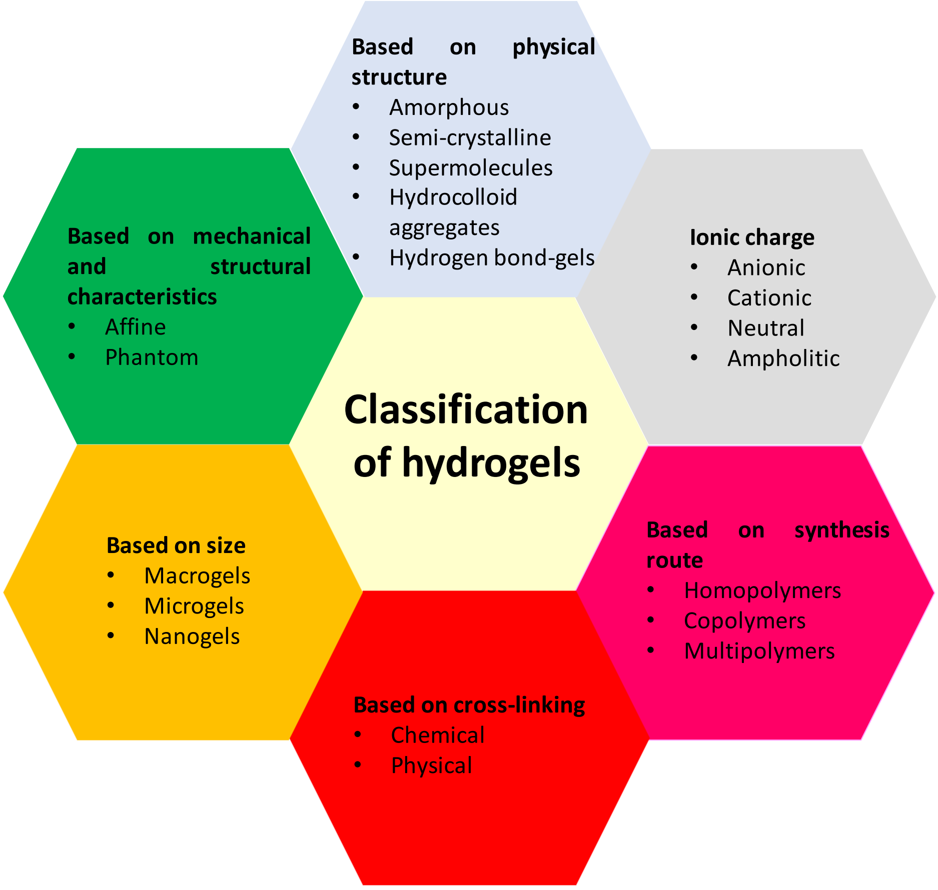

Figure 10 – Classification of hydrogels based on distinct parameters.

The process of hydrogel formation is denominated gelation or sol-gel transition. Gelation consists of the linking of polymer chains together, leading to the formation of larger branched polymer chains. Initially, these branched polymers are still soluble and polydisperse, and this mixture is usually known as ‘sol’. As the linking process continues, the branched polymer is increasing in size with a concomitant decrease in solubility. Then, an ‘infinite polymer’, called ‘gel’ or ‘network’ is formed by finite branched polymers.[82,83]

Gelation takes place mainly in two ways: physical or chemical cross-linking,[83] which will be briefly described in the following sections.

1.2.1.1. Physical Cross-linking

Nowadays, physically cross-linked hydrogels, also known as reversible gels, are receiving significant attention due to its easy preparation and absence of chemical cross-linking agents, depending on the intrinsic properties of the polymer.[66,84] The physical cross-linking of hydrogels usually takes place through molecular entanglements and/or secondary bonds, such as hydrogen bonds, ionic/ electrostatic interactions, and hydrophobic/ hydrophilic interactions. This type of cross-linking can also take place by crystallisation/stereo complex formation, metal coordination and π-π staking.[85] Due to the nature of these interactions, they are reversible and can be disrupted by variations in physical conditions (such as pH, temperature, and ionic strength of the solution) or by stress application.[83,86] A brief description of the different preparation strategies and some examples are provided in Table 1.

Table 1 – Description of some strategies used for the preparation of physically cross-linked hydrogels.

Strategy	Description	Ref.
Crystallisation	Crystals in the polymers' structure act as physical cross-linking sites leading to hydrogel formation. This can be accomplished by repetitive **freeze-thaw cycles** or by **stereo-complex interaction**.[85]	87–90
Ionic/ electrostatic interaction	Gelation of a polyelectrolyte solution by addition of di- or trivalent counterions with the opposite charge.[84]	91,92
Hydrogen bonding	Hydrogen bonding interactions can occur between the urea, amide, pyrrole, carboxylic acid, carbazole and hydroxylic groups themselves or between these groups and electron donor groups, such as imidazole and pyridine groups.[85]	93,94
Hydrophobic interactions	Hydrogels can be formed by hydrophobic interactions when a water-soluble polymer contains hydrophobic side chains, monomers or end groups. There are two main strategies to accomplish this: **thermal induction** and **ultrasonic treatment**.[85]	95,96

1.2.1.2. Chemical Cross-linking

Chemically cross-linked hydrogels are usually formed by covalent bonds between polymer chains and can occur by the bonding of functional groups present in the polymer backbone or between the polymer backbone and a cross-linker.[97] Comparatively to the physically cross-linked hydrogels, the chemical cross-linked hydrogels are more stable, cannot be dissolved in any solvent unless the covalent bonds in cross-linking points are cleaved, and exhibit a higher mechanical strength.[83,84] Moreover, chemical cross-linking allow a more precise spatiotemporal tuning of the gelation process.[66] The preparation of chemically cross-linked hydrogels can be achieved using several different methods such as chemical reaction of complementary groups, radical polymerisation, enzymatic reaction or high-energy radiation. These strategies are briefly described in Table 2.

Table 2 – Description of diverse methods used for the preparation of chemically cross-linked hydrogels.

Strategy	Description	Ref.
Chemical reaction of complementary groups	Polymers usually present functional groups such as OH, COOH, and NH_2, which can be used for the formation of covalent bonds between polymer chains with complementary functional groups. Examples of groups with complementary reactivity are amine-carboxylic acid, isocyanate-OH/NH_2 reaction, or Schiff base formation.[98]	[99,100]
Radical polymerisation	Radical polymerisation of monomers with low molecular weight in the presence of cross-linking agents.[98]	[101,102]
Enzymatic reaction	Formation of a strong covalent bond under physiological conditions and with a rapid gelation time that can be kinetically manipulated by regulating the enzyme concentration.[85]	[103,104]
High-energy radiation	Polymerisation of unsaturated compounds by gamma or electron beam radiation.[98]	[105]

1.2.2. Injectability

Injectability can be defined as the ability of a hydrogel to be delivered via direct injection using a syringe or catheter and has recently attracted considerable interest among the scientific community, namely in the biomedical field.[80] Injectable hydrogels are known to allow minimal invasive and straightforward procedures through injection, reducing the risk of infection, patient’s discomfort and pain, scars, treatment costs, and recovery time. Thus, they overcome some of the main drawbacks of the “traditional” implantable hydrogels, particularly in drug delivery and tissue engineering applications.[106] Furthermore, injectable hydrogels can easily adapt to the shape of its location, providing an excellent interface and fit of the hydrogel.[78]

Injectable hydrogels can be broadly classified as *in situ* forming hydrogels or self-healing and shear-thinning hydrogels. *In situ* forming hydrogels can undergo sol-gel transition at the target site by changes in the physical or chemical environmental conditions, such as temperature, pH, redox conditions, and ion concentration.[78] However, the gelation process usually requires severe conditions that sometimes cannot be achieved under physiological conditions, and that leads to the loss of bioactivity of loaded cells, drugs, and proteins.[107] Moreover, there is an inherent difficulty to control the gelation time *in vivo*. Slow gelation can culminate in the spreading of the hydrogel or hydrogel components and consequently in the diffusion and loss of the cargo molecules, while the fast gelation can originate a non-uniform hydrogel and the premature gelation in the syringe leading to needle blocking.[107] Additionally, as the *in situ* forming hydrogels are injected in the form of its liquid precursor solution (as unreacted radicals and polymers not cross-linked), and its gelation is not an instantaneous process, they may leak into neighbouring regions, limiting the hydrogel formation and possibly causing undesired toxicity.[78]

On the other hand, self-healing and shear-thinning hydrogels are pre-formed *ex vivo* and exhibit the ability to be delivered *in vivo* by extrusion through a syringe by application of shear stress.[78] Self-healing refers to the intrinsic ability of a hydrogel to damage repair without any external aid, which means that after shear application, the hydrogel exhibits a time-dependent recovery of the elastic modulus.[106] Shear-thinning is defined as the ability of a hydrogel to exhibit viscous flow under shear stress.[78] In this case, the hydrogel will flow when squeezed through the syringe (it becomes less viscous) and then, when the shear force is removed the viscosity increases again. The microscopic explanation for this behaviour is the destruction of the polymeric network under shear stress and the re-construction of the cross-linking bonds after the removal of stress, which can be ascribed as a self-healing process.[106]

Thus, self-healing and shear-thinning are closely related properties which impart the hydrogel the ability to flow when shear stress is applied through the syringe and to coalesce into an integral hydrogel at the target position.[78] As the hydrogel is already gelled when administrated, the local environment does not have a significant influence in the cross-linking. Furthermore, the self-healing of these hydrogels may be faster than the gelation of *in situ* forming hydrogels, overcoming the issues mentioned above.[106]

The self-healing ability of hydrogels is mainly imparted by the cross-linking through physical interactions and dynamic covalent bonds.[108] Examples of physical interactions are hydrophobic interactions,[109] electrostatic interactions,[110] hydrogen bonding,[111] π-π staking,[112] and metal-ligand coordination.[113] Typical dynamic covalent bonds are imine bonds (Schiff base),[114] disulphide bonds,[115] acylhydrazone bonds,[116] Diel-Alder "click chemistry",[117] dynamic reshuffling radical reactions,[118] and boronate-catechol complexation.[119]

However, both physical and dynamic covalent bonds exhibit weaknesses. Particularly, physical interactions exhibit more sensitivity to environmental conditions (*e.g.,* temperature, pH, and ionic strength) and are less stable when compared to covalent interactions. Nevertheless, physical interactions exhibit faster gelation times under mild conditions.[120] Notwithstanding, dynamic covalent bonds are stronger (more robust network) but exhibit a slower dynamic equilibrium.[121] Therefore, by the combination of both types of interaction, it is possible to obtain dual cross-linked hydrogels revealing rapid recovery (enhanced self-healing ability), high mechanical strength, long-term stability, and responsiveness to several factors[66,85,121] In the last years, several pioneering works have been made applying this strategy, proving its feasibility.[122–125] Thus, this thesis will address the development of a hydrogel constituted by dual cross-linking, namely by Schiff base and electrostatic interactions.

Reversible imine bond, also known as Schiff base, is formed by the dehydration reaction of an amine with an aldehyde or a carbonyl group and can occur under mild conditions, as depicted in Figure 11a.[106] Schiff base is considered a dynamic covalent bond due to the existing dynamic equilibrium between the functional groups involved. In the hydrogel network, there is a constant creation and destruction of the Schiff base bonds, imparting it with self-healing ability.[106] This type of linkage is suitable for its use in injectable hydrogels since the imine bond can be formed under physiological conditions, and the aldehyde group can strongly adhere to organs and tissues.[85] Schiff base linkage is highly vulnerable to acidic pH, undergoing hydrolytic cleavage when exposed to acidic environments.[126] Thus, this pH-sensitivity can be exploited in pH-responsive systems to trigger the release of therapeutic cargos. Moreover, hydrogels made of this kind of cross-linking exhibited a fast gelation time, good mechanical properties, and biocompatibility.[121]

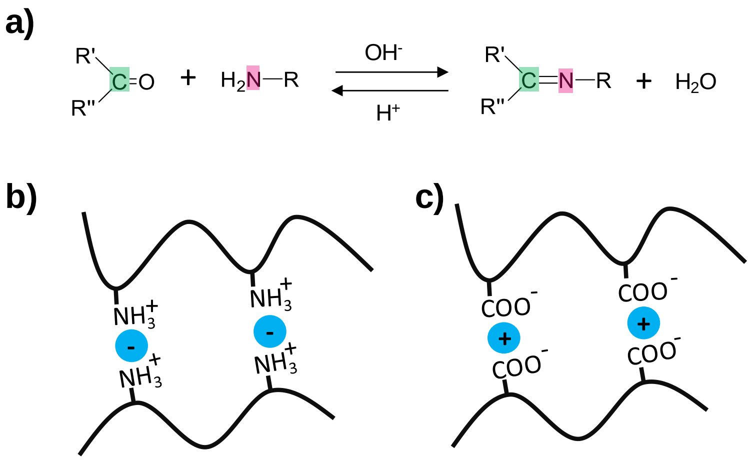

Figure 11 – Schematic representation of a) Schiff base formation and b) and c) electrostatic interactions between a positive or a negative charged polymer and anions or cations, respectively.

Ionic/electrostatic interactions originate hydrogels by the addition of counterions with the opposite charge to a polyelectrolyte solution (Figure 11b and c).[84] This type of cross-linking is known to originate hydrogels with self-healing ability since the physically cross-linked network can recover after being broken at high stress. However, hydrogels formed exclusively by ionic interactions show limited mechanical strength.[85] Since both players (polymer and cross-linker) must be ionised and have opposite charges for the electrostatic interaction to take place, one of the main factors influencing electrostatic interactions is the solution pH, which should be kept near the pKa interval of both participating molecules.[97] Considering that electrostatic interactions can be broken down by ionic species present in the environment, another important factor affecting this kind of bonds is the ionic strength of the solution.[127] The pH-sensitivity of this kind of cross-linking will be further discussed in Stimuli Sensitive release section.

Self-healing mechanisms are based on the fast equilibrium among the reversible dissociation and recombination of the groups involved in the cross-linking in a simultaneous and continuous way.[106] These mechanisms can be triggered by distinct driving forces such as thermally reversible reactions, molecular diffusion and entanglement, ionomeric arrangements, and reconstructive covalent dangling side chains or non-covalent hydrogen bonding.[128] The self-healing hydrogel systems have two important features:[106]

1. When damaged, the hydrogel produces some “mobile phases” in the injured area or nearby. These “mobile phases” fill and connect to the injured area, leading to its repair.
2. Under proper conditions, the hydrogel is cross-linked and healed by the interaction of the functional groups with each other.

Self-healing process can occur either spontaneously or triggered by some external stimuli, known as autonomic or non-autonomic self-healing, respectively.[81] In autonomic self-healing, hydrogels can repair themselves without any external stimulus, mainly due to the ability of the constituent materials to expose the functional groups involved in physical or chemical cross-linking without any stimulus. In contrast, non-autonomic self-healing may require a stimulus such as magnetic field, light, or heat to begin the healing process. Usually, in this sub-group, are inserted some hydrogels constituted by polymers that do not have functional groups able to form covalent bonds or to create non-covalent interactions spontaneously. Thus, external stimuli are required to provide extra energy to expose the groups involved in the cross-linking and then impart self-healing ability to the hydrogels.[106]

1.2.3. Stimuli-responsive Release

Conventional medicine consists of the systemic administration of high doses of specific drugs. This leads to the increase of the drug concentration in the blood when the medicine is taken, leading to a concentration peak that is usually followed by a fast decrease (in some extent due to the rapid clearance of the drug molecules from the body).[129] Moreover, this systemic administration of high drug doses leads to several side effects caused by non-specific uptake of the drugs from healthy cells in tissues and some organs like kidney, bone marrow, liver, and heart. To improve these issues, the concept of stimuli-responsive drug delivery has arisen. With this approach, the drug delivery system should be able to release its drug content in response to a given stimulus. The stimuli can be divided into internal or external stimuli, according to its origin.[130]

The internal stimulus consists of changes in the environment of the target site, which are characteristic of the pathology or from the target site. Some examples of internal stimulus are pH, enzymes, and redox conditions.

Regarding external stimulus, they are independent of the biological environment of the target site and depend only on the external stimulus. Light, temperature, magnetic field, electrical and mechanical stimulus are examples of commonly used external stimulus.[130] Thus, internal stimuli are related to the diseased environment, which is highly complex and variable, while external stimuli are more robust and controllable.[129] The next sections will introduce some frequently used stimuli, namely light, temperature, and pH.

1.2.3.1. Light-sensitive

Light-responsive systems attract significant interest due to the non-invasiveness and to the possibility of allowing the drug release in an accurate spatiotemporal way. Light-responsive systems can be sensitive to two types of radiation: UV and NIR light. A schematic representation of the electromagnetic spectrum and the main characteristics of both UV and NIR light being discussed in the next paragraphs is presented in Figure 12.

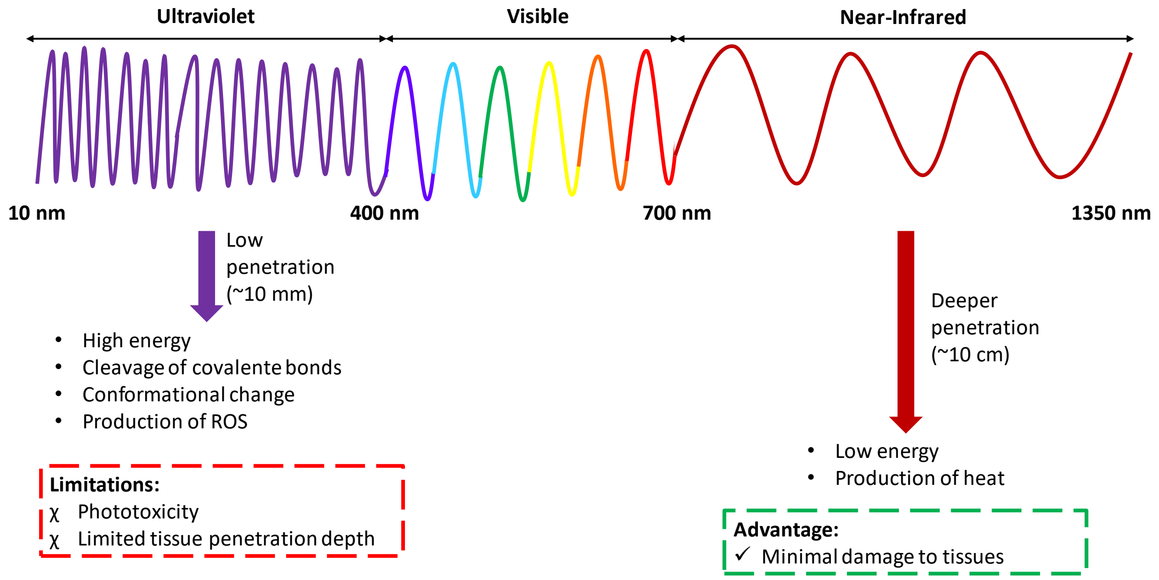

Figure 12 – Representation of the electromagnetic spectrum accompanied by main characteristics and effects of UV and NIR-light.

UV-responsive systems upon irradiation with UV light can undergo isomerisation or transformation of the materials leading to the release of their cargo. Moreover, UV light can also trigger the cleavage of covalent bonds and the production of reactive oxygen species (ROS).[131] However, UV-responsive systems have limited clinical potential due to possible phototoxicity and limited tissue penetration depth (around 10 mm) due to the strong absorption and scattering by water and other biological compounds (such as haemoglobin).[132] Comparatively to UV, NIR-light exhibits deeper tissue penetration (around 10 cm). Moreover, these wavelengths are known to cause minimal damage to healthy tissues, due to the decreased light absorption in living tissues by biomolecules and water. For this reason, NIR-responsive systems have gained significant attention.[132] This type of systems converts electromagnetic energy into heat and can be used to trigger the release of the cargo in drug delivery systems (such as nanoparticles or hydrogels), that can be either on their surface or encapsulated.[133] NIR-responsive systems are also commonly used for the thermal ablation of cancer cells, known as PPT.[130] A distinct approach that employs NIR radiation is photodynamic therapy (PDT), which consists in the delivery of photodynamic agents that generate reactive oxygen species upon NIR irradiation, leading to the eradication of cancer cells.[132] This subject will be further discussed in Photothermal Therapy section.

To obtain a NIR-responsive DDS, it is necessary to incorporate a material having one of the following features:[134]

- Large absorbance in the NIR region, culminating in the increase of the temperature, which finally triggers the release of the therapeutic cargo;
- Two-photon absorption (TPA), *i.e.*, photo-cleavable groups which can undergo cleavage with the absorption of two photons instead of one UV photon;
- Up-converting NPs, which converts NIR photons into high energy photons in visible and UV range. The high-energy photons produced can then be used to activate photo-sensitive materials for drug release or to generate ROS.

Some materials that have been widely used in the development of NIR-responsive delivery systems are gold nanomaterials (*e.g.,* nanorods, nanoshells, nanostars, NPs), carbon nanomaterials (*e.g.,* carbon nanotubes and graphene), polymeric nanomaterials, and upconversion nanomaterials (*e.g.,* $NaYF_4$ or CaF_2).[132] The polymeric nanomaterials are a particular type of materials since they do not produce the photothermal effect by themselves, and thus have to be combined with photochromic molecules.[132] The molybdenum blue $\{Mo_{154}\}$ contains 28 (partially) delocalized electrons causing the blue colour and the related absorption band in the NIR region.[20,21] Owing to its strong absorption in the NIR region, the reduced molybdate $\{Mo_{154}\}$ is an excellent candidate for the development of polyoxometalate based PPT systems. There is one report in the literature regarding the use of $\{Mo_{154}\}$ in the development of PTT systems,[64] showing its viability in our demand for a novel therapeutic system which combines the PTT and NIR-triggered drug release synergistically.

1.2.3.2. Temperature

Some treatments (such as PTT) lead to the heating/ temperature increase of the target region (to around 40-44 ºC). Thus, the drug delivery system can be designed to respond to the increase of the temperature, releasing its cargo in the desired site.[130]

Thermo-responsive polymers may belong to one of two main classes: polymers with a lower critical solution temperature (LCST) and polymers with an upper critical solution temperature (UCST). The lower and upper critical solution temperatures are defined as the temperatures at which below and above the polymer and the solvent are entirely miscible, respectively.[135] In other words, the critical solution temperature, can be defined as the temperature at which the polymer solution suffer phase transition from one to two phases.[136] Up to now, polymers exhibiting LCST are most widely used in biomedical applications and therefore the most exploited ones.[136] For this reason, in this document, we will focus only on the mechanism of thermo-responsiveness of polymers with LCST.

There are three main types of interactions in a polymer solution: polymer-water, polymer-polymer, and water-water interactions. Below the LCST, the enthalpy term of Gibbs equation ($\Delta G=\Delta H-T\Delta S$ where ΔG is free energy, ΔH enthalpy, T temperature, and ΔS entropy) related with hydrogen bonding responsible for polymer-water interactions, is dominant and then responsible for the polymer swelling and dissolution. The temperature increase above the LCST leads to an increase in entropy due to the water-water associations.[136] Given the Gibbs equation, this increase in the entropy will culminate in an increase in negative free energy of the system, making polymer-water interactions unfavourable, thus facilitating polymer-polymer and water-water interactions, culminating in the collapse of the polymer (the so-called hydrophobic effect).[136,137] Then, below the LCST, the polymer solution is clear and homogeneous, indicating that the polymer is completely soluble. On the other hand, increasing the temperature above LCST the polymer becomes more hydrophobic and then, insoluble culminating in the transition to a cloudy solution or even in gel formation.[135]

Examples of LCST polymers are poly(N-vinylcaprolactam) (LCST ≈ 26-35ºC), poly[2-(dimethylamino)ethyl methacrylate] (LCST ≈ 50ºC), poly(ethylene glycol) (LCST ≈ 85ºC), and poly(N-isopropylacrylamide) (PNIPAAm, LCST ≈ 32ºC).[135,136] Among these, due to its phase transition temperature similar to the body temperature (37ºC), PNIPAAm is the thermo-responsive polymer most widely investigated for biomedical applications.[135]

PNIPAAm is a polymer constituted by NIPAAm monomers. The chemical structure of the NIPAAm monomer is represented in Figure 13a, which highlights the hydrophilic (-NHCO-) and hydrophobic ($-CH(CH_3)_2$) groups,[81] in blue and orange, respectively. In aqueous solution, below the LCST, PNIPAAm is soluble due to the hydrogen bonding of the amide groups with water molecules[138] and exhibits a flexible, extended coil conformation.[137] When the temperature increases, the molecular agitation also increases, and the molecules are not able to remain in a stable position, leading to the weakening of the hydrogen bonds between the hydrophilic groups and the water molecules. This phenomenon is accompanied by the concomitant strengthening of the hydrophobic interactions between the hydrophobic segments of the polymer (the hydrophobic effect).[139] Then, when the temperature increases to around 32ºC (LCST), PNIPAAm shows a volume phase transition, *i.e.* the polymer shrinks and expels the solvent, in this case, the water, adopting a globular conformation.[138]

PNIPAAm hydrogels exhibit the same behaviour as free polymer, and thus, due to the association of the polymer chains through hydrophobic interactions, the hydrogel collapses from the coil to a globular structure, resulting in the hydrogel shrinkage.[81,137,140] This process is schematized in Figure 13b.

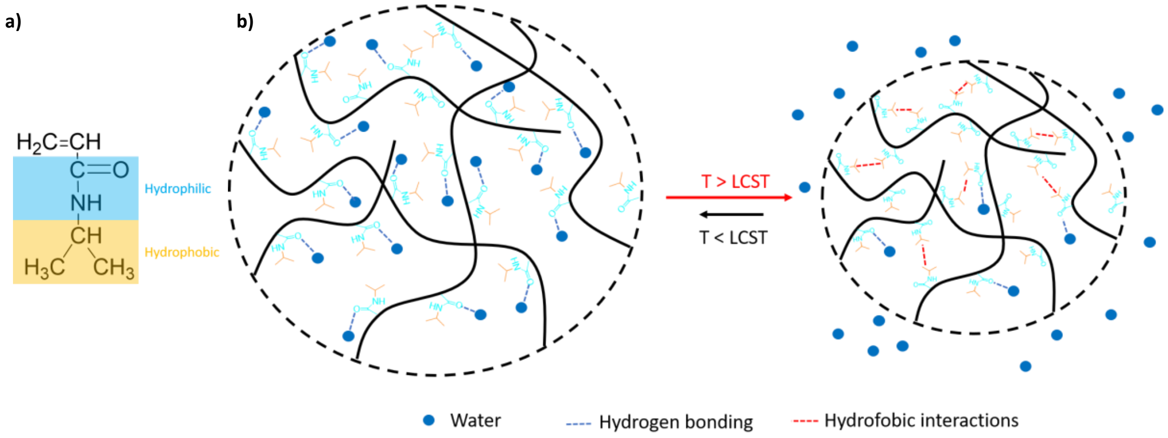

Figure 13 – a) Chemical structure of NIPAAm monomer, highlighting the hydrophilic (blue) and hydrophobic (orange) groups. b) Schematic illustration of the volume phase transition of a PNIPAAm hydrogel during heating or cooling.

The LCST can be tailored through the copolymerization with hydrophobic (stronger hydrophobic forces, leading to the collapse at a lower temperature) or hydrophilic (strengthening the polymer-water interactions, leading to an increase in the LCST) moieties.[137,140] In this case, several PNIPAAm copolymers with poly (N,N-diethylacrylamide) (LCST ≈ 25-32ºC), poly(dimethylaminoethyl methacrylate) (LCST ≈ 50ºC), poly(N-CL)-1-hydroxymethyl) propyl methacrylamide (LCST ≈ 30ºC) for example, were developed.[136]

1.2.3.3. pH

The pH of normal tissues is around 7.4, whereas tumour and inflamed tissues present pH values slightly acidic (ranging from 6.5 to 7.2, and 5.4 to 7.2, respectively).[130,141–143] Therefore, hydrogel based-DDS can take advantage of this characteristic by releasing the active agent in response to the pH decrease.

pH-responsiveness can be imparted to hydrogels by two main mechanisms:[144]

1. The presence of ionizable groups in the polymer's structure;
2. The use of cross-linkers able to form acid-sensitive linkages between the polymer chains.

In the first case, the polymer is usually a polyelectrolyte (a polymer that contains a large number of ionizable groups).[145] The ionizable groups can be either acidic or basic and can accept or donate protons as a function of the changes in the environmental pH as schematized in Figure 14a i and ii, respectively. The pH at which a specific group suffer ionisation is known as pK_a. By changing the pH across this threshold, a fast change in the polymer's net charge will occur leading to the generation of repulsive electrostatic forces, culminating in an increase in the hydrodynamic volume of the polymer chains and consequently in the swelling of the hydrogel.[127,145] In other terms, a highly charged structure causes electrostatic repulsion, leading to the hydrogel swelling. Moreover, the ionisation causes dissociation of hydrogen bonds between the polymer chains, resulting in discontinuous volume changes.[81] Thus, any factor able to reduce the repulsion such as pH, ionic strength, and counter ions, can affect the extent of swelling.[81,127]

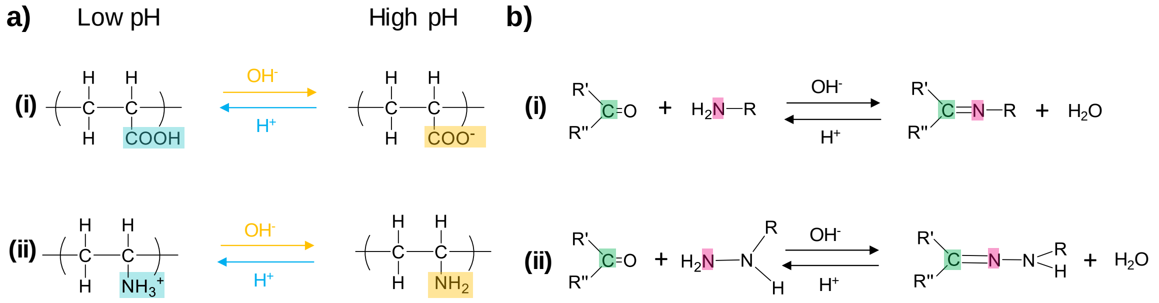

Figure 14 – Schematic illustration of the two main mechanisms responsible for hydrogel's pH-responsiveness. a) pH dependence of (i) anionic and (ii) cationic polyelectrolytes. b) Acid-sensitive bonds: (i) Schiff base and (ii) hydrazone.

Furthermore, to keep the charge neutrality, an ion concentration gradient between inside and outside the hydrogel is generated. Then, the repulsive electrostatic forces are counterbalanced by anions or cations that move into the hydrogel from the outer solution. The increase of the concentration of mobile ions (cations or anions) in the hydrogel, originates an osmotic pressure that makes the hydrogel to swell. Finally, the hydrogel swelling, which induces elastic restoring forces, balances the osmotic pressure, culminating in the equilibrium in the hydrogel.[81,146]

The second approach described consists in the cross-linking of the polymer chains through acid-sensitive bonds formed between the cross-linker and the polymer chains. Thus, the acidic pH triggers the cleavage of these bonds leading to the release of loaded drug molecules, exposure of targeting ligands, and modification of the polymer charge.[144] Examples of these acid-labile bonds are the Schiff base[147] and hydrazone,[148] represented in Figure 14b i and ii, respectively. Usually, the cleavage of bonds causes complete disassociation of hydrogels, and complete payload release compared with swelling-controlled release mechanism.

1.2.4. Chitosan

Chitosan (CS) is a natural linear polymer constituted by glucosamine and N-acetylglucosamine units linked by β(1-4) glycosidic bonds, as depicted in Figure 15. CS is obtained by the deacetylation of chitin, the second most abundant natural polymer on earth, and can be found in the exoskeleton of crustaceans like as crabs, lobsters, and shrimps.[149] Usually, the chitin deacetylation occurs under alkaline conditions (using concentrated NaOH) or by enzymatic hydrolysis (with chitin deacetylase). To be considered as chitosan, chitin needs to exhibit a deacetylation degree above 50% (depending on the source), becoming soluble in slightly acidic aqueous solutions.[150,151]

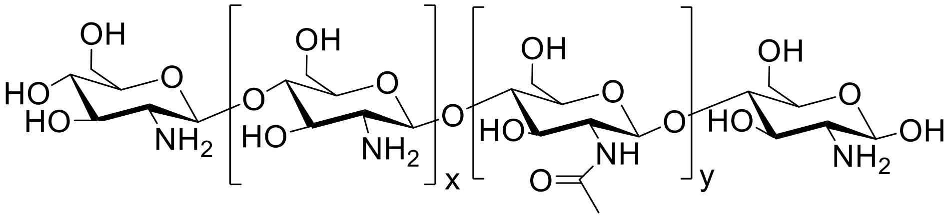

Figure 15 – Chemical structure of chitosan, where x denotes the number of glucosamine units and y the number of N-acetylglucosamine units in the polymer chain.

Due to the presence of numerous NH_2 groups and to its existence in several molecular weights, CS is chemically versatile. Moreover, CS is known to be biocompatible, biodegradable, and non-toxic.[152,153]. For these reasons, CS is a fascinating material widely used in biomedicine.[149,154,155] This biopolymer can form hydrogels by itself through merely adjusting the pH, by dissolving in a nonsolvent, or by simple mixture with other polymers via electrostatic interactions. However, these hydrogels exhibit weak mechanical properties and uncontrolled dissolution.[156] For this reason, it has emerged the need for new chitosan-based hydrogel formulations built up by chemical cross-linking. Among them, injectable and self-healing hydrogels are also attracting considerable interest, namely the ones formed by Schiff base (or imine bonds) cross-linking, taking advantage of the numerous amine groups in the CS backbone.[107]

1.2.5. Photothermal Therapy

As previously referred in this document, the actual cancer therapies are known to cause several side effects and poor treatment outcomes, motivating the development of more effective and precise treatment strategies.[157] Among the emerging cancer therapies are gene therapy, immunotherapy, PDT, and PTT. PTT is a highly effective, selective, and minimally invasive treatment able to eliminate several types of cancers.[158,159] In this treatment technique is used an external laser which allows the tuning of the dosage and the precise targeting of the tumour place, minimising the damage to the neighbouring healthy tissues.[158]

PTT uses photothermal agents to transduce the absorbed light (photon energy) into heat (thermal energy) and induce hyperthermia.[57] Hyperthermia is defined as the administration of heat to treat a disease. It is known to be effective in local cancer ablation owing to the chaotic architecture of the vasculature in solid tumours. The abnormal vasculature in the tumour region culminates in low pH and hypoxia, making the cancer cells more sensitive to hyperthermia, regarding the normal cells.[160] Thus, it is reported that the cancer cells can be ablated at temperatures between 40 and 44 ºC due to the DNA damage, disruption of the cellular membrane, and protein denaturation.[161] Furthermore, the high temperatures induced by PTT can also stimulate the immune system due to the expression of heat shock proteins and to the increase in migration of lymphocytes to the tissues with febrile temperatures.[162]

Photothermal therapy has been widely studied over the last years, as an emergent and promising treatment method. The reports found in the literature primarily focus on the development of new photothermal agents and its composites aiming to reduce their toxicity and ultimately to improve their photothermal conversion efficiency. Despite all the efforts to seek more efficient systems, most of the developed materials need high irradiance values (mostly above or equal to 1 W/cm^2). This thesis tries to fill this research gap by exploring the use of the polyoxometalate {Mo_{154}} as a potential photothermal agent. Furthermore, in the course of this thesis, it is developed an injectable hydrogel for dual combination therapy (drug and photothermal).

2. Aims

The giant polyoxomolybdate $\{Mo_{154}\}$ will be used in the development of composites for dual combination therapy, *i.e.*, drug and PTT. In particular, the aims of this thesis are as follows:

- To prepare and characterise an injectable and self-healing hydrogel composed by chitosan grafted with PNIPAAm (CS-g-PNIPAAm), di-functionalised PEG (DF-PEG), and $\{Mo_{154}\}$;
- To study the thermo- and pH-triggered release of a model drug (doxorubicin) and a protein (horseradish peroxidase);
- To access the *in vitro* cytotoxicity of the hydrogel and its initial components;
- To evaluate the *in vitro* photothermal performance of the prepared hydrogels.

3. Results and Discussion

This chapter presents and discusses all the obtained data from the characterisation of the starting materials and the developed hydrogel to the *in vitro* release and cytotoxicity studies. Additionally, the results obtained in the photothermal conversion studies are analysed and discussed.

3.1. Preparation and Characterisation of Starting Materials

In this section, the preparation and characterisation of the raw materials used to prepare the hydrogels, namely {Mo_{154}}, chitosan grafted with PNIPAAm (CS-g-PNIPAAm), and di-functionalised poly(ethylene glycol) (DF-PEG) are discussed.

3.1.1. {Mo_{154}}

{Mo_{154}} was prepared by acidification of an aqueous molybdate solution, followed by its reduction using sodium dithionite, as described by Müller and his team.[15] To confirm its successful preparation, several characterisation techniques, such as ultraviolet-visible (UV-Vis), Fourier-transform infrared spectroscopy (FTIR), and Raman spectroscopy were performed.

The UV-Vis spectrum of the big-wheel, depicted in Figure 16a, shows two bands centred at 745 and 1070 nm, known to be characteristic of the molybdenum blue species.[163] These bands are assigned to the intervalence charge transfer transitions (Mo^{V}/Mo^{VI}). Moreover, the visible UV-Vis band (centred at 745 nm) is also responsible for the characteristic dark-blue colouration of the {Mo_{154}} crystals and solution, as it is possible to confirm in Figure 16b and 16c.[21]

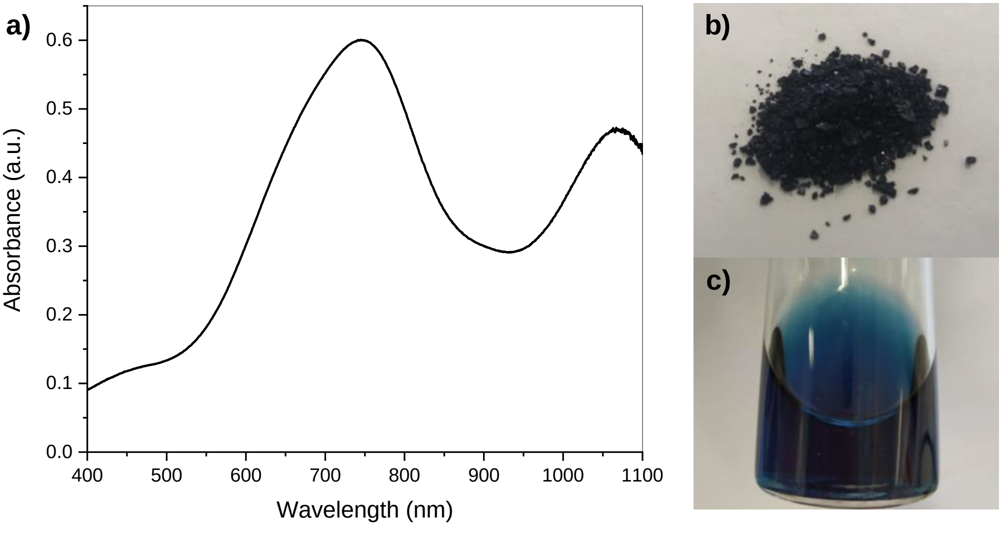

Figure 16 – a) UV-Vis spectrum of {Mo_{154}} in aqueous solution with a 0.1 mg/mL concentration. b) and c) photographs exhibiting the dark-blue coloration of {Mo_{154}} in crystal and in 1 mg/mL aqueous solution, respectively.

In Figure 17, it is possible to observe the FTIR spectrum of {Mo_{154}}. Analysing this spectrum, it is possible to find the {Mo_{154}} characteristic bands, namely the band centred at 1616 cm^{-1} assigned to $\delta(H_2O)$, and the bands at 970 and 912 cm^{-1} that are attributed to ν(Mo=O). Moreover, the bands at 750, 630, and 555 cm^{-1} are also reported to be characteristic from {Mo_{154}}.[163]

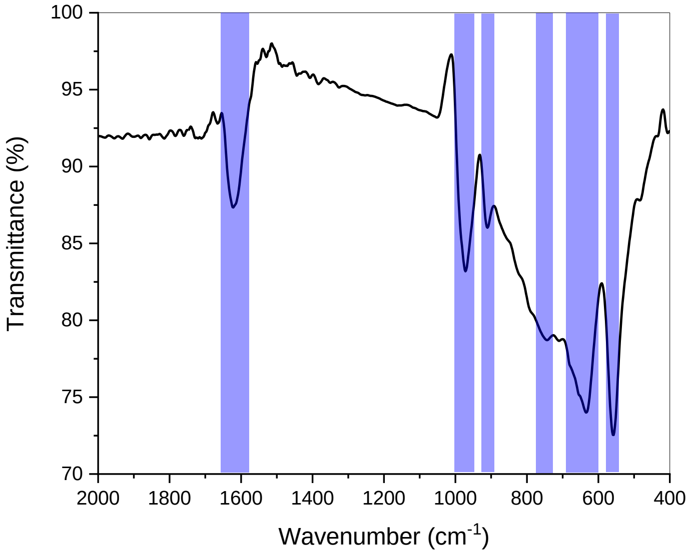

Figure 17 – FTIR spectrum of {Mo_{154}}. The characteristic FTIR peaks of {Mo_{154}} are highlighted in blue.

To further prove the successful preparation of the mentioned polyoxometalate, Raman spectroscopy was also performed. The solid-state Raman spectrum is displayed in Figure 18, and it is possible to identify five main bands centred at 793, 534, 463, 323 and 211 cm^{-1}. These bands agree with the patterns described in the literature.[163] The band centred at 323 cm^{-1} is ascribed to the δ(Mo−O−Mo), and the band at 793 to the {$(Mo^{V/VI})_3\mu_3$-O}.

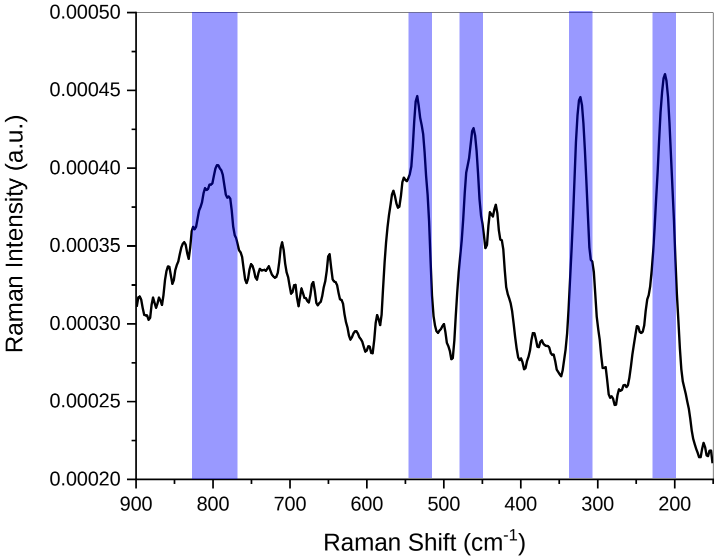

Figure 18 – Solid-state Raman spectrum of {Mo_{154}} (λ_e = 1064 nm). *The characteristic Raman bands of {Mo_{154}} are highlighted in blue.*

Thus, since the analysis carried out are in agreement with the data reported in the literature, it is possible to conclude that the {Mo_{154}} was successfully prepared.

3.1.2. Chitosan Grafted with Poly(N-isopropylacrylamide)

Chitosan (CS) is known to be a biodegradable, biocompatible, and non-toxic biopolymer widely used in biomedicine for drug delivery and tissue engineering purposes.[149,154,155] CS shows pH-responsive properties owing to the presence of amino groups, in its structure, that can be protonated and deprotonated as a function of the environmental pH.[164] However, it does not show thermo-responsive properties. Thus, a typical procedure to impart CS the ability to respond to temperature variations is *via* modification with a thermo-responsive polymer, such as poly(N-isopropylacrylamide) (PNIPAAm) or poly(N-vinylcaprolactam).[155] Due to its lower critical solution temperature (LCST ≈ 32 ºC) near to the body temperature and its abrupt phase transition, PNIPAAm is the most widely used thermo-responsible polymer in biomedical applications.[135]

Therefore, the approach here followed was the grafting of CS with PNIPAAm through a free-radical polymerisation previously described by Duan *et al*.[165]. The process initially involves the formation of radicals in the CS molecules using ammonium persulfate as initiator, followed by the addition of NIPAAm monomers, as schematized in Figure 19. To verify the success of the grafting reaction, ^{1}H NMR (nuclear magnetic resonance) and FTIR were performed. Dynamic light scattering (DLS) and differential scanning calorimetry (DSC) were done to demonstrate the thermo-responsiveness of the final polymer.

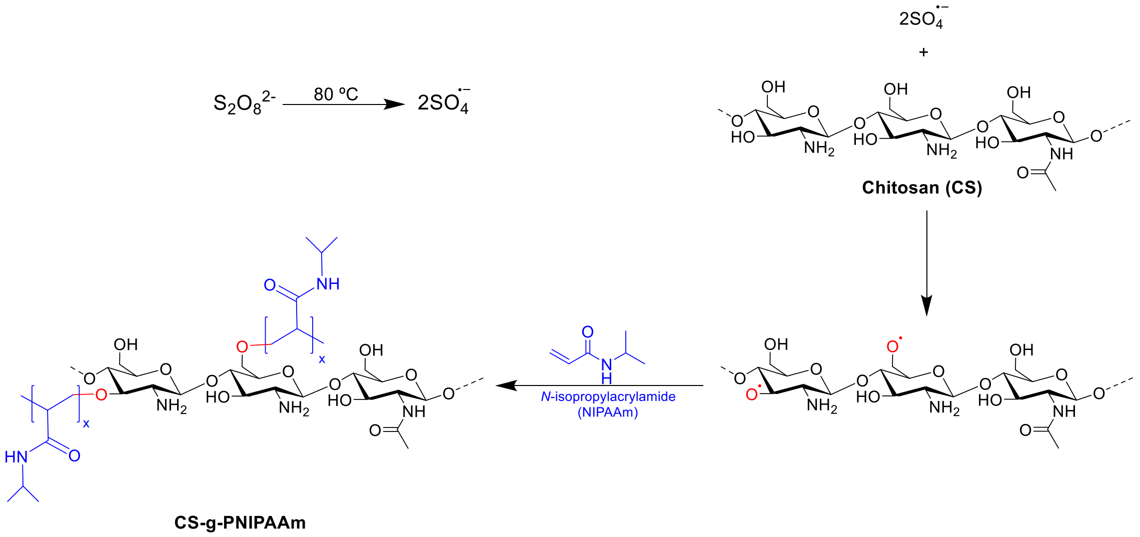

Figure 19 – Reaction scheme of the grafting reaction of NIPAAm in CS. "x" represents the number of NIPAAm monomers.

The ^1H NMR spectrum of CS-g-PNIPAAm (Figure 20) shows the typical CS peaks, namely the peaks in the region from 3.56 to 4.10 ppm, corresponding to the overlap of the signals from H3 to H6 and the peak at 3.14 ppm ascribed to the H2 in the glucosamine unit of CS. Moreover, the peak at 2.03 ppm can be assigned to the H7. This data is in agreement with the described in the literature.[166–168] Beyond the typical CS peaks, the ^1H NMR spectrum also displays four new peaks characteristic of PNIPAAm. The peak at 3.90 ppm is assigned to the Hb (-NH-CH<), and the peaks at 1.53 and 1.96 ppm are ascribed to the Hc and Hd (-CH-CH$_2$-), respectively. Furthermore, it is also possible to find a sharp peak at 1.10 ppm that is assigned to the Ha of the two methyl groups of PNIPAAm.[168,169] Thus, since the ^1H NMR spectrum displays the characteristic peaks of both CS and PNIPAAm, it is possible to conclude that the grafting reaction occurred, as expected. Moreover, ^1H NMR analysis can provide information about the relative percentage of each component in the final polymer. Thus, integrating the area of the peaks at 1.10 and 3.14 ppm and normalising the value by the number of protons ascribed to each signal, it is possible to know the ratio between the number of glucosamine units from CS and NIPAAm monomers from PNIPAAm. In this way, it was found that there are 3.9 NIPAAm monomers per chitosan unit. Thus, it was estimated that the CS-g-PNIPAAm molecular weight is 605.5 g/mol and that the weight percentage of PNIPAAm and CS in the final polymer is around 73% and 27%, respectively.

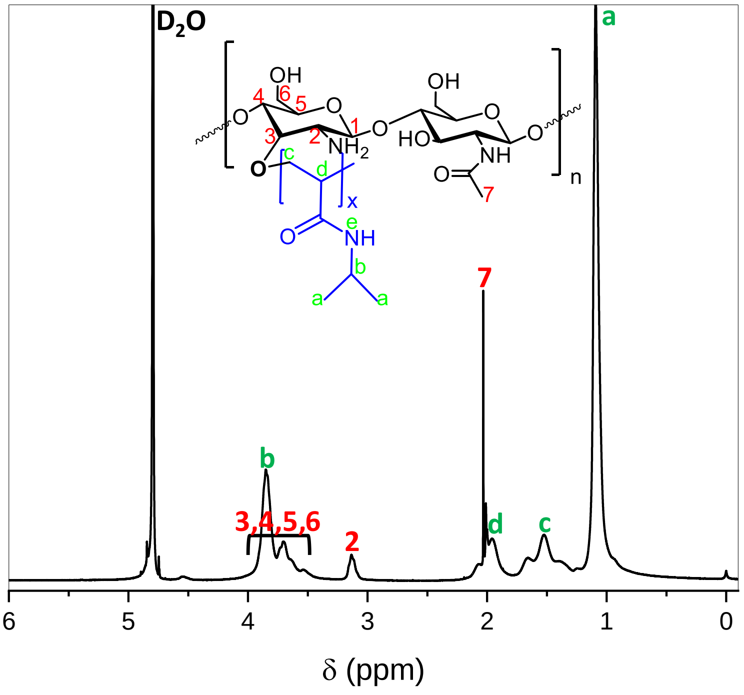

Figure 20 – ^1H NMR spectrum of CS-g-PNIPAAm in 1% of deuterium chloride. In the inset is presented the structural formula of CS-g-PNIPAAm copolymer.

To further confirm the success of the grafting reaction, FTIR spectroscopy of the obtained copolymer, as well as the initial materials was performed (Figure 21). The CS spectrum shows a broad band between 3368 and 3287 cm^{-1}, corresponding to N-H and O-H stretching modes and intramolecular hydrogen bonds, respectively. The bands centred at 2920 and 2871 cm^{-1} are assigned to C-H symmetric and asymmetric stretching, respectively. Two bands at 1652 and 1315 cm^{-1} can be ascribed to C=O stretching of amide I and C-N stretching of amide III, respectively, proving the presence of residual N-acetyl groups. A band around 1577 cm^{-1} can be assigned to the N-H bending of the primary amine. The bands at 1421 and 1374 cm^{-1} correspond to CH_2 bending, and CH_3 symmetrical deformations and the band centred at 1151 cm^{-1} can be ascribed to the asymmetric stretching of the C-O-C bridge. Finally, the two bands at 1061 and 1026 cm^{-1} are assigned to C-O stretching (C_3-OH and C_6-OH). All of the described bands are in agreement with the reported in the literature for CS.[170,171]

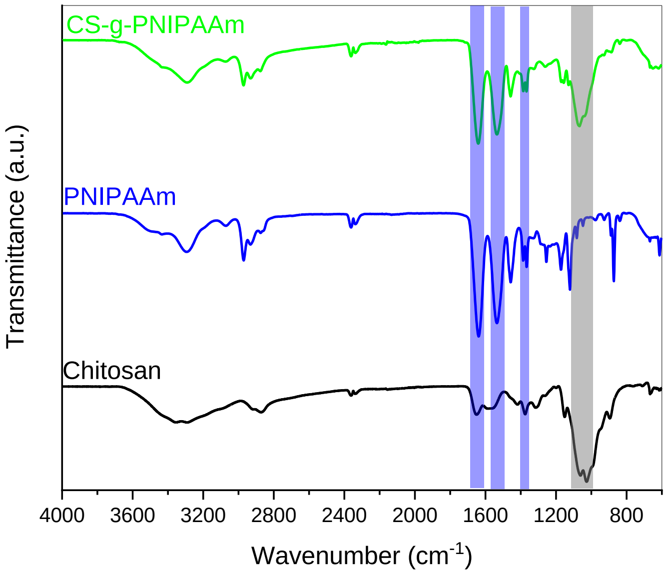

Figure 21 – FTIR spectra of chitosan, PNIPAAm, and CS-g-PNIPAAm. The blue and grey bands highlight the shared peaks among CS-g-PNIPAAm and PNIPAAm or CS, respectively.

In PNIPAAm spectrum, it is possible to observe some broad bands between 3600 and 3200 cm^{-1}, which can be assigned to the N-H stretching, and a band around 3072 cm^{-1} corresponding to the stretching frequency of the amide. The bands in the region between 2996 and 2844 cm^{-1} can be attributed to the C-H stretching of the -CH_2- bridges in PNIPAAm network. The bands centred at 1639 and 1533 cm^{-1} correspond to the amide I and II, respectively. In addition, two bands centred at 1387 and 1368 cm^{-1} can be ascribed to the presence of bending of isopropyl groups from NIPAAm. This data fits the described in the literature for the same polymer.[172,173]

The CS-g-PNIPAAm FTIR spectrum shows several new bands comparatively to the original CS spectrum, namely the bands centred at 1639, 1533, 1387, and 1368 cm^{-1}, confirming the presence of PNIPAAm in the grafted biopolymer.[174] Furthermore, the two bands at 1065 and 1027 cm^{-1} characteristic of the C_3-OH and C_6-OH of CS, exhibit a decrease in intensity, indicating that these two groups may be chemically bonded to PNIPAAm.[165] Therefore, from the ^{1}H NMR and FTIR spectroscopy data, it is possible to conclude the success of the grafting reaction, indicating that the final product is CS-g-PNIPAAm.

To assess the thermo-responsiveness of the prepared copolymer and investigate the phase transition temperature, DLS and DSC measurements were performed.

As previously mentioned, thermo-responsive polymers are characterised by a phase transition from the extended coil to globule at a given temperature, known as the critical solution temperature. Thus, for polymers presenting LCST, below this temperature, the polymer molecules exist as individual dissolved polymer chains (known as coil conformation), exhibiting a small hydrodynamic diameter. However, increasing the temperature above the LCST, the dehydration process (*i.e.,* the breakdown of hydrogen bonds between the polymer chains and the water molecules) leads to the collapse and agglomeration of the free polymer chains by hydrophobic interactions, known as globule conformation. The polymer in the globule conformation shows a larger size than the free polymer molecules in the coil conformation.[175] Thus, the phase transition is characterised by a drastic increase in particle size, which can be monitored by DLS.

DLS is based on the measurement of the time-dependent variations in the scattered light caused by the Brownian motion of the particles. Thus, the velocity of the Brownian motion can be measured and is usually known as the translational diffusion coefficient (D).[176] D can be related to the particle's size by the Stokes-Einstein equation:

$$D_h = \frac{kT}{3\pi\eta D}$$

where, D_h represents the mean hydrodynamic diameter, k the Boltzmann's constant, T the absolute temperature, η the viscosity of the dispersing medium, and D the translational diffusion coefficient. Thus, DLS measurements can be performed at several temperatures in order to relate the particle's size with the temperature, as shown in Figure 22. It was possible to verify an abrupt change in the hydrodynamic diameter from 25 to around 300 nm, for temperatures above 27 to 30 ºC. This indicates that the polymer in solution suffered a phase transition from the coil to the globule conformation, confirming the thermo-responsiveness of the prepared copolymer.

The critical temperature value obtained from the mentioned graph corresponds to the phase transition temperature. It is noteworthy to clarify that the phase transition temperature is different from LCST. The LCST is defined as the temperature below which all the polymer concentrations are soluble, while phase transition temperature corresponds to the temperature at which a polymer solution with a specific concentration undergoes a phase transition from coil-to-globule.[175] Thus, from Figure 22 is possible to verify that for a CS-g-PNIPAAm aqueous solution with 0.005 wt-%, the phase transition temperature is around 27 to 30 ºC. This value slightly deviates from the values reported in the literature for chitosan grafted PNIPAAm co-polymers, around 32-33 ºC.[177–179] However, there is one report describing the preparation of CS-g-PNIPAAm, using a distinct synthesis method, with a phase transition temperature around 30 ºC.[180] Several factors are known to influence the phase transition temperature of a polymer, such as a polymer concentration,[175] pH, the concentration of salts, and the presence of surfactants.[177] Thus, since there are not surfactants in the system analysed, the shift observed can be explained by variations in one of the other parameters mentioned. It is also interesting to note the large error bars of the diameters obtained at 28 and 29 ºC. Since these points are so close to the phase transition temperature, there may exist the formation of some unstable bigger aggregates that quickly disappear, originating discrepant measurements and big error bars.

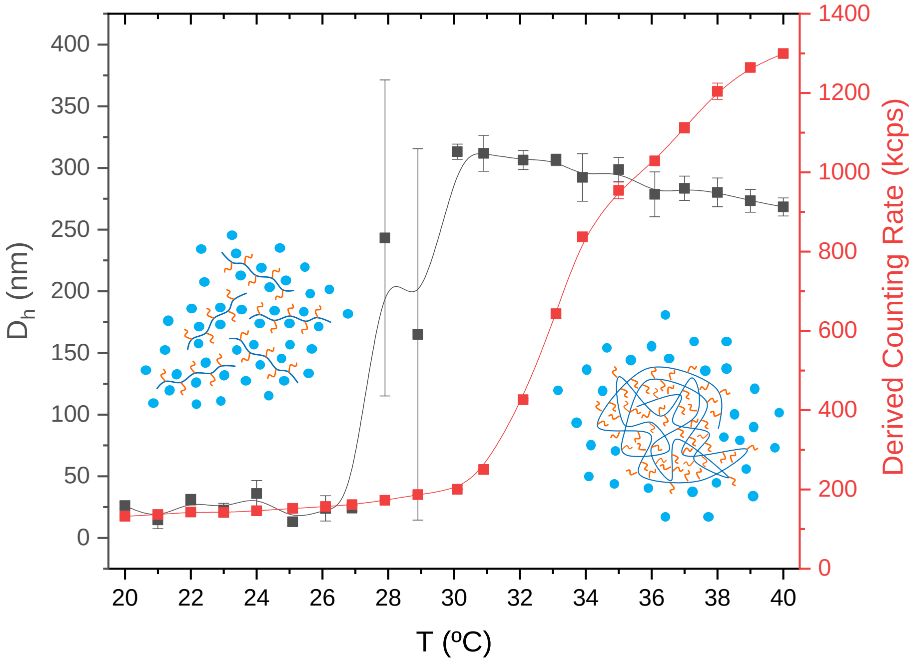

Figure 22 – Evolution of D_h and derived counting rate of an aqueous solution of CS-g-PNIPAAm (0.005 wt-%) with the increase of the temperature measured by DLS. The full line represents a B-Spline fitting, and the error bars represent the standard deviation of each point. The graph is accompanied by a schematic representation of the extended coil and globular conformation characteristics from below and above phase transition temperature, respectively. In blue is represented the polymer backbone, in orange, the hydrophobic domains of the polymer and the light-blue spheres represent the water molecules.

Another parameter that can be analysed by DLS is the variation of the scattered light, which can be evaluated by the derived counting rate. According to the Rayleigh dispersion theory, the intensity of the scattered light is proportional to d^6, where *d* corresponds to the particle diameter.[175] Thus, in the coil to globule transition, it is possible to verify a sharp increase in the scattered light. Moreover, the partial dehydration of the polymer generates an increase in the difference between the refractive index of the concentrated and the dilute phase, therefore increasing the amount of scattered light. In contrast, the difference in the refractive index between the hydrated polymer and the water is not so significative, causing less scattering below the phase transition temperature.[175] This sharp increase in the scattered light is also visible in Figure 22 at around 30 ºC, being in accordance with the previously discussed.

The phase transition of a thermo-responsive polymer exhibiting LCST is known to be an endothermic process, and thus can be characterised by DSC.[175] DSC is based on the measurement of the difference of heat capacity between two materials: a reference and a sample. For this, the reference and the sample pan are heated, and the temperature change for a given amount of heat is measured in each pan. Thus, using this technique is possible to obtain a graph like the one depicted in Figure 23, exhibiting the dependence of the heat flow with the temperature of a CS and CS-g-PNIPAAm solutions. CS itself did not exhibit any peak, indicating that this polymer does not show thermo-responsive behaviour in the temperature range analysed. This result agrees with the reported in the literature since CS is known to be a polymer that presents no thermo-responsiveness.[155]

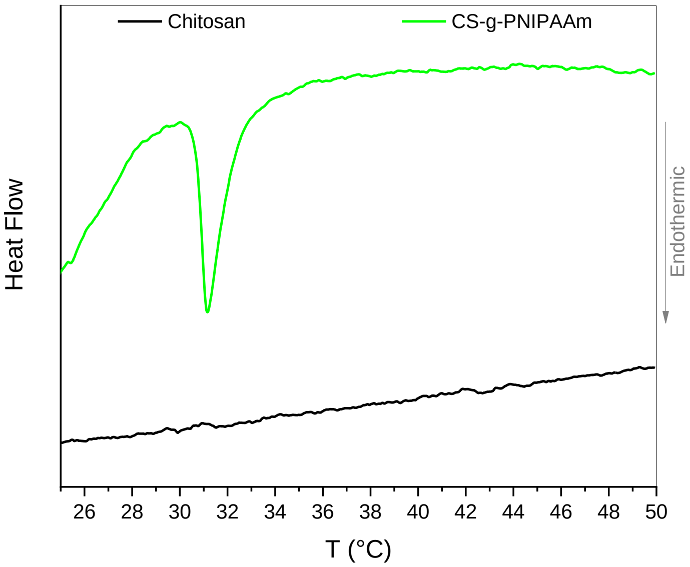

Figure 23 – Heat flow versus temperature of CS (2.0 wt-%) and CS-g-PNIPAAm solutions (1.5 wt-%) measured by DSC.

In contrast, CS-g-PNIPAAm showed an endothermic peak around 31 ºC associated with the phase transition, thus proving the thermo-responsiveness of the prepared copolymer. The value obtained by DSC for the phase transition temperature is in agreement with the data obtained by DLS.

Figure 24 shows three pictures of the same CS-g-PNIPAAm aqueous solution before, right after heating to 37.5 ºC, and after cooling down. Before heating, the solution was transparent, indicating that the polymer chains are hydrated and in a coil conformation. After heating above the phase transition temperature, the polymer molecules are in a globule conformation, giving an opacity to the solution. After cooling down, the polymer solution suffers a new phase transition back to the coil conformation, becoming transparent again. This proves the reversibility of the phase transition process, which was previously described for polymers exhibiting LCST.[177,181]

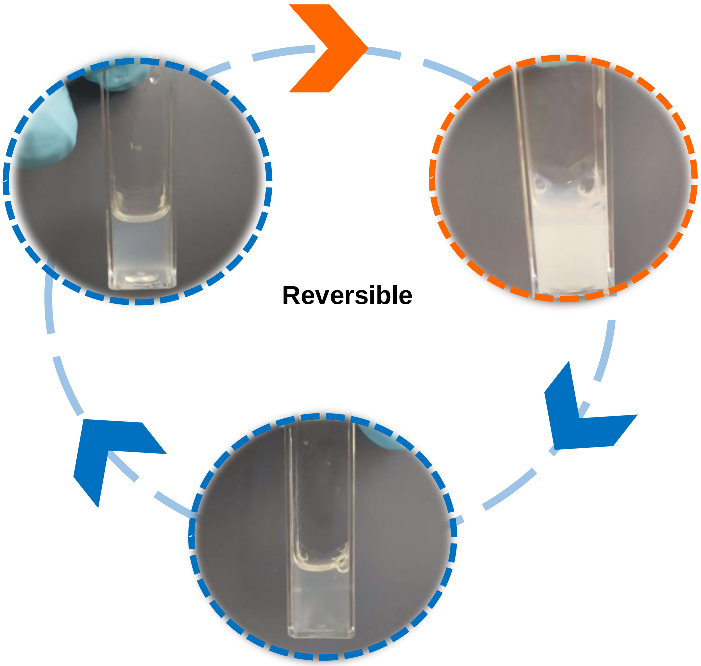

Figure 24 – Scheme demonstrating the reversible thermo-responsive behaviour of CS-g-PNIPAAm. The pictures in the blue and orange circles correspond to the polymer solution at room temperature and 37.5 ºC, respectively. Similarly, the blue and orange arrows correspond to the cooldown and heating processes.

3.1.3. Di-functionalised Poly(ethylene glycol)

Regarding the biocompatibility, biodegradability, and non-toxicity[152,153] of CS, CS-based hydrogels have been extensively studied. CS cross-linking has been mainly achieved by chemical approaches, namely the use of small dialdehydes, such as glutaraldehyde and glyoxal.[182–184] However, toxicity concerns about these small dialdehydes limit its use in pharmaceutical applications.[185–187] In the search for safe and non-toxic cross-linking agents, poly(ethylene glycol) (PEG) appears as a promising molecule since it is known to be a non-toxic, biocompatible, water-soluble, non-antigenic, and non-immunogenic polymer.[188,189] Therefore, PEG is widely used in biomedical and pharmaceutical applications, and several PEG-based products were already approved by the Food and Drug Administration (FDA).[188] Moreover, PEG is highly soluble in organic solvents, and therefore, its chemical modification, such as the preparation of PEG dialdehyde-derivatives, is relatively easy.[189] Keeping this in mind, Zhang *et al*.[190] developed a PEG-based cross-linker through functionalization of the hydroxyl terminal groups of PEG chain with benzaldehyde groups, as schematized in Figure 25. The choice of benzaldehyde groups relies on the enhanced stability of the aromatic Schiff base regarding the aliphatic Schiff base.[191] As previously stated, in Schiff base linkage there is an inherent dynamic equilibrium between the aldehyde and amine of the PEG cross-linker and CS, respectively. Therefore, the cross-linking made by this di-functionalized (DF)-PEG is a dynamic cross-linking, imparting the hydrogel with self-healing ability. Moreover, given the pH sensitivity of Schiff bases, the prepared hydrogel shows a pH-sensitive behaviour. The DF-PEG cross-linker was synthesised by a Steglich esterification (see Figure 25). N, N'-Dicyclohexylcarbodiimide (DCC) was used to help the formation of a stable intermediate and 4-dimethylaminopyridine (DMAP) as a catalyst.[190] The product obtained was characterised by ^{1}H NMR and FTIR.

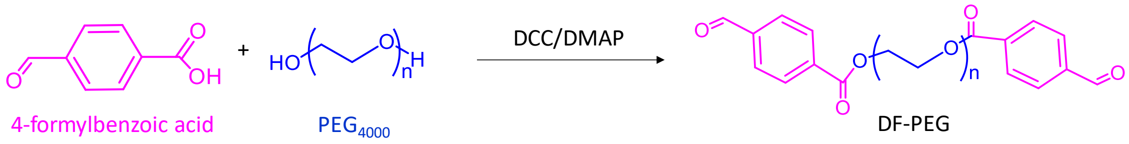

Figure 25 – Reaction scheme of the PEG functionalization reaction. "n" represents the number of repeating units in PEG; in this case (the molecular weight of PEG is 4000 Da), n is around 90.

The ^{1}H NMR spectrum of DF-PEG (Figure 26) displays a multiplet from 3.87 to 3.38 ppm ascribed to the ether methylene protons on the PEG backbone. The spectrum also displays some new peaks attributed to the aldehyde (at 10.12 ppm), benzene ring (from 8.20 to 8.12 and 8.11 to 8.02 ppm), and ester methylene (from 4.47 to 4.40 ppm). The presence of these new peaks along with the absence of the peak around 4.56 ppm,[192] usually ascribed to the hydroxyl group in PEG, confirms the success of the functionalization reaction. Moreover, by integrating and normalising the peaks from 3.87 to 3.38 ppm and at 10.12 ppm, it was estimated that around 79.4% of the PEG molecules were successfully modified with benzaldehyde groups at both ends.

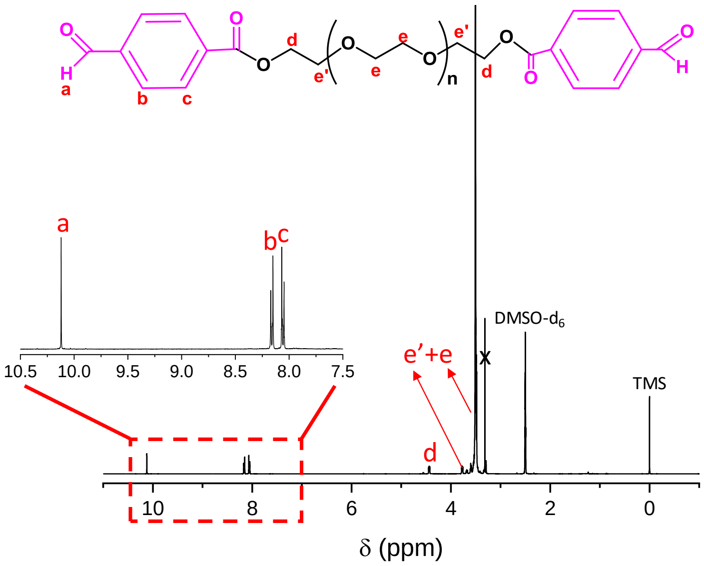

Figure 26 – ^{1}H NMR spectrum of DF-PEG in DMSO-d_6. In the inset is presented the structural formula of DF-PEG.

The FTIR spectra of PEG and DF-PEG (Figure 27) shows the characteristic bands of PEG, namely the peaks centred at 2886 cm^{-1} ascribed to the C-H stretching, at 1464 and 1341 cm^{-1} attributed to the C-H bending, and at 1280 and 1095 associated to the O-H and C-O-H stretching modes.[193] Moreover, the DF-PEG spectrum presents an additional band at 1712 cm^{-1} assigned to the aldehyde and ester carbonyls imparted by the functionalization reaction.[190] Thus, both ^{1}H NMR and FTIR data suggest the successful functionalization of the PEG molecules with benzaldehyde groups.

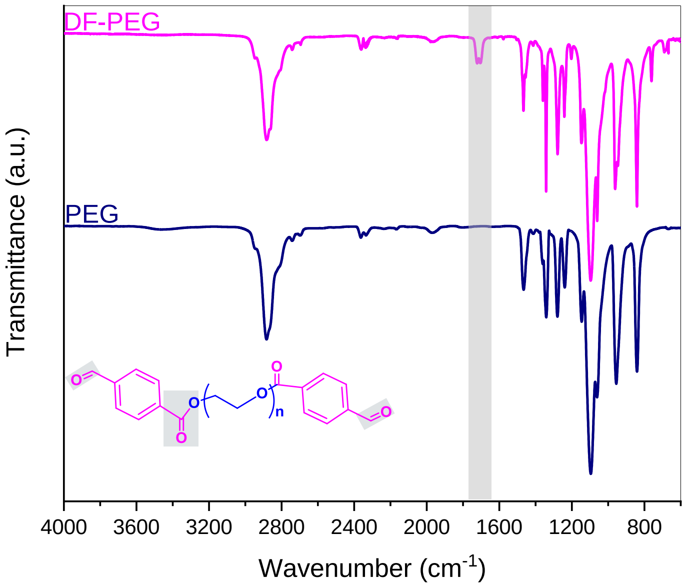

Figure 27 – FTIR spectra of PEG and DF-PEG. In the inset is possible to observe the structural formula of DF-PEG, with the aldehyde and ester carbonyls groups highlighted in grey. The grey band highlights the appearance of the mentioned groups in the DF-PEG spectrum.

3.2. Preparation and Characterisation of Hydrogels

As previously mentioned, this thesis aimed to develop an injectable and self-healing hydrogel able to be locally administrated and to synergistically perform chemo and photothermal therapy. Therefore, the prepared thermo-responsive polymer, CS-g-PNIPAAm, was dual cross-linked with DF-PEG and $\{Mo_{154}\}$, as it is possible to observe in the scheme of Figure 28. Due to its highly negative charge, $\{Mo_{154}\}$ contributes to the network formation by establishing electrostatic bonds with the protonated amine groups of CS. At the same time, as illustrated in Figure 28, the DF-PEG acts as a chemical cross-linker by the formation of reversible Schiff base among the benzaldehyde groups on DF-PEG and the amine groups on the CS backbone of CS-g-PNIPAAm. Briefly, all the components were mixed in aqueous solution for 30 sec using a vortex, and within less than 1 min, the hydrogel was formed. The gelation of the hydrogel was verified by the tube inversion test (Figure 29b).

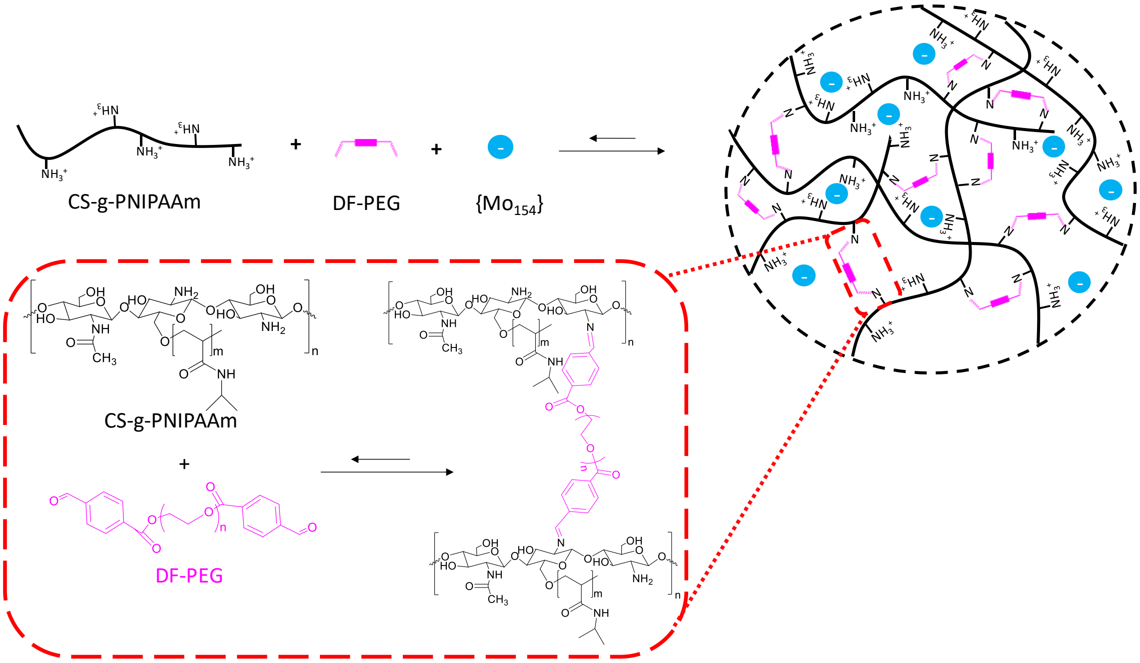

Figure 28 – Chemical structure scheme of the prepared hydrogel, namely the dynamic imine and electrostatic bonds responsible for the hydrogel cross-linking. The red rectangle shows a magnification of the reaction scheme of the reversible imine bond formation between CS-g-PNIPAAm and DF-PEG.

Figure 29a exhibits the UV-Vis spectra of the prepared hydrogel, $\{Mo_{154}\}$, and hydrogel control. The spectrum of hydrogel control shows no absorption band, information that agrees with the white/ transparent colour observed in Figure 29b. On the contrary, the spectrum of the hydrogel containing the $\{Mo_{154}\}$ anion showed one band centred at 745 nm, which is characteristic of the POM,[163] and that is in agreement with the hydrogel blue colouration observed in Figure 29b. This indicates the presence and structural integrity of the {Mo_{154}} in the prepared hydrogel. Furthermore, the strong absorbance in the NIR region, imparted by the presence of the POM in the hydrogel, is essential to confer photothermal conversion ability to the prepared formulation.

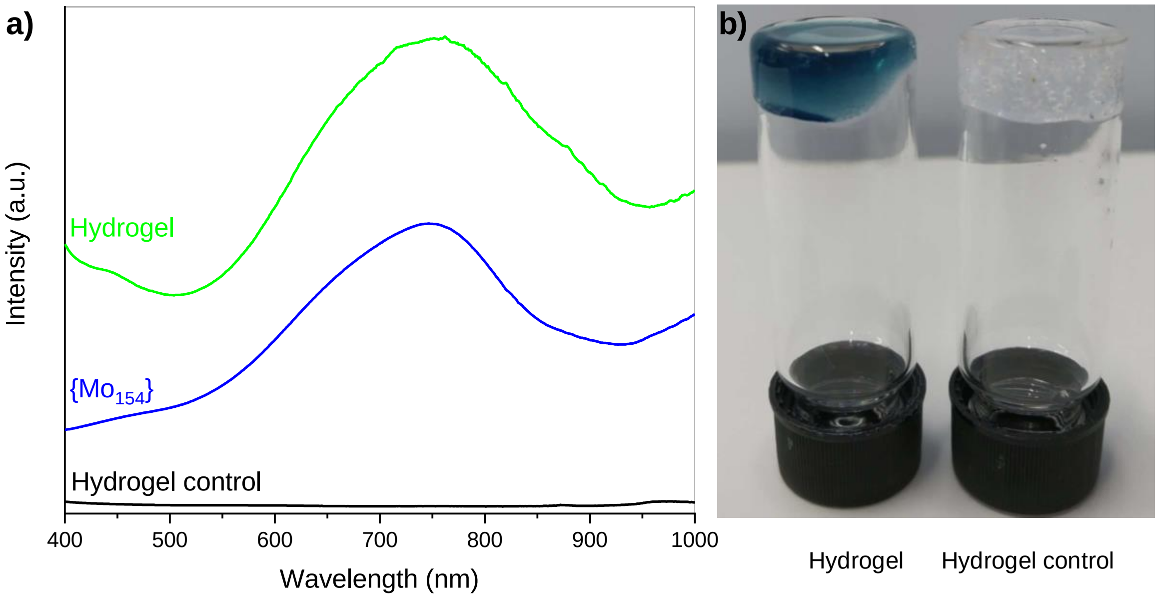

Figure 29 – a) UV-Vis spectra of the prepared hydrogel, {Mo_{154}} anion aqueous solution, and hydrogel control (without POM). b) Picture showing the blue colouration of the hydrogel and the white/ transparent colour of the hydrogel control.

FTIR spectroscopy was used to characterise the chemical composition of the prepared hydrogel (Figure 30). The FTIR spectrum of the hydrogel presents bands centred at 1639 and 1533 cm^{-1} previously ascribed to the amide I and II,[172,173] respectively, from PNIPAAm in CS-g-PNIPAAm, confirming the presence and structural integrity of this polymer in the prepared hydrogel. It is also possible to observe two bands centred at 1341 cm^{-1} attributed to the C-H bending, and at 1095 associated with O-H and C-O-H stretching characteristic from PEG.[193] Moreover, regarding the FTIR spectrum of DF-PEG, the spectrum of the hydrogel showed a decrease in the band at 1712 cm^{-1} assigned to the aldehyde and ester carbonyls of the DF-PEG, which confirmed that the aldehyde groups in the ends of the DF-PEG are involved in the imine bonds responsible for the cross-linking of the CS-g-PNIPAAm, as illustrated in Figure 28.

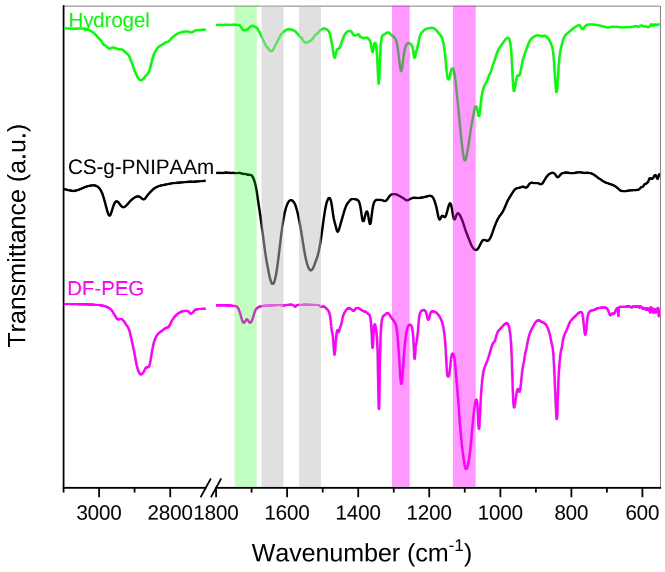

Figure 30 – FTIR spectra of the prepared hydrogel, CS-g-PNIPAAm, and DF-PEG. The green band highlights the decrease in the intensity of the band ascribed to the aldehyde and ester carbonyls. The grey and pink bands highlight the shared peaks among the hydrogel and CS-g-PNIPAAm or DF-PEG, respectively.

Raman spectroscopy was further used to confirm the presence of the {Mo$_{154}$} anion in the prepared hydrogel (Figure 31). The solid-state Raman spectrum of the hydrogel showed some of the characteristic bands of the hydrogel control (highlighted in grey). Besides, the spectrum of the prepared hydrogel showed some bands characteristic of the {Mo$_{154}$} centred at 534, 463, and 211 cm^{-1} (highlighted in blue).[163] Thus, confirming the presence of this POM in the formulation.

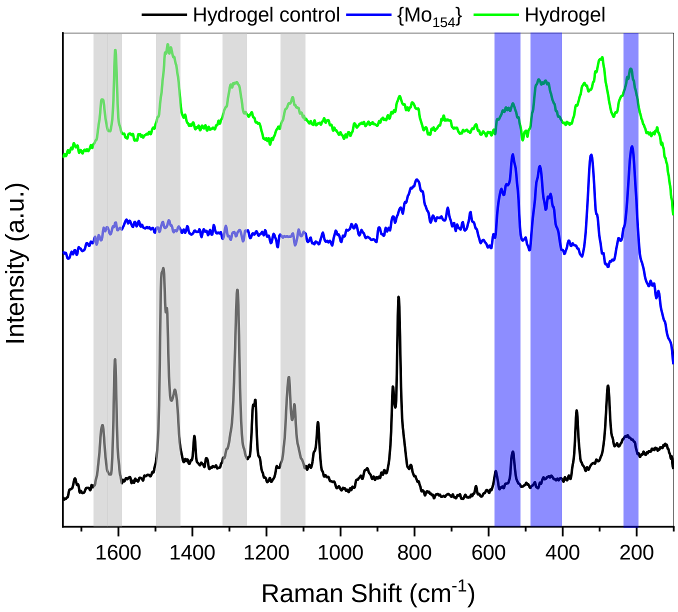

Figure 31 – Solid-state Raman spectra of hydrogel control, {Mo$_{154}$}, and the prepared formulation of the hydrogel (λ_e = 1064 nm). The characteristic Raman peaks of {Mo$_{154}$} and control shared with the hydrogel are highlighted in blue and grey, respectively.

To evaluate the morphology of the prepared materials, the hydrogels with and without POM were frozen, freeze-dried, and subsequently analysed by scanning electron microscopy (SEM; Figure 32a and 32b). Both hydrogels showed a porous structure without significative differences caused by the introduction of {Mo_{154}}.

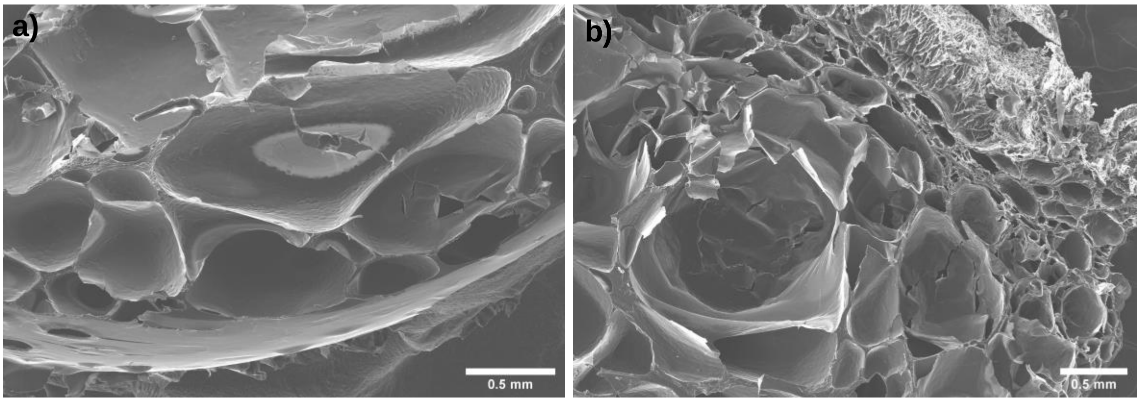

Figure 32 – SEM images of the a) hydrogel control (without POM) and b) hydrogel (with POM).

Through energy-dispersive X-ray spectroscopy (EDS) analysis (Figure 33a), it was possible to observe the appearance of the signal from Mo in the hydrogel relatively to the hydrogel control. This information confirms once again that Mo was successfully introduced in the hydrogel. Since there is no Mo signal in the hydrogel control spectrum, and given the remaining spectroscopic data discussed earlier, we can assume that this Mo is inserted in the form of {Mo_{154}}. Additional information about the spatial distribution of the {Mo_{154}} in the hydrogel was obtained by EDS mapping (Figure 33c to e). In Figure 33c and 33e, it is possible to observe that Mo is evenly distributed over the hydrogel.

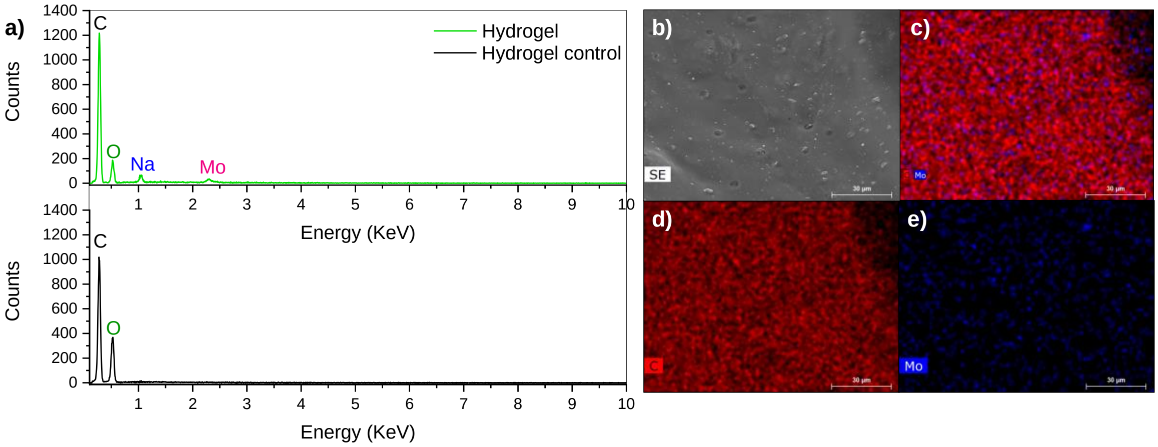

Figure 33 – a) EDS spectra of hydrogel and hydrogel control with the respective assignments of the elements detected. b) SEM image of the hydrogel surface analysed; c) EDS mapping of both C and Mo merged; and d) and e) EDS mapping of C and Mo, respectively. Scale bar – 30 µm.

DSC was used to determine the phase transition temperature of the hydrogel (Figure 34). The hydrogel showed an endothermic peak around 28 ºC associated with the phase transition, thus proving it thermo-responsiveness. Comparing this value with the value previously obtained for CS-g-PNIPAAm (31 ºC), it is noticeable a slight decrease. As above-mentioned, several factors affect the phase transition temperature of a polymer, namely the polymer concentration,[175] pH, the concentration of salts, and the presence of surfactants.[177] To further study the influence of the polymer concentration in the shift observed for the phase transition temperature, several polymer concentrations (0.5, 1.5, and 2.0 wt-%) were prepared and characterised by DSC (Figure 34). It is noticeable a slight decrease in the phase transition temperature of the polymer solution from 31.5 to 31 and 30 ºC, increasing the concentration from 0.5 to 1.5, and 2.0 wt-%, respectively. Moreover, a solution containing the same polymer concentration as the hydrogel, but without cross-linking (CS-g-PNIPAAm + PEG), was prepared aiming to study the behaviour of the total polymer concentration of the system and to verify if the cross-linking has some role in the observed shift of the phase transition temperature. The phase transition temperature value obtained in this case was 28 ºC, the same value obtained for the hydrogel. This led to the conclusion that the observed shift is a concentration-dependent effect: increasing the polymer concentration, the phase transition temperature decreases. This concentration-dependent effect was previously explained in the literature: increasing the polymer concentration, the width of vicinal immobilised water within interacting polymer chains decreases, leading to an improvement of the disruption action of the repulsive forces arising with the temperature increase.[180,194,195] Moreover, it can be concluded that the decrease in the phase transition temperature value is not due to the cross-linking of the hydrogel since the cross-linked and non-cross-linked systems have the same value.

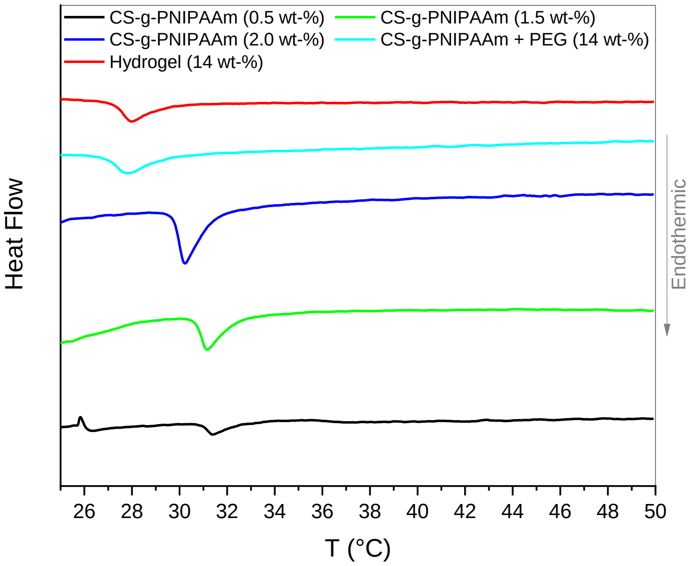

Figure 34 – Heat flow versus temperature for several CS-g-PNIPAAm solution concentrations, a solution of CS-g-PNIPAAm and PEG, and the hydrogel measured by DSC. The values in parentheses correspond to the total polymer concentration in each sample.

Due to its sensitivity and swiftness, rheology is a well-established and widely used method for the characterisation of the hydrogel's mechanical properties and architecture, such as degree of cross-linking.[196] The rheological measurements were carried out by displaying the initial components of the hydrogel in a parallel plate geometry, before gelation. A time sweep test was initially performed to monitor the gelation process (Figure 35). In the beginning, the samples are still in the liquid state, being the viscosity dominant, and thus, most of the energy is lost as viscous heat. Therefore, in the initial stage, G'' was larger than G'. With the increase of time, the polymer solutions started to gel through the cross-linking of the polymer chains, and therefore, both G' and G'' increased. However, the elastic properties of the system began to dominate, and thus, the rate of increase of G' was higher than that of G''. Therefore, there is an interception point, where G' becomes larger than G''. The time required for this interception is known as gelation time.[197] From Figure 35, it is possible to observe that the interception point of both control and hydrogel occurred in less than 50 sec. Considering the set-up time, it is possible to state that the gelation process occurred within 1 min. This value follows the previous one estimated by the tube inversion test and is comparable to the gelation times reported for this type of hydrogels (in the order of minutes).[190,198–200]

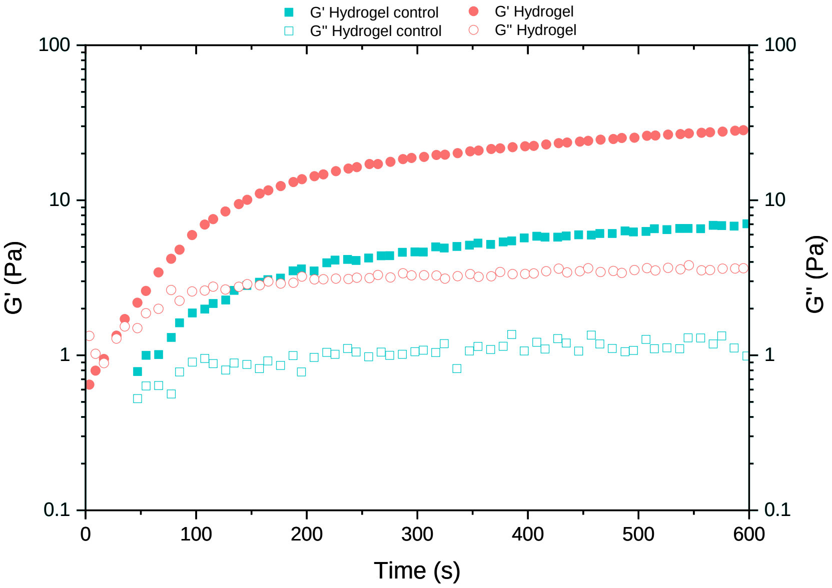

Figure 35 – Time sweep curves of the hydrogel control and hydrogel performed at 25 ºC and 1% of stress.

After the interception point, G' kept increasing until it reached its maximum value (7 and 30 Pa for control and hydrogel, respectively) and stabilised roughly after 3 min from the beginning of the experiment. This increase in storage modulus after the gelation was ascribed by Zhang *et al.*[198] to the hydrogel network formation, as well to the dynamic equilibrium of the imine (between the aldehyde and amine groups).

It is noticeable that the gelation occurred earlier in the hydrogel than in the hydrogel control and that both G' and G'' values of the hydrogel were larger than the ones of the control. Since the only difference among both hydrogels is the presence (or absence) of {Mo_{154}}, this effect can be ascribed to the formation of electrostatic bonds between the negative charge of the POM and the protonated amine groups of CS, as illustrated in Figure 28. The presence of these additional physical bonds makes the cross-linking process quicker and increases the hydrogel modulus (G' and G'') since it creates more cross-linking points within the components of the hydrogel.

Strain sweep assays were performed on both control and hydrogel, to determine and compare their G' and G'', as well as to assess the linear viscoelastic regime (LVR) (Figure 36). In LVR, stress and strain are proportional, and the G' *versus* strain curves assume constant values (plateau). In the LVR, the applied stresses are not enough to cause a structural breakdown or yielding of the structure. However, when the stress applied exceeds the yield stress, a non-linear region appears. Therefore, the limit of the LVR can be determined by the point at which the hydrogel structure starts to yield, corresponding to the point at which G' becomes dependent on the stress or strain.[201]

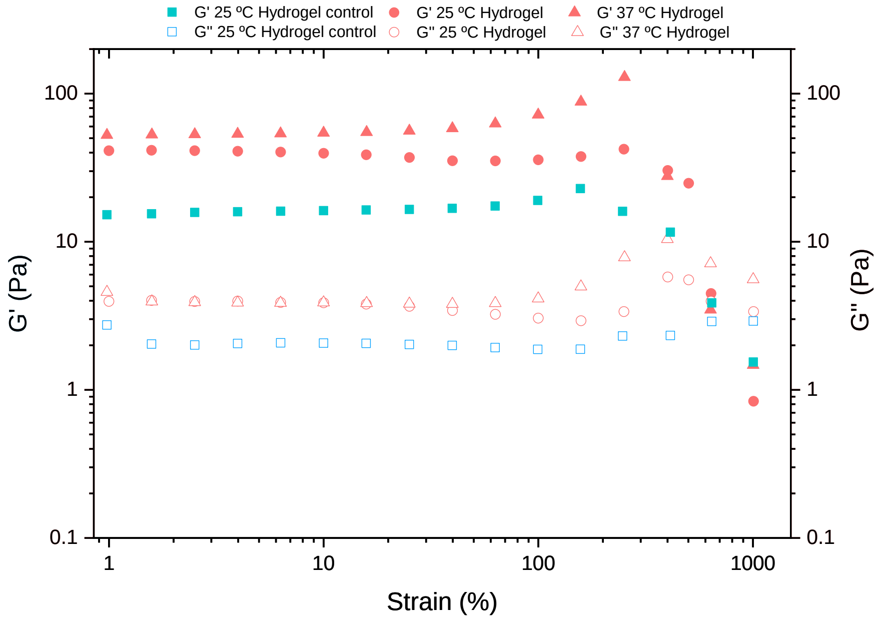

Figure 36 – Strain sweep curves of the hydrogel control (25 ºC) and hydrogel (25 and 37 ºC). The assay was performed at a constant frequency of 1 Hz.

The limits of the LVR determined from Figure 36 were: 160%, 256%, and 102% strain for the hydrogel control (25 ºC), and hydrogel at 25 and 37 ºC, respectively. It is noteworthy that the rupture point occurs at lower strains for hydrogel control than for hydrogel, which can be indicative of the strengthening of the hydrogel by the addition of the POM. This effect may be due to the higher degree of cross-linking in the hydrogel with {Mo_{154}} when compared to the hydrogel without POM, leading to the conclusion that the POM may be contributing to the hydrogel network by forming additional electrostatic interactions. Similarly to the reported in Figure 35, before break, G' assumes the values of 15 and 40 Pa in the plateau of hydrogel control and hydrogel, respectively, supporting the premise of the additional cross-linking by the POM.

Regarding the hydrogel behaviour at different temperatures, it was observed that at 37 ºC G' assumed a value slightly higher (50 Pa) than at 25 ºC (40 Pa) and that the linearity was lost earlier (102% strain).

Frequency sweep tests were also performed for the hydrogel control (at 25 ºC) and hydrogel (at 25 and 37 ºC), keeping constant stress of 1% (Figure 37). It was observed that G' remained almost constant for all the frequencies and was very similar for both temperatures, being again smaller for the hydrogel control. Simultaneously, G'' showed some variation regarding the frequency variation. For a covalently bonded hydrogel, both G' and G'' values remain constant at all frequency values. However, this variation in G'' can indicate that the hydrogel network is formed by dynamic cross-linking instead of a rigid covalent cross-linking.[198] This information is in agreement with the data analysed previously since both Schiff base and electrostatic bonds are dynamic bonds. The dynamic cross-linking is fundamental for the self-healing ability of a hydrogel because it allows the quick bound formation after the break or the damage.

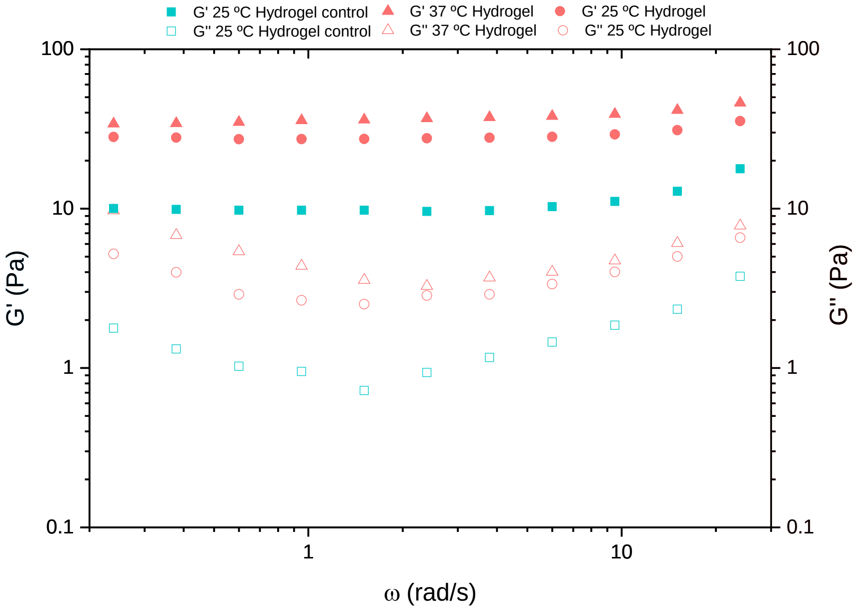

Figure 37 – Frequency sweep curves of hydrogel control (25 ºC) and hydrogel (25 and 37 ºC). The assay was performed at a constant strain of 1 %.

To evaluate the self-healing behaviour of the hydrogel in a quantitative way, a step strain measurement was carried out by applying a strain (1000%), higher than the limit of the LVR previously determined, for 2 min, followed by the application of a low strain (1%), in 4 cycles (Figure 38). With the increase of the strain from 1% to 1000%, the G' decreased from around 45 to 1 Pa due to the breakdown of the imine bonds.[190,199,202] In all the cycles, when the high strain (1000%) was removed, and the low strain (1%) was applied, both G' and G'' exhibited total recovery within few seconds. The fast recovery of the hydrogel is explained by the reversible behaviour of the imine and electrostatic bonds. These types of bonds are highly reversible and act as sacrificial bonds breaking at high stress, but readily reforming after the removal of the stress. Therefore, the dynamic equilibrium exhibited by both the Schiff base and electrostatic bonds helps the quick stabilisation of the hydrogel network under stress and allows the fast recovery (healing) of the hydrogel.[199]

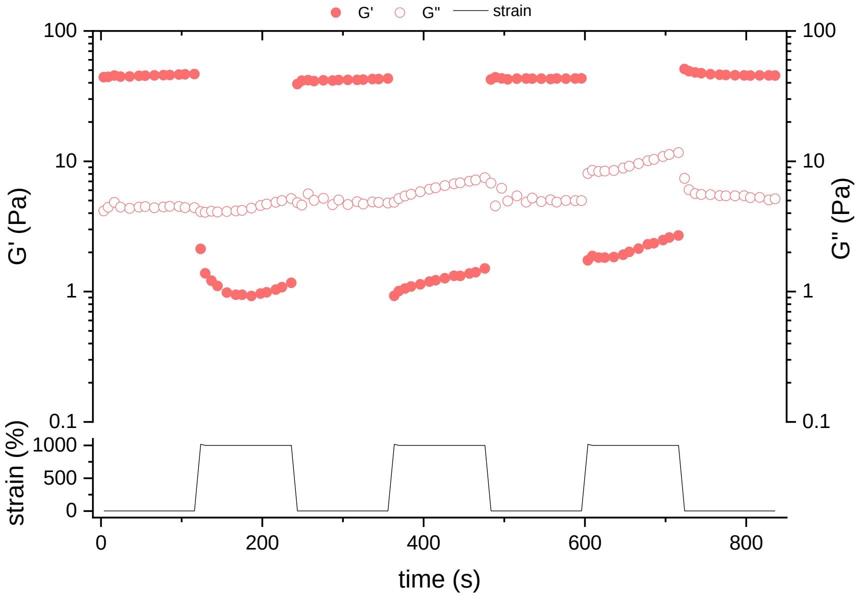

Figure 38 – G' and G'' in continuous step strain measurements (cycles of 1% and 1000% of strain).

To further evaluate the self-healing ability of the prepared hydrogel, a macroscopic self-healing test was performed by punching a hole in a freshly prepared hydrogel. Figure 39a displays the moment t=0 min, when the hole was punched. After 4 min at room temperature (Figure 39b), it was observed that the hole was completely closed, indicating an efficient self-healing and consequently the repair of the cross-linked network. The hydrogel prepared in the present thesis showed an improvement regarding the reported by Zhang *et al*.[190], which takes 2 h until complete recover. However, this sacrifices the mechanical strength, which decreased from 1150 to 40 Pa. The combination of a high self-healing efficiency and a high mechanical strength is usually hard since the high mechanical strength requires stable and strong bonds, which restrict the mobility of the polymer chains, slowing down the recovery process.[199] This limits the use of the hydrogel to applications where high mechanical strength is not required.

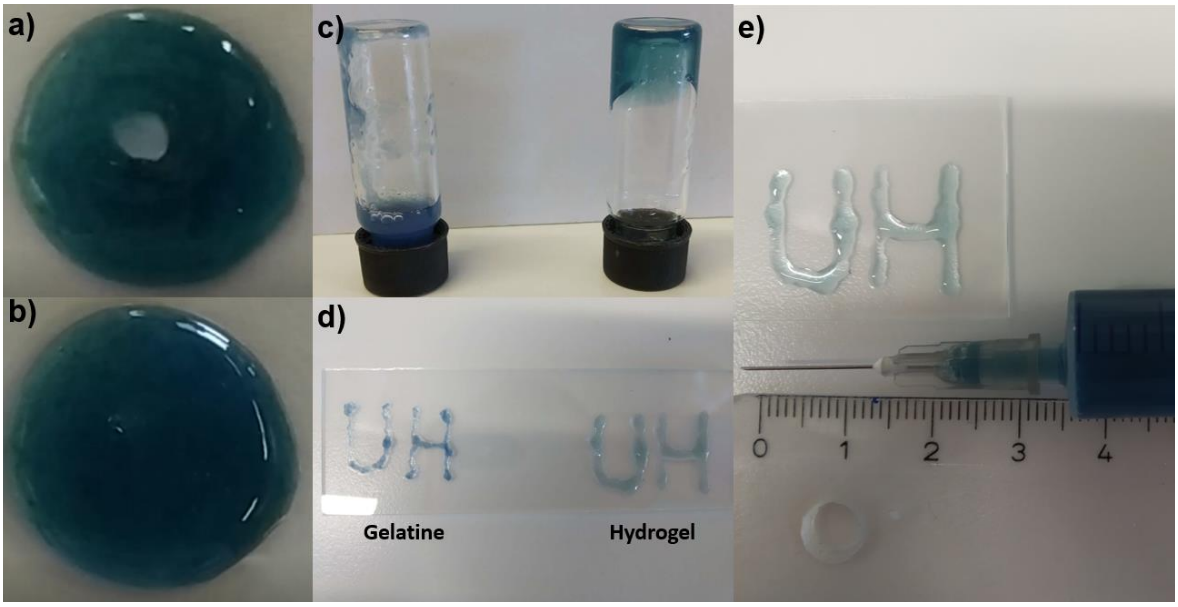

Figure 39 – Self-healing and injectability. a) and b) picture of the hydrogel right after punching a hole (~1 cm) and 4 minutes after, respectively. c) gelatine and hydrogel 5 min after being extruded into 2 mL of HBSS-HEPES. d) gelatine and hydrogel extruded through a syringe. e) enlargement of the picture of the hydrogel extruded using a syringe and photo of the syringe and needle used.

According to the rheological data obtained (Figure 36 and Figure 38), the hydrogel showed a fluidic behaviour under high shear strain (G'<G''), recovering instantaneously when the stress is removed. Therefore, the hydrogel is suitable to be used as an injectable hydrogel. To further study its injectability, gelatine and hydrogel were extruded through a syringe. Gelatine was chosen due to its well-known hydrogel properties, which do not exhibit self-healing properties. In a first assay, the gelatine and the hydrogel were extruded through a syringe into 2 mL of a buffer solution (Hank's balanced salt solution – 4-(2-hydroxyethyl)-1-piperazineethanesulfonic acid (HBSS–HEPES)). As it is shown in Figure 39c, the hydrogel healed to reform a whole piece within 5 min, while the gelatine was dissolved. This result further proves the remarkable self-healing ability of the prepared hydrogel. In a different test, the letters "UH" were successfully written using the hydrogel, showing a uniform structure as a unique piece (Figure 39d and 39e), confirming, again, the injectability of the prepared hydrogel. The letters drawn with gelatine did not form a unique piece, as it was expected.

When the hydrogel was squeezed in the syringe, the pressure induced the dissociation of the imine and electrostatic bonds, causing the hydrogel to deform and "flow" as a liquid to pass through the needle. Right after the extrusion, the hydrogel came together to form a unique piece due to its rapid self-healing ability. This behaviour indicates that the developed hydrogel has potentialities to be implanted through a minimally invasive injection.

3.3. *In vitro* Release Studies

One of the main objectives of this thesis was the development of a drug delivery system, able to locally deliver different types of cargo molecules, such as small drugs and proteins. For this purpose, the release of two model drugs, doxorubicin (DOX) and horseradish peroxidase (HRP), were investigated.

DOX is a widely known antineoplastic antibiotic[203] which presents an orange colouration and a strong fluorescence. Therefore, both UV-Vis absorption spectroscopy and fluorescence can be used in the detection of this drug. Initially, to verify the absorption maximum of DOX, the UV-Vis spectra of DOX solutions (pH 5.5 and 7.4) were recorded. From the spectra shown in Appendix 1, it was determined that the wavelength at which the absorption maximum occurs is 480 nm, for both pHs. Then, before performing its release, it was necessary to determine the range of linearity in which DOX can be quantified and the equations to make that quantification. For this, calibration curves for both pH-values were done by measuring either the fluorescence or the absorption (Appendix 2 and Appendix 3). It was found that the absorption had a linear behaviour for concentrations from 1 to 100 μg/mL. When the detection method was the fluorescence, the values were linear only from 0.01 to 10 μg/mL. Since the fluorescence exhibited a lower detection limit and a linear behaviour closer to the range of values being used, this was the method selected for the detection of DOX in the release study.

Briefly, the DOX-loaded hydrogels were prepared in 50 mL tubes, and after gelation, 1.5 mL of buffer (HBSS-HEPES, pH 7.4 or HBSS-MES (2-(N-morpholino)-ethanesulfonic acid), pH 5.5) was added and kept either at room temperature (RT) or 37 °C. Three replicas were prepared for each condition studied. Then, aliquots of the release medium were removed, diluted, stored in the fridge in the dark, and analysed at the end of the experiment. The samples were analysed by measurement of the fluorescence using a plate reader and then quantified using the calibration curves previously determined. Simultaneously, controls were prepared in the same way, but without encapsulating the DOX in the hydrogel (Appendix 4).

Figure 40a shows the DOX release profiles of the DOX-loaded hydrogels at RT and 37 ºC, at pH 7.4. During the first hour of incubation, it was observed an initial burst release of about 47% and 23% of the drug from the hydrogel at 37 ºC and room temperature, respectively. The observed burst release may be explained by the rapid expulsion of weakly attached drugs on the outer surface of the hydrogel.[204] At 37 ºC, DOX was quickly released within 2 h (~84%) and then the release rate slowed down after 6 h (~97%), achieving the equilibrium. However, as expected, at RT the release rate slowed down after 1 h, and the release continued to increase slowly, reaching 62% of drug release after 24 h.

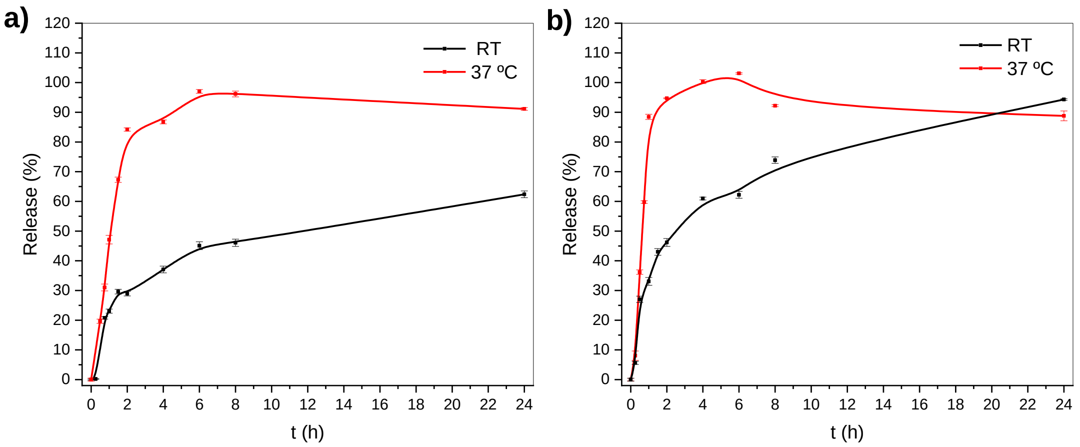

Figure 40 – In vitro doxorubicin release profiles from doxorubicin-loaded hydrogels. A drug release study was performed at room temperature and 37 °C and a) pH 7.4 and b) pH 5.5. The full line represents a B-Spline fitting and the error bars represent the standard deviation of each point.

To study the influence of the pH in the release behaviour of the hydrogels, the release was also performed at pH 5.5 (Figure 40b). The hydrogels showed a burst release in the first hour, having released around 33% and 85% at RT and 37 ºC, respectively. After this burst release, the release rate slowed down and 100% of the DOX was released after 6 h at 37 ºC. At RT, the release reached around 62% of drug released within 6 h, and 94% after 24 h. Overall, the release at room temperature was faster and more complete at pH 5.5 than at pH 7.4.

Additionally, to study the ability of the hydrogel to deliver/release a different type of molecule, namely a protein, HRP was encapsulated in the hydrogel and allowed to be released in buffer solutions with two distinct pH (7.4 and 5.5). HRP is a glycoprotein that oxidises a wide variety of inorganic and organic compounds by using oxygen,[205,206] and that has been commercially used for immunoassays and as a component of clinical diagnostic kits.[206] HRP was chosen as model-protein payload for this study due to its ability to catalyse the conversion of a non-fluorescent substrate in a fluorescent molecule, able to be detected quickly and straightforwardly by a plate reader. The release experiment was performed as previously described for DOX, except for the detection/quantification. The amount of HRP released was determined from a relation derived from the Michaelis-Menten equation:

$$v0 = K[E]$$

where v_0 is the initial reaction rate, K is a constant, and $[E]$ the enzyme concentration (for a more detailed explanation, please see Materials and Methods). This equation relates v_0 with the concentration of the enzyme, allowing the quantification of HRP present in each sample. The reaction being screened was the conversion of a substrate (Amplex^{TM} UltraRed) in a fluorescent molecule, catalysed by HRP in the presence of hydrogen peroxide. Then, v_0 was determined from the slope of the graph of the fluorescence intensity *versus* time (the fluorescence intensity was measured at each 30 sec, during the first 4 min of reaction). Initially, calibration curves were determined by plotting v_0 against the known HRP concentration of the patterns prepared for each buffer (Appendix 6). Then, the procedure described above was applied to all the samples, and the v_0 determined to each time point, allowing the determination of the amount of HRP released.

Figure 41a shows the HRP release profiles from HRP-loaded hydrogels at RT and 37 ºC, at pH 7.4. At RT, there is almost no release with only 12% of HRP being released after 24 h. In contrast, at 37 ºC there is a burst release in the first hour of experiment with 28% of HRP released. After the first hour, the release slowed down but kept increasing until 24 h, until it reached 95% of HRP released.

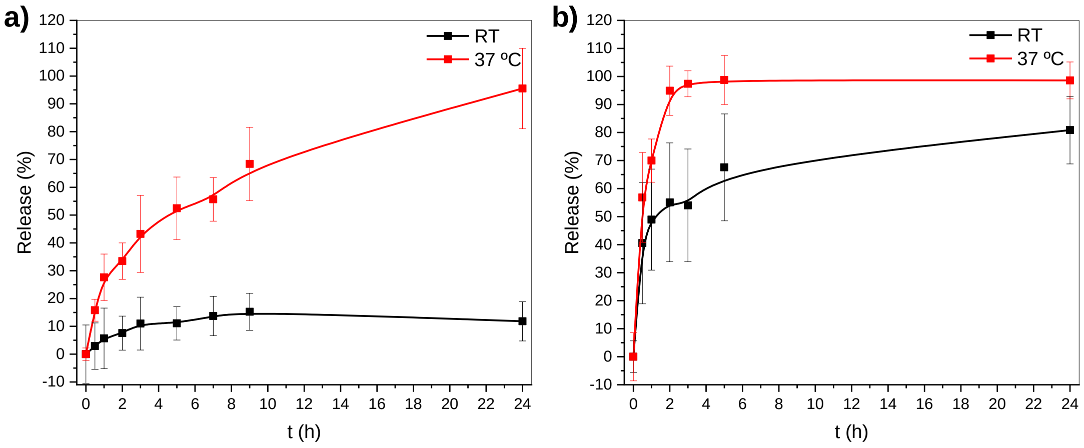

Figure 41 – In vitro HRP release profiles from HRP-loaded hydrogels. A drug release study was performed at room temperature and 37°C and a) pH 7.4 and b) pH 5.5. The full line represents a B-Spline fitting, and the error bars represent the standard deviation of each point.

Once again, to study the influence of the acidic pH in the cargo release, the experiment was performed in HBSS-MES, with pH 5.5 (Figure 41b). Differently to the observed for pH 7.4, in acidic pH, the hydrogels showed an initial burst release in the first half-hour with 41% and 57% at RT and 37 ºC, respectively. The release rate slowed down within two hours, being the percentage of HRP released 55% and 95% at RT and 37 ºC, correspondingly. Then, the release at RT continued to increase slowly, reaching 81% in 24 h. The release at 37 ºC reached the equilibrium after 3 h with 97% of release and almost no change until the 24 h, where the percentage of HRP released was 99%.

The release profiles of DOX and HRP showed similar behaviour for all the conditions. However, the DOX release profiles showed a faster release rate when compared with those from HRP. This aspect can be explained by the difference in molecular weight of DOX and HRP (543.5 g/mol[203] and 40000 g/mol,[207] respectively), which allows DOX to diffuse faster. For both molecules and pH-values investigated, the release rate was significantly higher at 37 ºC (above LCST) than at RT (below LCST). This can be attributed to the volume phase transition exhibited by CS-g-PNIPAAm above the LCST. The collapse of the PNIPAAm chains from the coil to a globular structure leads to the hydrogel shrinkage,[81,137,140] and consequent cargo expulsion. The release in the hydrogels at RT occurs in a slower way depending only on free diffusion.

Considering now the distinct pH-values, it was noticed a significant increase in the release rate at pH 5.5 relatively to pH 7.4. This effect can be explained by the pH-responsive character of the CS and the imine bonds that cross-link the hydrogel network. CS, the backbone polymer of the thermo-responsive polymer prepared, is a polyelectrolyte with acidic ionizable groups, which can accept protons as a function of changes in the environmental pH. CS presents a pK_a of 6.5,[208] and therefore by changing the pH across this pH threshold, the amine groups on CS backbone will be protonated, generating repulsive electrostatic forces, which will cause an increase of the hydrodynamic volume of the polymer and consequently the swelling of the hydrogel. The imine bonds (or Schiff bases) are acid-labile,[147] which undergo cleavage in acidic pH-values, leading to the release of loaded drug molecules. The pH-responsiveness of the hydrogel is an important property since the tumour microenvironment usually present acidic pH,[130,141] allowing the spatial control of the release.

Therefore, it was concluded that regardless of the molecule used in the release experiment, the developed hydrogel showed thermo- and pH-responsive properties.

3.4. Cytotoxicity Studies

The *in vitro* cytotoxicity of the initial components was evaluated in human melanoma cells (M21), using a metabolic assay (Alamar Blue®). Figure 42 shows the plots of the viability *versus* the concentration of CS-g-PNIPAAm. For concentrations up to 0.5 mg/mL, the polymer showed low cytotoxicity, since the viability was always higher than 75% for 4 and 24 h of incubation. However, for a concentration of 1 mg/mL and 24 h of incubation, the viability decreases significantly to 29%. Thus, this concentration was considered cytotoxic. A disadvantage of the direct grafting method used in this thesis is the excessive formation of PNIPAAm homopolymer, *i.e.*, PNIPAAm not grafted on the chitosan backbone.[180] Thus, the cytotoxicity showed by CS-g-PNIPAAm can be explained by the presence of free

PNIPAAm homopolymer in the solution, which exhibited a significant decrease of viability at concentrations higher than 0.5 mg/mL, as previously reported.[209]

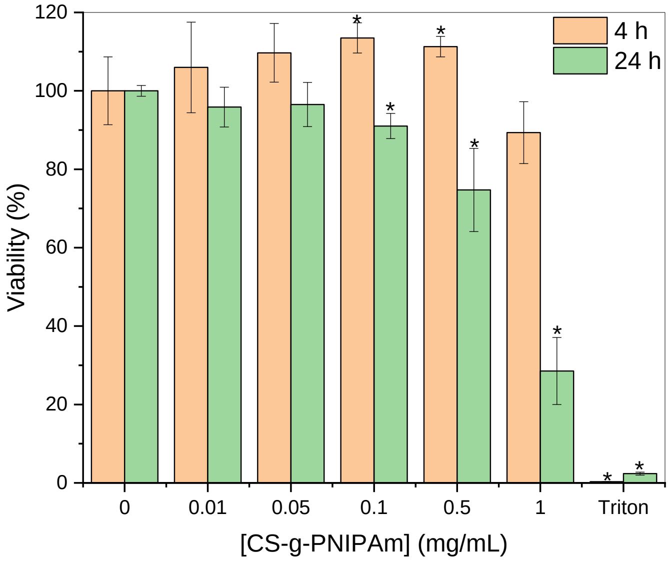

Figure 42 – Cell viability of M21 cell line when incubated with different concentrations of CS-g-PNIPAAm for 4 and 24 h (denotes significative differences with a significance level of 0.05, the statistical analysis was done using OneWay ANOVA).*

In Figure 43 is shown the cell viability data obtained for several concentrations of DF-PEG incubated with M21 cells during 4 and 24 h. The cell viability was always above 80% for all concentrations up to 5 mg/mL, and therefore, DF-PEG can be considered to present low cytotoxicity in this concentration range. Only for 24 h of incubation at higher concentration (10 mg/mL), there was a decrease in cell viability to around 50%. Thus, DF-PEG can be considered to present some cytotoxicity only at high concentrations.

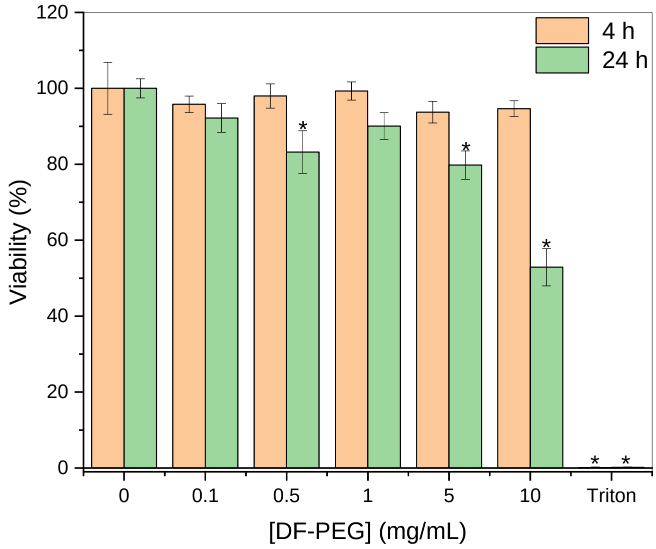

Figure 43 – Cell viability of M21 cell line when incubated with different concentrations of DF-PEG for 4 and 24 h (denotes significative differences with a significance level of 0.05, the statistical analysis was done using OneWay ANOVA).*

Figure 44 shows the columnar plots of the viability *versus* the concentration of {Mo_{154}}. It was observed that the cell viability had no significant decrease at 4 and 24 h for almost all concentrations, except for the two higher concentrations that showed a decrease in cell viability to around 20% at 24 h. Besides, the higher concentration (1.67 mg/mL) also showed a decrease in cell viability at 4 h of incubation. These results demonstrate the low cytotoxicity of this POM to concentrations up to 0.42 mg/mL. This concentration was below the concentration used in the hydrogel (1.67 mg/mL). However, in the hydrogel, the {Mo_{154}} was entrapped in the hydrogel matrix by electrostatic interactions, and therefore, even if there was leakage of the POM, it was expected not to reach such high concentrations.

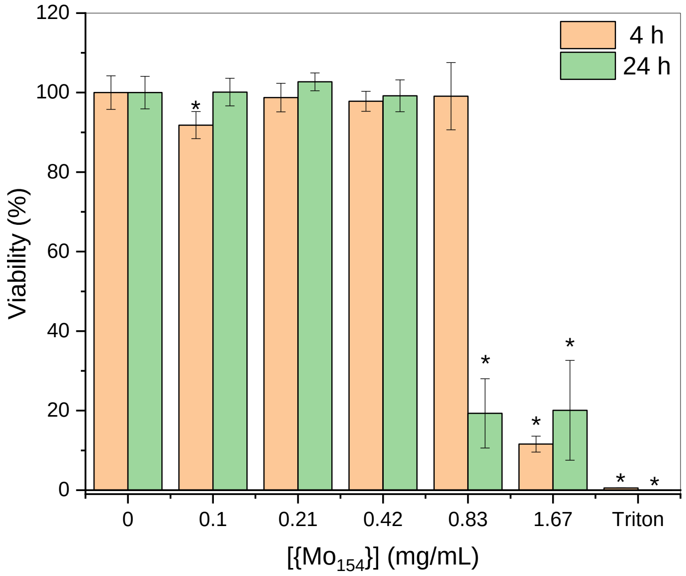

Figure 44 – Cell viability of M21 cell line when incubated with different concentrations of {Mo_{154}} for 4 and 24 h (denotes significative differences with a significance level of 0.05, the statistical analysis was done using OneWay ANOVA).*

To study the cytotoxicity of the hydrogel control and the hydrogel, M21 cells were seeded in a 24-well Transwell® plate and the hydrogels incubated with the cells during 4 and 24 h. The biocompatibility of the hydrogels was evaluated using an ATP based luminescent cell viability assay (CellTiterGlo®). The results of this assay are presented in Figure 45. Both hydrogel control (without POM) and hydrogel (with POM) showed no significant decrease in the viability of the M21 cell line, decreasing only slightly after 24 h (to 83% and 90%, respectively). Moreover, there was no significant difference between the results obtained for hydrogel control and hydrogel, indicating that there was no additional toxicity coming from the incorporation of the {Mo_{154}}. This result confirms that despite the initial components of the hydrogel showed some toxicity at higher concentrations, when incorporated in the hydrogel this toxicity was prevented, resulting in a final material that presents low cytotoxicity.

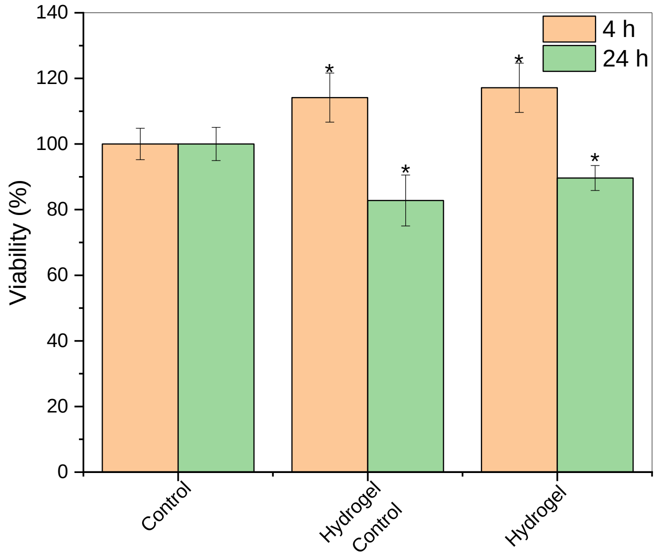

Figure 45 – Cell viability of M21 cell line when incubated with hydrogel with and without {Mo_{154}} for 4 and 24 h (denotes significative differences with a significance level of 0.05, the statistical analysis was done using OneWay ANOVA).*

3.5. Photothermal Conversion Studies

As previously discussed, the absorption spectrum of the hydrogel showed a band centred at 745 nm, characteristic of the {Mo_{154}} (Figure 29b). The strong absorbance in the NIR region imparted by the presence of the POM in the hydrogel is essential to confer photothermal conversion ability to the formulation, which will be discussed in this section. The maximum absorption band centred at 745 nm, indicates that the wavelengths of radiation usually used for photothermal therapy (around 808 nm) are applicable to {Mo_{154}}. Moreover, a study previously published proved that {Mo_{154}} composites exhibited a photothermal conversion efficiency (30.9%) comparable to or higher than the materials usually used as photothermal agents, such as gold nanoparticles in different shapes (12-22%).[64] This information shows the viability of the use of {Mo_{154}} as a photothermal agent.

To evaluate the photothermal conversion ability of the prepared hydrogel, hydrogels prepared with different {Mo_{154}} concentrations were irradiated for 10 minutes with a laser (785 nm) with an irradiance of 0.1 W/cm^2 at RT (~25 ºC). The temperature was measured with a thermocouple and recorded in intervals of 30 sec. The photothermal conversion curves obtained are shown in Figure 46. The concentration 0 wt-% corresponds to the hydrogel control, *i.e.*, without POM, and served as a blank. After 10 min of laser irradiation, this hydrogel presented a temperature increase of only 2 ºC. Using different concentrations of {Mo_{154}} (0.7, 1.4, 2.7, and 5.4 wt-%), it was observed an increase of 15, 23, 31, and 32 ºC relatively to the initial temperature. Given the increase in the temperature and the data on cytotoxicity previously obtained, the hydrogel with 2.7 wt-% of {Mo_{154}} was the formulation chosen to be used as the final formulation. Furthermore, it is noteworthy that the power density used in this experiment (0.1 W/cm^2), was lower than those being described in the literature (mostly between 0.28 and 5.8 W/cm^2) for the same increase in temperature (~30 ºC).[64,210–214]

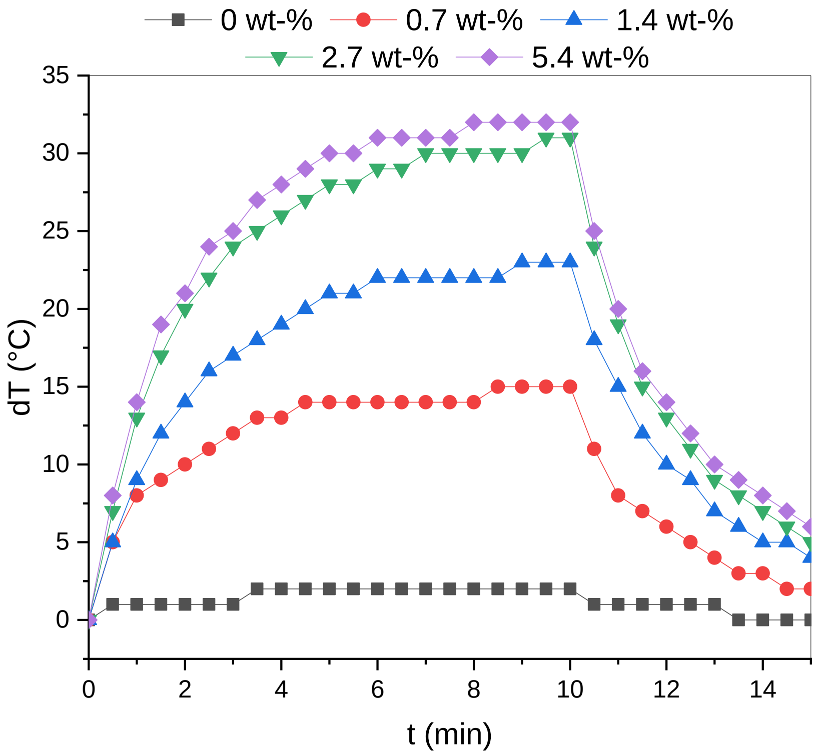

Figure 46 – Photothermal conversion curve of the hydrogels with different concentrations of {Mo$_{154}$} irradiated for 10 min at an irradiance of 0.1 W/cm^2 (785 nm) and cooled down (laser off) for 5 min.

Figure 47 shows the comparison of the photothermal conversion curves of the hydrogel with 2.7 wt-% of {Mo$_{154}$} and the same amount and formulation of the hydrogel, but in the cell setup (*i.e.*, with the hydrogel in the Transwell® and 1 mL of HBSS-HEPES in the well) performed by measuring the temperature increase of the buffer solution. By observing these graphs, it was concluded that the increase of the temperature in the medium (HBSS-HEPES) was much lower than the observed in the hydrogel. When the hydrogel is surrounded by the medium, it will probably lose energy as heat to the medium, heating it. However, the heat being produced in the hydrogel may not be enough to cause the temperature increase required (~22–25 ºC, if the starting temperature is the RT). Therefore, it was necessary to study the photothermal conversion ability of the hydrogel when exposed to higher power density/current values.

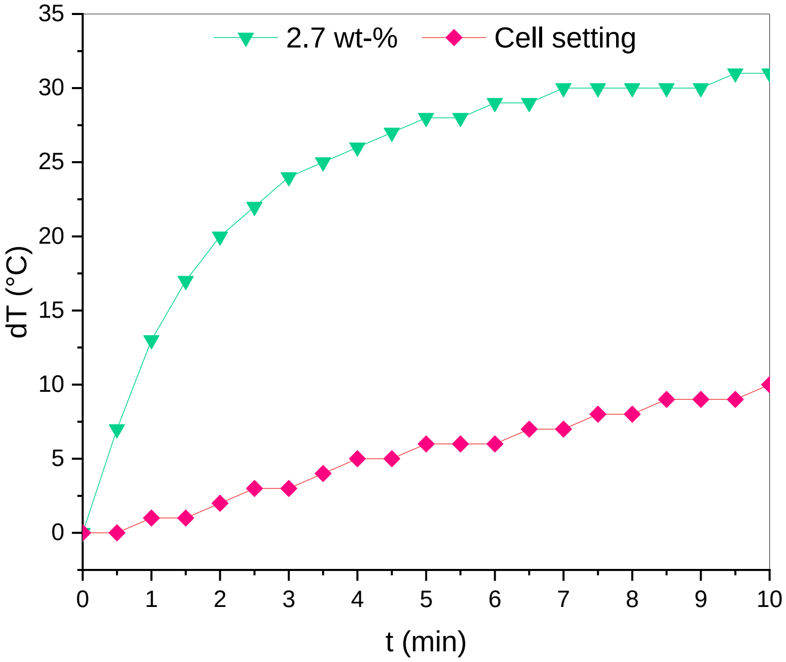

Figure 47 – Photothermal conversion curves of the hydrogel (2.7 wt-% of {Mo_{154}}) measured directly in the hydrogel and in the setting used for the cell experiment (hydrogel in the Transwell® and 1 mL of HBSS-HEPES in the well) irradiated for 10 min at an irradiance of 0.1 W/cm^2 (785 nm).

To study its photothermal conversion ability, the prepared hydrogel was irradiated with different irradiance values. To do that, a laser (808 nm) with tuneable current outputs, and then irradiance values, was used. The data obtained is shown in Figure 48a.

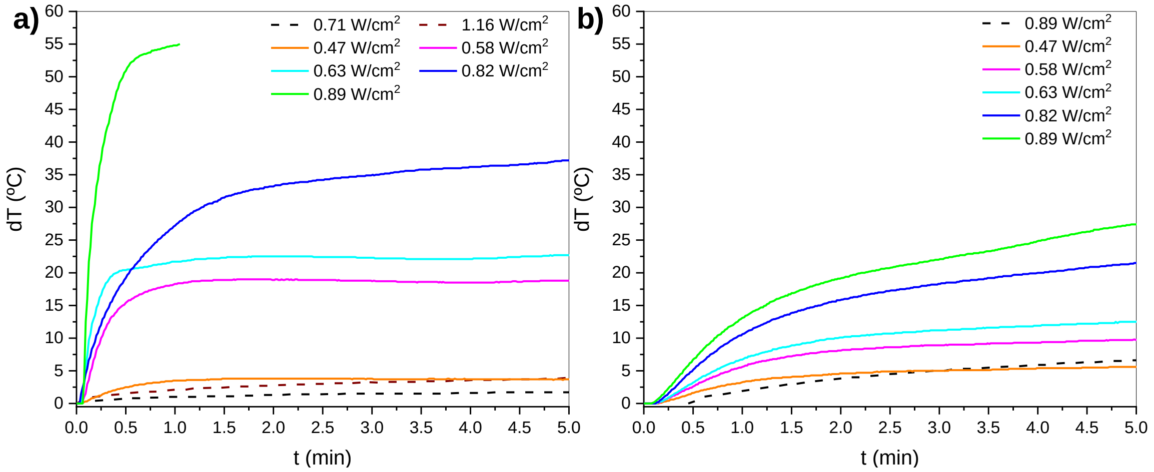

Figure 48 – Photothermal conversion curves of the a) hydrogels and b) {Mo_{154}} aqueous solutions with a concentration of 1.67 mg/mL under laser irradiation with different irradiance values (808 nm).Control hydrogel and water in dashed lines. Hydrogels with {Mo_{154}} and {Mo_{154}} aqueous solutions in coloured full lines.

As expected, increasing irradiances led to higher temperature increases for the same hydrogel formulation. It is noteworthy that the irradiance value used in this assay (0.82 W/cm^2) to reach a total temperature increase of ~37 ºC was higher than the previously used (0.1 W/cm^2). This can be explained based on the proximity of the emission/absorption wavelengths of the laser and the hydrogel. The maximum in the absorption spectrum of the hydrogel (775 nm) was closer to the wavelength of the laser initially used (785 nm) rather than of the second one (808 nm). Thus, when the laser with λ_e=785 nm was used, the absorption was higher, causing an improved photothermal conversion than when the laser with λ_e=808 nm was used.

Although the irradiance values used in this assay were higher than the previously discussed, they still were in the range of the values commonly described in the literature (0.28 and 5.8 W/cm^2).[64,210–214] Moreover, comparing the results previously described in the literature for {Mo$_{154}$} anion,[64] the irradiance value here used was smaller (0.82 *versus* 1 W/cm^2). This small decrease in irradiance used can have important practical implications, since it allows the application of a smaller irradiation dose to obtain the same final output, decreasing the risks associated with the handling of high-power lasers.

Due to the high-temperature increase observed when the hydrogel was irradiated with 0.89 W/cm^2, the laser power was shut down after roughly 1 min due to safety issues.

The photothermal conversion curves obtained by measuring the temperature increase in a {Mo$_{154}$} aqueous solution with the same concentration of the hydrogel and irradiated with the same current values are shown in Figure 48b. It was observed that when in solution, this POM caused a much lower temperature increase (14 *versus* 55 ºC, when irradiated for 1 min with a current value of 0.89 W/cm^2). Therefore, when incorporated in the hydrogel, the POM showed an improved photothermal conversion regarding the POM solution. This phenomenon can probably be explained by the decreased energy losses by convection in the hydrogel relatively to the solution.

4. Conclusions and Future Work

In the present thesis, it was developed a self-healing and injectable hydrogel based on a thermo-responsive polymer (CS-g-PNIPAAm) double cross-linked by Schiff base, through a benzaldehyde di-functionalised PEG, and electrostatic interactions with $\{Mo_{154}\}$. The prepared hydrogel showed a dual temperature and pH-responsive behaviour towards the delivery of drug and protein model cargos.

The starting materials (CS-g-PNIPAAm, DF-PEG, and $\{Mo_{154}\}$) were prepared by adapting methods previously described in the literature. Their successful synthesis was confirmed by several techniques, such as ^{1}H NMR, FTIR, Raman spectroscopy, and UV-Vis. CS-g-PNIPAAm was further characterised by DLS and DSC, proving it thermo-responsiveness and phase transition temperature around 30 ºC.

The hydrogel was prepared by mixing CS-g-PNIPAAm, DF-PEG, and $\{Mo_{154}\}$ and was formed within 1 min, as verified by inversion test and confirmed by the time sweep assay. The rheological data confirmed the additional cross-linking provided by the electrostatic interactions among the negative charge of the $\{Mo_{154}\}$ and the protonated amine groups of CS. Moreover, the frequency sweep tests proved the dynamic nature of the bonds cross-linking the hydrogel network.

The dynamic cross-linking is essential for the self-healing ability of a hydrogel since it allows the quick bound formation after the break or the damage. This property was verified by the instantaneous recovery of the hydrogel in the step strain measurement and the macroscopic self-healing test, carried out by punching a hole (⌀~1cm) in a hydrogel, which healed within 4 min at RT. Moreover, the hydrogel showed to be injectable through a syringe, presenting a uniform structure as a unique piece after extrusion.

However, the combination of a fast self-healing ability with the high mechanical strength of the hydrogel is hard to achieve, since the last one requires stable and strong cross-linking bonds, which limits the mobility of polymer chains and slows down the recovery of the hydrogel network. This was noticed in the prepared hydrogel, which presented a low mechanical strength. An improved mechanical strength could beneficiate the integrity of the hydrogel when used in applications requiring high mechanical requirements. This point can be further exploited as future work, for example, by adding a covalent cross-linker to the system.

SEM images of the hydrogel indicated the presence of a porous structure, with no significative changes regarding the addition of the POM. EDS results further proved the presence of Mo, and ultimately $\{Mo_{154}\}$, in the hydrogel, and EDS-mapping showed that this POM is homogeneously distributed in the hydrogel.

DSC analysis confirmed the thermo-responsiveness of the prepared hydrogel, showing a phase transition temperature of 28 ºC. The phase transition temperature obtained was lower than the desired, and then, future work would be needed to study the chemical adjustment of the ratios of PNIPAAm and CS in the co-polymer, to try to reach a higher value, ideally around 42 ºC.

The suitability of the prepared hydrogel to deliver different types of molecules was evaluated by studying the release of a model protein (HRP) and a model drug (DOX). Regardless of the molecule used, the release profiles showed that the hydrogel is pH and temperature-responsive, being, therefore, suitable for the use as a targeted and controlled drug delivery system.

Despite its constituents exhibited some cytotoxicity for the higher concentrations, the prepared hydrogel showed low cytotoxicity. Furthermore, the prepared material presented improved photothermal properties being able to cause a temperature increase of around 35 ºC with low irradiance (0.1 or 0.82 W/cm^2 with an excitation wavelength of 785 or 808 nm, respectively). Moreover, when incorporated in the hydrogel, the POM exhibits an improved photothermal conversion regarding the POM solution.

The incorporation of $\{Mo_{154}\}$ in the hydrogel was profitable since it led to an enhanced photothermal conversion ability when compared to a $\{Mo_{154}\}$ aqueous solution and exhibited reduced cytotoxicity. Additionally, the hydrogel had exceptional self-healing and injectability performances, and further ability to delivery both protein and drug cargos in a targeted and stimuli-responsive way. Overall, the composite described in this thesis can be used in applications needing a dual (chemo and photothermal) combination therapy, delivered through an injectable hydrogel where *in situ* administration is needed.

As forthcoming work is suggested to study the temperature increase with the hydrogel in the setup with the transwell plates with distinct laser powers, to try to improve the data obtained here. Afterwards, it would be desirable to perform an assay with cancer cells to test the ability of the hydrogel to accomplish photothermal therapy for cell ablation. In the case this *in vitro* test shows promising results, *in vivo* studies could be performed to evaluate the synergistic photothermal and chemotherapy behaviour of the developed system, in mice or rat models.

5. Materials and Methods

In this section, the materials and methods used in this thesis are described.

5.1. Materials

{Mo_{154}}: Sodium dithionite ($Na_2S_2O_4$, 85+%), sodium molybdate oxide dihydrate ($Na_2MoO_4•2H_2O$ 99.5%), hydrochloric acid (1 M) were obtained from Alfa Aesar (Germany).

Polymers: Ammonium persulfate (APS, ≥98.0 %); chitosan (medium molecular weight, 75-85% deacetylated); deuterium chloride solution (35 wt-% in D_2O, ≥99 atom % D), deuterium oxide (99.9 atom % D); dimethyl sulfoxide-d_6 (DMSO-d_6, 99.9 atom % D, contains 0.03 % (v/v) TMS); N,N'-dicyclohexylcarbodiimide (DCC, ≥99 %); 4-dimethylaminopyridine (DMAP, ≥99 %); diethyl ether (contains BHT as inhibitor, ≥99.8 %); 4-formylbenzoic acid (97 %); glacial acetic acid (≥99.8 %); N-Isopropylacrylamide (NIPAAm, 97%); tetrahydrofuran (THF, ≥99.9 %); THF anhydrous (≥99.9 %) were obtained from Sigma-Aldrich (Finland). Dialysis bag (Spectra/Por® 6 Dialysis bag Membrane Pre-wetted RC tubing MWCo: 50 kDa) purchased from Spectra. Polyethylene glycol (PEG, 4000 Da) was acquired from Fluka®.

Release studies: Amplex™ UltraRed reagent was purchased from Invitrogen by Thermo Fisher Scientific (Finland). Doxorubicin hydrochloride (>95.0 %) was obtained from Tokyo Chemical Industry Co. LTD (Finland). Hank's balanced salt solution (HBSS, 10×) was purchased from Life Technologies (USA). Hydrogen peroxide solution (≥35 %) 2-(N-morpholino)-ethanesulfonic acid (MES); 4-(2-hydroxyethyl)-1-piperazineethanesulfonic acid (HEPES); and peroxidase from horseradish (Type II, 150- 250 U/mg) were purchased from Sigma-Aldrich (Finland).

Cell studies: Dulbecco's modified Eagle medium (DMEM) was obtained from Hyclone (Finland). Alamar Blue® was purchased from Thermo Fischer Scientific (Finland). 24-well plate (Transwell®) with 12 inserts with 6.5 mm diameter and 8.0 μm pore size and 96-well plate were acquired from Corning (Finland). CellTiterGlo® Luminescent Cell Viability assay kit was obtained from Promega Corporation (USA). Hank's balanced salt solution (HBSS, 10×), and heat-inactivated fetal bovine serum (FBS) were purchased from Life Technologies (USA). FBS, non-essential amino acids (NEAA, 100×), trypsin (2.5%), ʟ-glutamine (100×), streptomycin (100 IU/mL), penicillin (100 IU mL^{-1}), and ethylenediaminetetraacetic acid (EDTA) were acquired from HyClone (USA). 4-(2-hydroxyethyl)-1-piperazineethanesulfonic acid (HEPES) was purchased from Sigma-Aldrich (Finland).

5.2. Preparation and Characterisation of Starting Materials

In this section, the preparation and characterisation of the initial materials posteriorly used to prepare the hydrogels, namely {Mo_{154}}, CS-g-PNIPAAm and DF-PEG, are presented.

5.2.1. {Mo_{154}}

{Mo_{154}} was synthesised following the method previously described.[163] Shortly, $Na_2S_2O_4$ (0.2 g, 1.15 mmol) was added to 10 mL of an aqueous solution of $Na_2MoO_4{\bullet}2H_2O$ (3.0 g, 12.4 mmol). Next, under continuous stirring, 30 mL of HCl (1 M) was added. The solution was allowed to stir for 10 min in an open Erlenmeyer flask. After that, the solution was stored in a closed flask for three days. Then, the precipitated blue crystals were removed by filtration and washed with cold water.

The prepared POM was characterised by Raman spectroscopy using a Raman-FT Bruker RFS/100S (λ_e=1064 nm). Raman shift (cm^{-1}) = 793, 534, 463, 323, 211. {Mo_{154}} was also characterised by Fourier-transform infrared spectroscopy (FTIR) using an infrared spectrophotometer-FT Mattson 7000 galaxy series (128 scans and resolution of 4 cm^{-1}). The KBr pellets for analysis were freshly prepared. IR (KBr): ν (cm^{-1}) = 1616, 970, 912, 750, 630, 555. Moreover, {Mo_{154}} was characterised by ultraviolet-visible (UV-Vis) spectroscopy using a Thermo Scientific Evolution 220 UV-visible spectrophotometer between 400 to 1100 nm, with 100 scans/min and a bandwidth of 2 nm.

5.2.2. Chitosan Grafted with Poly(N-isopropylacrylamide)

The copolymer of CS-g-PNIPAAm was prepared by free radical polymerisation adapting the method previously reported by Duan *et al.*[165]. The copolymerisation reaction was carried out in round bottom flask equipped with a magnetic stirrer and capped with a septum, under nitrogen atmosphere. After dissolving 1.0 g of CS in 200 mL of acetic acid (0.6% (v/v)), the chitosan solution was heated to 80 ºC under nitrogen. Then, 3 mL of APS aqueous solution (1×10^{-2} M) was added to the CS solution and stirred for 10 min. Finally, 6 mL of NIPAAm aqueous solution (2.9 M) was added, and the solution stirred for 3 h at 80 ºC. The obtained product was dialysed against Milli-Q water for five days and finally freeze-dried. It was obtained a mass of 0.97 g with a yield of 65%.

CS-g-PNIPAAm was dissolved in 1 wt-% deuterium chloride solution for characterisation by ^1H Nuclear Magnetic Resonance (NMR) using an Avance III 400 MHz NMR spectrometer (Bruker). ^1H NMR (δ): 3.56-4.10 (4H, H3 to H6 from glucosamine unit, see Figure 20), 3.14 (1H, H2 from glucosamine unit, see Figure 20), 3.90 (1H, $-NH-C\underline{H}<$), 1.96 (1H, $-C\underline{H}-CH_2-$),

1.53 (2H, -CH-C$\underline{H_2}$-), 1.10 (6H, -CH-(C$\underline{H_3}$)$_2$). The ratio between the number of glucosamine (Gcs) units from CS and NIPAAm monomers from PNIPAAm was determined using the following formula:

$$\frac{Gcs\ units}{NIPAAm\ units} = \frac{\int peak(1.10\ ppm)}{\int peak(3.14\ ppm)/6}$$

Moreover, the percentage of NIPAAm monomers and glucosamine units in the final graft copolymers was determined. Initially, the molecular weight of the obtained copolymer was determined:

$$MW_{CS-g-PNIPAAm} = \frac{(\int peak\ (1.10\ ppm))}{6} \times MW_{NIPAAm} + \left(\int peak\ (3.14\ ppm)\right) \times MW_{Gcs}$$

Next, the percentage of each component was determined using the following equations:

$$NIPAAm\,\% = \frac{\left(\int peak\ (1.10\ ppm)\right) \times MW_{NIPAAm}}{MW_{CS-g-PNIPAAm}}$$

$$Gcs\,\% = \frac{\left(\int peak\ (3.14\ ppm)\right) \times MW_{Gcs}}{MW_{CS-g-PNIPAAm}}$$

The obtained copolymer was also characterised by Fourier-transform infrared spectroscopy (FTIR) – attenuated total reflectance (ATR) using an FTIR spectrometer Bruker Vertex 70 (64 scans with a resolution of 4 cm^{-1}). IR: ν (cm^{-1}) = 1639, 1533, 1387, 1368, 1065, and 1027.

The thermo-responsiveness and the critical temperature were studied by differential scanning calorimetry (DSC) using a Mettler Toledo DSC826^{e} with a flow rate of 1 ºC/min under a nitrogen atmosphere. These properties were further studied by dynamic light scattering (DLS) using a ZetaSizer Nano series (Nano-ZS from Malvern), recording the size trend with the increase of the temperature from 20 to 40 ºC, with 5 measurements in each temperature and an equilibration time of 600 s of a 0.005 wt-% aqueous solution of CS-g-PNIPAAM.

5.2.3. Di-functionalised Poly(ethylene glycol)

PEG was functionalized with benzaldehyde groups adapting the procedure previously described by Zhang *et al.*[190]. Briefly, PEG$_{4000}$ (3.26 g, 0.81 mmol) was dissolved in 50 mL of THF, followed by the addition of 4-formylbenzoic acid (0.49 g, 3.26 mmol), DMAP (0.025 g, 0.20 mmol), and DCC (0.84 g, 4.07 mmol). The mixture was allowed to react under magnetic stirring overnight, and then the white precipitate was removed by filtration. The polymer solution was purified by precipitation in diethyl ether three times, and then the polymer was obtained as a white solid. After drying in an oven (Memmert GmbH) at 37 ºC overnight, it was obtained a mass of 2.45 g with a yield of 75%.

To characterise and verify the successful functionalisation of PEG with benzaldehyde moieties, ^{1}H NMR and FTIR-ATR were carried out. To perform ^{1}H NMR spectroscopy, the obtained polymer was dissolved in DMSO-d_6.^{1}H NMR (δ): 10.12 (2H, CHO), 8.20 – 8.12 (4H, C$\underline{H}$CCHO), 8.11- 8.02 (4H, C$\underline{H}$CHCCHO), 4.47-4.40 (4H, $COOCH_2$), 3.87 – 3.38 (364 H, $COOCH_2C\underline{H_2}$ and $OC\underline{H_2}C\underline{H_2}O$). The percentage of PEG molecules modified at both ends with benzaldehyde moieties was determined using the formula:

$$\%\,Functionalization = \frac{(\int peak\ (10.12\,ppm)/2)}{(\int peak\ (3.87 - 3.38\,ppm)/364)} \times 100$$

The di-functionalized PEG was also characterised by FTIR-ATR. IR: ν (cm^{-1}) = 2886, 1712, 1464, 1341, 1280, 1095.

5.3. Hydrogel Preparation and Characterisation

A 2 wt-% CS-g-PNIPAAm solution was obtained by dissolving the polymer in an acetic acid aqueous solution 0.01% (v/v). A 33 wt-% of DF-PEG solution was prepared by dissolving 500 mg of the polymer in 1 mL of Milli-Q water. A solution containing 1.1 wt-% of $\{Mo_{154}\}$ and 44 wt-% PEG was prepared by dissolving 20 mg of POM and 800 mg of PEG in 1 mL of Milli-Q water. Furthermore, for the blank hydrogels, a 44 wt-% solution of PEG was prepared by dissolving 800 mg of PEG in 1 mL of Milli-Q water.

The hydrogel was prepared by simply mixing all the components, as illustrated in Figure 49. Briefly, the $\{Mo_{154}\}$+PEG solution (25 μL) was added to the DF-PEG solution (50 μL), and then a CS-g-PNIPAAm solution (225 μL) was added to the mixture. Finally, all the components were mixed for 30 sec using a vortex, and within less than 1 min, the hydrogel was formed.

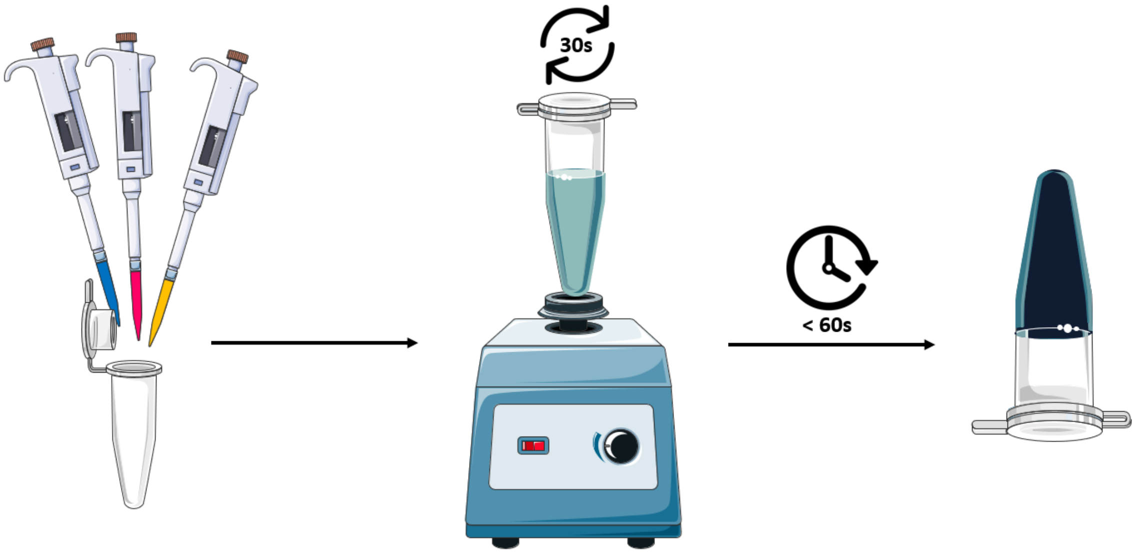

Figure 49 – Scheme of hydrogel preparation. Initially, the three main components are added together, then, mixed using a vortex for 30 sec and within less than 60 sec, the hydrogel is formed.

The blank hydrogels were prepared in the same way, but instead of adding {Mo_{154}}+PEG solution, a PEG aqueous solution was added.

The hydrogels were characterised by vibrational spectroscopy FTIR-ATR and Raman, and UV-Vis spectroscopy. For FTIR-ATR and Raman spectroscopy the hydrogel was previously prepared, frozen for 1 h in a –20 ºC freezer and freeze-dried for 4 days. The FTIR spectrum was recorded from 3500 to 675 cm^{-1}. IR: ν (cm^{-1}) = 1712, 1639, 1533, 1280, 1095.

Raman spectroscopy was recorded from 1750 to 100 cm^{-1} using a spectrophotometer Raman-FT Bruker RFS/100S. Raman shift (cm^{-1}) = 1643, 1609, 1500 to 1427, 1319 to 1215, 1170 to 1096, 534, 463, 211.

The UV-Vis absorption spectra of a {Mo_{154}} aqueous solution and both hydrogels with and without {Mo_{154}} were recorded using a Varioskan™ LUX multimode microplate reader (Thermo Fisher Scientific) between 400 to 1000 nm.

Scanning electron microscopy (SEM) images, were acquired in a FEG-SEM Hitachi SU-70 operated at 15 kV with energy-dispersive X-ray spectroscopy (EDS) Bruker QUANTAX 400 detector. The hydrogel samples were prepared by freeze-drying, as described above, and placed in an aluminium support with double-sided carbon tape, and deposition of a carbon coating was performed before SEM analysis.

The thermo-responsiveness was evaluated by DSC analysis of the freshly prepared hydrogel under N_2 atmosphere. For that, the hydrogel was prepared and poured into the DSC pan before gelation. To study the deviation of the critical temperature, CS-g-PNIPAAm solutions with different polymer concentrations (0.5, 1.5 and 2 wt-%) were prepared. In addition, an aqueous solution containing PEG and CS-g-PNIPAAm with the same final polymer concentration (14 wt-%) as the one in the hydrogel was prepared by mixing 0.225 mL of CS-g-PNIPAAm (2 wt-%), 0.025 mL of PEG (44 wt-%) and 0.05 mL of PEG (33 wt-%).

The rheological behaviour of both hydrogel and hydrogel control were accessed by oscillatory shear rheometry using a TA Instruments AR2000 rheometer with a 20 mm diameter stainless steel plate-and-plate (parallel plate) geometry, as illustrated in Figure 50. Three different test methods were employed: oscillatory time sweep, strain sweep, and frequency sweep. The time sweep test was done to monitor the *in-situ* gelation of the hydrogel solutions and was performed by recording the temporal evolution of the storage modulus, G', and the loss modulus, G''. All the components of the hydrogel were added to the down plate, and the test was initiated right after. The strain was kept at 1% and with an angular frequency of 1 Hz, at 25 ºC, for 10 min.

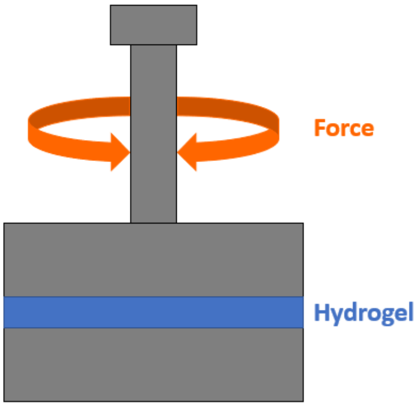

Figure 50 – Schematic illustration of the oscillatory shear rheometry set-up.

The strain sweep test was carried out on hydrogels to determine and compare their G' and G'' under the same physical conditions and to find the linear viscoelastic region (LVR). In the LVR, both G' and G'' exhibit constant plateau values. The term "LVR" is derived from the existing proportionality between the predefined and measured parameters.[215] The LVR is an important parameter because it dictates the range in which a test can be performed without destroying the structure of the sample. This is important information to set the strain at which the frequency sweep and the step strain measurements are carried out. The strain sweep test was performed at 25 ºC for the hydrogel and hydrogel control, and at 37 ºC only for the hydrogel. G' and G'' were recorded while the strain was increased from 0.9% to 1000% at a constant frequency of 1 Hz. The hydrogels were also subjected to a frequency sweep at a constant strain (1%) and temperature (25 and 37 ºC). The G' and G'' values were recorded with the increase of the oscillatory frequency from 0.016 to 3.82 Hz.

Furthermore, to study the self-healing behaviour of the prepared formulation, step strain measurements were also performed. The amplitude oscillatory forces were changed from 1 to 1000%, keeping the angular frequency (1 Hz) and the temperature (25 ºC) constant.

To further study the self-healing of the prepared material, a freshly prepared hydrogel was placed in a glass coverslip and a hole with approximately 0.5 cm in diameter was made in the centre of the hydrogel. The closure of the hole was recorded, and the time passed until the complete recovery of the hydrogel counted.

The injectability of the developed hydrogel was studied by extrusion of the hydrogel through a needle (Terumo® AGANI 27G×5/8, 0.4×16mm). Initially, the hydrogel was loaded into a 10 mL syringe (Soft-Ject®, from Henke Sass Wolf, Germany) before gelation, and after 5 min extruded through a needle into 2 mL of HBSS-HEPES. The same procedure was repeated with gelatin. The gelatin was prepared using a 7.5 wt-% gelatin solution with 6 mg of $\{Mo_{154}\}$. The gelatin solution was previously heated to 37 ºC and then loaded in the syringe and cooled down until gelation in the fridge.

5.4. *In vitro* Release Studies

To prove the suitability of the developed hydrogel for the delivery of distinct cargo molecules, such as a small drug molecule and a protein, the release of doxorubicin (DOX) and horseradish peroxidase (HRP) were studied.

DOX has an orange colouration (Figure 51) and consequently exhibits an absorption band around 480 nm. Moreover, DOX is also known to show strong fluorescence. Therefore, both the absorption and fluorescence can be used in the detection of this drug.

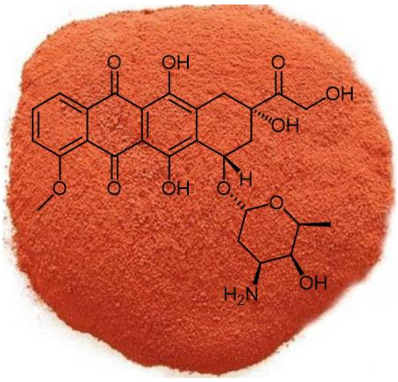

Figure 51 – DOX structure overlaid in a photograph of its powder.

Before performing the release, it was necessary to do an absorption spectrum of the compound in each of the two buffers used (HBSS-HEPES, pH 7.4 and HBSS-MES, pH 5.5), as well as the respective calibration curves. The calibration curves were prepared by dilution of a DOX solution (10 μg/mL) to obtain concentrations between 0.01 and 1 μg/mL and a distinct solution (1 mg/mL) to prepare concentrations between 2 and 10 μg/mL. The dilutions were prepared in the respective buffer (HBSS-HEPES, pH 7.4 or HBSS-MES, pH 5.5). Then, a microplate reader was used to read the absorbance (λ = 480 nm) and the fluorescence (λ_{ex} = 470 nm; λ_{em} = 585 nm) of the prepared patterns.

Once defined the detection method and limits for DOX, it was proceeded to the release study. To do that, the hydrogels were prepared as previously described with the further addition of 25 μL of DOX aqueous solution (1 mg/mL). After the gelation of the hydrogels, 1.5 mL of the selected buffer (HBSS-HEPES, pH 7.4 or HBSS-MES, pH 5.5) was added. In each time point, 10 μL of the release medium was removed and substituted by the same volume of fresh buffer. The aliquots removed were diluted 10×, centrifuged (5 min, 9000 rpm), and 80 μL was removed from the supernatant to a plate posteriorly analysed by fluorescence. The release experiments were performed at RT and 37 ºC in an oven (Memmert). For each condition, the analysis was done in triplicate. A control for release study incorporating the same amount of DOX in 1.5 mL of release buffer was also incubated at RT and 37 ºC. Aliquots were taken at the same time points to monitor the fluorescence/absorbance variation of DOX itself during the release study.

To prove the ability of the prepared hydrogel to load and release a protein cargo, HRP was used as a model payload. However, HRP cannot be directly quantified. Thus, to quantify the amount of enzyme released, it was necessary to use a substrate (Amplex^{TM} UltraRed) that is converted in a fluorescent product in the presence of HRP and H_2O_2. The structure of Amplex^{TM} UltraRed is not known, reason why in Figure 52 is displayed the conversion mechanism of Amplex^{TM} Red in resofurin (fluorescent), which exhibits the same basic principle.

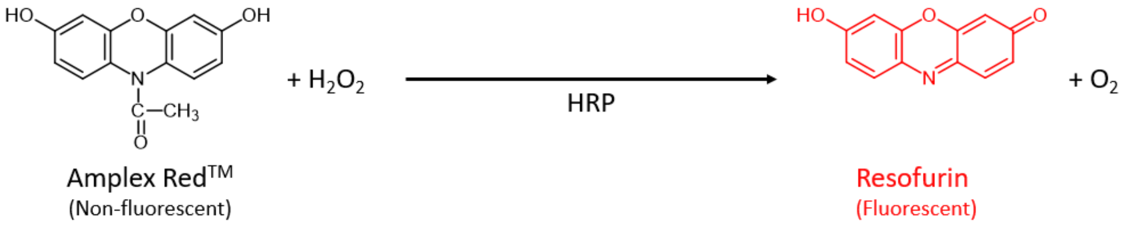

Figure 52 – Conversion of Amplex^{TM} Red in resofurin a fluorescent compound, by HRP.

To relate the fluorescence signal obtained with the concentration of HRP present in the sample, it was necessary to look at enzymatic kinetics. If we define, *dP* as the variation of the reaction product formation, and *dt* as the time variation, the initial reaction rate, v_0, is defined as:

$$v0 = \frac{dP}{dt}$$

Then, v_0 can be determined for each sample using the first points of the curves of luminescence intensity against time. Thus, by making a linear fit to those points, v_0 corresponds to the slope of the obtained curves.

v_0 can also be defined by the Michaelis-Menten equation:

$$v0 = \frac{Vmax[S]}{K_M + [S]}$$

where, V_{max} corresponds to maximum reaction rate with the concentration of substrate, $[S]$ denotes the substrate concentration, and K_M is the Michaelis constant. By definition,

$$Vmax = Kcat[E]$$

where, K_{cat} is a constant (turnover number) and $[E]$ the enzyme concentration. Substituting this on Michaelis-Menten equation and assuming that $[S] >> K_M$, we can relate v_0 and $[E]$, as follows:

$$v0 = K[E]$$

Thus, using this equation, one can associate v_0 with the concentration of the enzyme present in each sample, allowing the quantification of HRP.

The patterns for the calibration curve were prepared in HBSS-HEPES (pH 7.4) and HBSS-MES (pH 5.5) by dilution of a HRP solution with a concentration of 10 ng/mL for the concentrations between 0.5 and 7.5 ng/mL and HRP solution with a concentration of 100 ng/mL for the concentrations between 10 and 15 ng/mL.

The HRP release was carried out as above described. Briefly, 10 μL of HRP aqueous solution (1 mg/mL) was added to the hydrogel. After gelation, 1.5 mL of the appropriate buffer (HBSS-HEPES, pH 7.4 or HBSS-MES, pH 5.5) was added. Then, in each time point, 5 μL of the release medium was removed and substituted by the same volume of fresh buffer. The aliquots removed were diluted 301×. The release experiments were performed at RT and 37 ºC in an oven. For each condition, the analysis was done in triplicate. To determine the concentration of HRP being released at each time point, control samples were also performed. Control samples were prepared by incorporating the same amount of HRP in 1.5 mL of release buffer and by incubating it at RT and 37 ºC. Aliquots were taken at the same time points to monitor the fluorescence variation of HRP itself during the release study.

Finally, 50 μL of each sample or pattern was placed in a 96-well plate, and 50 μL of Amplex^{TM} UltraRed stock solution was added right before the reading. The fluorescence was measured using a Varioskan^{TM} Lux with a λ_{ex} = 565 nm and a λ_{em} = 590 nm, in intervals of 30 sec.

The percentage of release (% Release) in each time point was determined based on v_0 (the slope of the curves obtained with the points from the two first min after the addition of the substrate). This value was substituted in the calibration curve, and then a correction based on the background (value obtained in t = 0 min) and on the control samples was applied.

5.5. Cytotoxicity Studies

The cytotoxicity of the initial components of the hydrogel was evaluated using a fluorescent metabolic assay. The metabolic assays evaluate the cellular metabolic activity, indicating the ability of a cell to modify a substrate, usually colourless or with a specific colour, and convert it in a coloured product, different from the initial substrate. A metabolic assay widely used is the resazurin assay (Alamar Blue®), in which the substrate is resazurin. Resazurin is a redox indicator exhibiting cell-permeability, solubility in physiological buffers, a deep-blue colour and that is non-fluorescent and non-toxic. These features allow its direct use in cell culture.[216] Therefore, the metabolic active, or "live", cells will secrete enzymes, namely NADH dehydrogenase and carnitine dehydrogenase, which reduces resazurin into resorufin, with concomitant oxidation of the electron source, NADH to NAD^+ (Figure 53). The amount of resorufin produced is proportional to the number of viable cells. Since the reaction product, resorufin, fluoresces when excited with 560 nm light, and presents a red/pink colouration, the cell viability can be assed either by absorbance or fluorescence.[217]

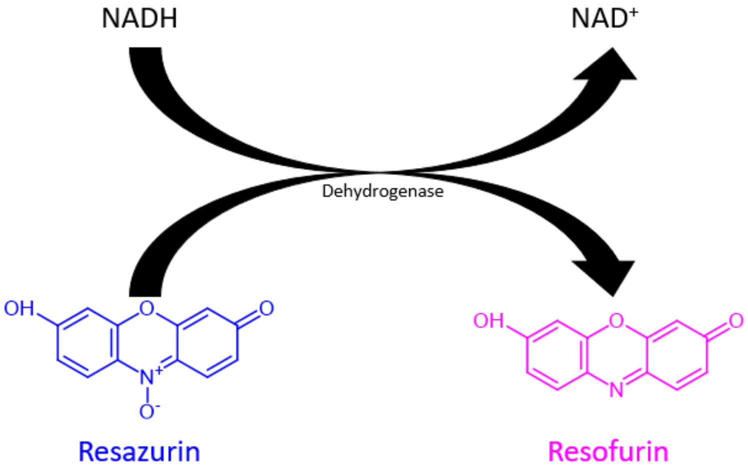

Figure 53 – Scheme of the mechanism of conversion of resazurin (blue-coloured and non-fluorescent) in resorufin (pink-coloured and fluorescent) in viable cells.

Briefly, human melanoma cells (M21, used from passage 5 to 12) were seeded in 96-well plates at the density of 1.5 × 10^4 cells per well and allowed to attach overnight. After cell adhesion, the wells were washed with HBSS-HEPES buffer (pH 7.4) and finally incubated with 100 μL of solutions of CS-g-PNIPAAm (0.0, 0.01, 0.05, 0.1, 0.5, and 1.0 mg/mL), DF-PEG (0.0, 0.1, 0.5, 1.0, 5.0, 10.0 and mg/mL), and {Mo_{154}} (0.0, 0.1, 0.2, 0.4, 0.8, and 1.7 mg/mL). In all experiments, several wells with Triton X-100 (1%) as the positive control were included. After 4 and 24 h of incubation, the wells were washed with HBSS-HEPES buffer (pH 7.4) and then, 10 μL of Alamar Blue® and 90 μL of HBSS-HEPES buffer (pH 7.4) were added. Each experiment was performed at least in triplicates. The respective plates were incubated at 37 ºC. After 6 h, the fluorescence was measured using a plate reader exciting the samples with a λ_{ex} = 560 nm and measuring the emission intensity at 590 nm.

The biocompatibility of the hydrogels was evaluated through an ATP (adenosine triphosphate) based luminescent cell viability assay. ATP is the most relevant chemical energy reservoir in cells and is core in several cellular processes such as signalling, biological synthesis, movement, and transport. However, when the cells are damaged lethally, they lose the ability to produce ATP, leading to a dramatic decrease in the ATP cellular level. The ATP assays are based on the conversion of luciferin in oxyluciferin catalysed by the enzyme luciferase in the presence of Mg^{2+} and ATP, originating a luminescent signal (Figure 54). Since the luminescent signal is proportional to the ATP concentration, which is equivalent to the number of viable cells in each sample, it is possible to determine the amount of viable cells.[218]

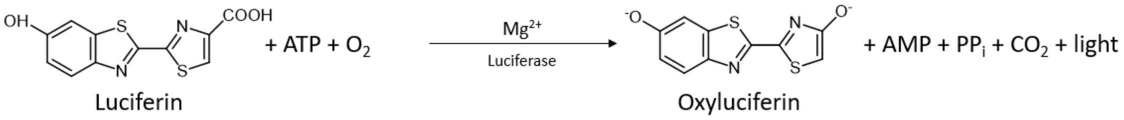

Figure 54 – Generation of the luminescent signal by catalysation of the conversion of luciferin to oxyluciferin.

In this case, M21 cells were seeded in 24-well plate (Transwell®) at the density of 5 × 10^4 cells per well and allowed to attach overnight. Then, the old medium was substituted by 1 mL of fresh medium and the freshly prepared hydrogels with and without {Mo_{154}} were added to the inserts before gelation (Figure 55).

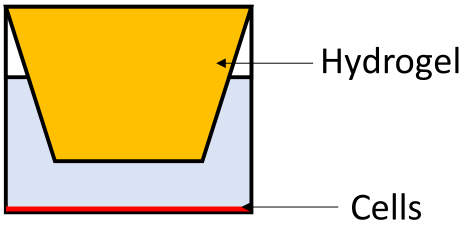

Figure 55 – Schematic illustration of the cell setup in the in 24-well plate (Transwell®).

After 4 and 24 h, the inserts were removed, and the CellTiterGlo® luminescent assay was performed as indicated in the fabricant protocol. Briefly, 250 μL of CellTiterGlo® reagent was added to 250 μL of HBSS-HEPES buffer (pH 7.4). To induce cell lysis, the plate was shaken for 2 min in an orbital shaker. Then, to stabilise the luminescent signal, the plate was incubated for 10 min at RT. Finally, 100 μL aliquots from each well were transferred to a 96-well plate and the luminescence recorded using a Varioskan™ LUX multimode microplate reader.

In all biocompatibility assays, the percentage of viable cells was calculated accordingly to the following equation:

$$Viability\ (\%) = \frac{Signal\ Sample}{Signal\ Control} \times 100$$

The statistical significance was analysed with one-way analysis of variance (ANOVA), with the level of significance set at probabilities of $*p < 0.05$. All statistical analyses were carried out using the software Origin 2018 (OriginLab, US).

5.6. Photothermal Conversion Studies

The photothermal conversion of the prepared hydrogel was studied by light irradiation in a 96-well plate with a laser from a Raman RXN1-PhAT-785 nm-D (A Kaiser aerospace & electronics company) with an irradiance of 0.1 W/cm^2 placed on the top of the plate, as shown in Figure 56. The temperature variation was measured in intervals of 30 sec using a thermocouple. To study the increase of the temperature variation of with the concentration of photothermal agent {Mo_{154}}, hydrogels with different POM concentrations were prepared by changing the initial concentration of the {Mo_{154}} + PEG solution. The concentrations used in this study were 0, 5, 10, 20, and 40 mg/mL, and the final concentrations of 0, 0.7, 1.4, 2.7, 5.4 wt-%.

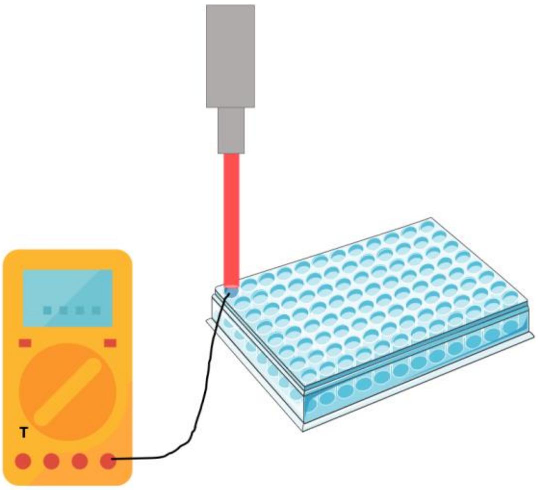

Figure 56 – Schematic illustration of the photothermal conversion measurements.

An additional experiment was performed to study the temperature increase in the cell setup used for hydrogels, *i.e.*, the ability of the system to reach a temperature able to ablate the cancer cells. For that, 300 μL of hydrogel was placed in the inserts of a 24 well-plate with Transwell® that afterwards was filled with 1 mL of HBSS-HEPES. Then, the hydrogel was irradiated for 10 min using a laser (785 nm) with an irradiance of 0.1 W/cm^2 placed on the top of the plate. The temperature was measured in intervals of 30 sec using a thermocouple. To further study the photothermal conversion, the increase of the temperature variation with the variation of the irradiance was also studied. To do that, a laser Rothinker (808 nm) was adjusted with different current outputs (1.51, 1.56, 1.58, 1.63, and 1.66 A) and the temperature was measured by a thermocouple. The experiment was carried out in a black box, in dark conditions. The formulation and the hydrogel control (blank) used in this assay were the ones previously described. The power values used were subsequently determined using a calibration line provided by the laser manufacturer, and the irradiance values were calculated by dividing the power values by the irradiated area.

6. Bibliography

(1) Wu, L. Organically Encapsulated Polyoxometalate Catalysts. In *Encapsulated Catalysts*; Sadjadi, S., Ed.; Elsevier: Oxford, 2017; pp 1–33. https://doi.org/10.1016/B978-0-12-803836-9.00001-8.

(2) Miras, H. N.; Long, D. L.; Cronin, L. Exploring Self-Assembly and the Self-Organization of Nanoscale Inorganic Polyoxometalate Clusters. In *Advances in Inorganic Chemistry*; Elsevier Inc., 2017; Vol. 69, pp 1–28. https://doi.org/10.1016/bs.adioch.2016.12.001.

(3) Hasenknopf, B. Polyoxometalates: Introduction to a Class of Inorganic Compounds and Their Biomedical Applications. *Front. Biosci.* **2005**, *10*, 275–287.

(4) Hutin, M.; Rosnes, M. H.; Long, D.-L.; Cronin, L. Polyoxometalates: Synthesis and Structure – From Building Blocks to Emergent Materials. In *Comprehensive Inorganic Chemistry II*; Reedijk, J., Poeppelmeier, K., Eds.; Elsevier, 2013; Vol. 2, pp 241–269. https://doi.org/10.1016/B978-0-08-097774-4.00210-2.

(5) Pope, M. T.; Müller, A. Polyoxometalate Chemistry: An Old Field with New Dimensions in Several Disciplines. *Angew. Chemie - Int. Ed.* **1991**, *30* (1), 34–48. https://doi.org/10.1002/anie.199100341.

(6) Moiras, C.; Cronin, L. Polyoxometalate Nanocapsules: From Structure to Function. In *Organic Nanostructures*; Atwood, J. L., Steed, J. W., Eds.; Wiley-VCH Verlag GmbH & Co. KGaA: Weinheim, 2008; pp 275–289. https://doi.org/10.1002/9783527622504.ch11.

(7) Kortz, U.; Müller, A.; van Slageren, J.; Schnack, J.; Dalal, N. S.; Dressel, M. Polyoxometalates: Fascinating Structures, Unique Magnetic Properties. *Coord. Chem. Rev.* **2009**, *253* (19–20), 2315–2327. https://doi.org/10.1016/j.ccr.2009.01.014.

(8) Rhule, J. T.; Hill, C. L.; Judd, D. A.; Schinazi, R. F. Polyoxometalates in Medicine. *Chem. Rev.* **1998**, *98* (1), 327–358. https://doi.org/10.1021/cr960396q.

(9) Long, D.-L.; Tsunashima, R.; Cronin, L. Polyoxometalates: Building Blocks for Functional Nanoscale Systems. *Angew. Chemie - Int. Ed.* **2010**, *49* (10), 1736–1758. https://doi.org/10.1002/anie.200902483.

(10) Müller, A.; Krickemeyer, E.; Meyer, J.; Bögge, H.; Peters, F.; Plass, W.; Diemann, E.; Dillinger, S.; Nonnenbruch, F.; Randerath, M.; et al. [Mo154(NO)14O420(OH)28(H2O)70](25 ± 5)−: A Water-Soluble Big Wheel with More than 700 Atoms and a Relative Molecular Mass of About 24000. *Angew. Chemie - Int. Ed.* **1995**, *34* (19), 2122–2124. https://doi.org/10.1002/anie.199521221.

(11) Nicoara, A.; Patrut, A.; Margineanu, D.; Müller, A. Electrochemical Investigation of

Molecular Growth of the {Mo57V6} Polyoxometalate Cluster. *Electrochem. Commun.* **2003**, *5* (6), 511–518. https://doi.org/10.1016/S1388-2481(03)00114-0.

(12) Müller, A.; Kögerler, P.; Kuhlmann, C. A Variety of Combinatorially Linkable Units as Disposition: From a Giant Icosahedral Keplerate to Multi-Functional Metal–Oxide Based Network Structures. *Chem. Commun.* **1999**, No. 15, 1347–1358. https://doi.org/10.1039/a901436e.

(13) Akutagawa, T.; Jin, R.; Tunashima, R.; Noro, S.; Cronin, L.; Nakamura, T. Nanoscale Assemblies of Gigantic Molecular {Mo154 }-Rings: (Dimethyldioctadecylammonium)20 [Mo154O462H8(H2O)70]. *Langmuir* **2008**, *24* (1), 231–238. https://doi.org/10.1021/la701364k.

(14) Müller, A.; Plass, W.; Krickemeyer, E.; Dillinger, S.; Bögge, H.; Armatage, A.; Proust, A.; Beugholt, C.; Bergmann, U. [Mo57Fe6(NO)6O174(OH)3(H2O)24]15-: A Highly Symmetrical Giant Cluster with an Unusual Cavity and the Possibility of Positioning Paramagnetic Centers on Extremely Large Cluster Surfaces. *Angew. Chemie - Int. Ed.* **1994**, *33* (8), 849–851. https://doi.org/10.1002/anie.199408491.

(15) Müller, A.; Das, S. K.; Fedin, V. P.; Krickemeyer, E.; Beugholt, C.; Bögge, H.; Schmidtmann, M.; Hauptfleisch, B. Rapid and Simple Isolation of the Crystalline Molybdenum-Blue Compounds with Discrete and Linked Nanosized Ring-Shaped Anions: Na15[Mo126(VI)Mo28(V)O462H14(H2O)70]0.5 [Mo124(VI)Mo28(V)O457H14(H2O)68]0.5 · ca. 400 H2O and Na22[Mo118(VI)Mo28(V)O442H14(H2O)5. *J. Inorg. Gen. Chem.* **1999**, *625* (7), 1187–1192. https://doi.org/10.1002/(SICI)1521-3749(199907)625:7<1187::AID-ZAAC1187>3.0.CO;2-%23.

(16) Müller, A.; Sousa, F. L.; Merca, A.; Bögge, H.; Miró, P.; Fernández, J. A.; Poblet, J. M.; Bo, C. Supramolecular Chemistry on a Cluster Surface: Fixation/Complexation of Potassium and Ammonium Ions with Crown-Ether-like Rings. *Angew. Chemie - Int. Ed.* **2009**, *48* (32), 5934–5937. https://doi.org/10.1002/anie.200902137.

(17) Müller, A.; Plass, W. Spectroscopic Investigations of the Unusual Giant Cluster Anion [Mo57Fe6(NO)6O174(OH)3(H2O)24]15 Containing 276 Non-Hydrogen Atoms. *J. Mol. Struct.* **1994**, *321* (3), 215–223. https://doi.org/10.1016/0022-2860(93)07983-4.

(18) Muller, A.; Plass, W.; Krickemeyer, E.; Sessoli, R.; Gatteschi, D.; Meyer, J.; Bogge, H.; Krockel, M.; Trautwein, A. X. Stepwise Substituting Magnetic Centers in a Giant Cluster Host System. *Inorg. Chim. Acta* **1998**, *271* (1,2), 9–12. https://doi.org/10.1016/S0020-1693(97)05885-4.

(19) Müller, A.; Krickemeyer, E.; Dillinger, S.; Bögge, H.; Plass, W.; Proust, A.; Dloczik,

L.; Menke, C.; Meyer, J.; Rohlfing, R. New Perspectives in Polyoxometalate Chemistry by Isolation of Compounds Containing Very Large Moieties as Transferable Building Blocks:(NMe4) 5 [As2Mo8V4AsO40]· 3H2O,(NH4) 21 [H3Mo57V6 (NO) 6O183 (H2O) 18]· 65 H2O,(NH2Me2) 18 (NH4) 6 [Mo57V6 (NO) 6O183 (H. *J. Inorg. Gen. Chem.* **1994**, *620*, 599–619. https://doi.org/10.1002/zaac.19946200405.

(20) Müller, A.; Serain, C. Soluble Molybdenum Blues - “Des Pudels Kern.” *Acc. Chem. Res.* **2000**, *33* (1), 2–10. https://doi.org/10.1021/ar9601510.

(21) Müller, A.; Gouzerh, P. From Linking of Metal-Oxide Building Blocks in a Dynamic Library to Giant Clusters with Unique Properties and towards Adaptive Chemistry. *Chem. Soc. Rev.* **2012**, *41* (22), 7431–7463. https://doi.org/10.1039/c2cs35169b.

(22) Mukherjee, H. Treatment of Cancer of the Intestinal Tract With a Complex Compound of Phosphotungtic Phosphomolybdic Acids and Caffeine. *J. Indian Med. Assoc.* **1965**, *44*, 477–479.

(23) Jasmin, C.; Chermann, J.-C.; Herve, G.; Teze, A.; Souchay, P.; Boy-Loustau, C.; Raybaud, N.; Sinoussi, F.; Raynaud, M. In Vivo Inhibition of Murine Leukemia and Sarcoma Viruses by the Heteropolyanion 5-Tungsto-2-Antimoniate2. *JNCI J. Natl. Cancer Inst.* **1974**, *53* (2), 469–474. https://doi.org/10.1093/jnci/53.2.469.

(24) Bijelic, A.; Aureliano, M.; Rompel, A. Polyoxometalates as Potential Next-Generation Metallodrugs in the Combat Against Cancer. *Angew. Chemie - Int. Ed.* **2018**, *57*, 2–22. https://doi.org/10.1002/anie.201803868.

(25) Rozenbaum, W.; Dormont, D.; Spire, B.; Vilmer, E.; Gentilini, M.; Griscelli, C.; Montagnier, L.; Barre-Sinoussi, F.; Chermann, J. . Antimoniotungstate (HPA 23) Treatment of Three Patients with AIDS and One with Prodrome. *Lancet* **1985**, *325* (8426), 450–451. https://doi.org/10.1016/S0140-6736(85)91162-6.

(26) Witvrouw, M.; Weigold, H.; Pannecouque, C.; Schols, D.; De Clercq, E.; Holan, G. Potent Anti-HIV (Type 1 and Type 2) Activity of Polyoxometalates: Structure−Activity Relationship and Mechanism of Action. *J. Med. Chem.* **2000**, *43* (5), 778–783. https://doi.org/10.1021/jm980263s.

(27) Judd, D. A.; Nettles, J. H.; Nevins, N.; Snyder, J. P.; Liotta, D. C.; Tang, J.; Ermolieff, J.; Schinazi, R. F.; Hill, C. L. Polyoxometalate HIV-1 Protease Inhibitors. A New Mode of Protease Inhibition. *J. Am. Chem. Soc.* **2001**, *123* (5), 886–897. https://doi.org/10.1021/ja001809e.

(28) Flütsch, A.; Schroeder, T.; Grütter, M. G.; Patzke, G. R. HIV-1 Protease Inhibition Potential of Functionalized Polyoxometalates. *Bioorg. Med. Chem. Lett.* **2011**, *21* (4),

1162–1166. https://doi.org/10.1016/j.bmcl.2010.12.103.

(29) Tajima, Y. Purification of a Factor That Enhances the Antibacterial Activity of β-Lactams against Methicillin-Resistant Staphylococcus Aureus: Its Identification as Undecaphosphotungstate. *J. Inorg. Biochem.* **1997**, *68* (2), 93–99. https://doi.org/10.1016/S0162-0134(97)00049-4.

(30) Tajima, Y. Effects of Tungstosilicate on Strains of Methicillin-Resistant Staphylococcus Aureus with Unique Resistant Mechanisms. *Microbiol. Immunol.* **2003**, *47* (3), 207–212. https://doi.org/10.1111/j.1348-0421.2003.tb03388.x.

(31) Fukuda, N.; Yamase, T.; Tajima, Y. Inhibitory Effect of Polyoxotungstates on the Production of Penicillin-Binding Proteins and β-Lactamase against Methicillin-Resistant Staphylococcus Aureus. *Biol. Pharm. Bull.* **1999**, *22* (5), 463–470. https://doi.org/10.1248/bpb.22.463.

(32) Gu, J.; Zhang, L.; Yuan, X.; Chen, Y.; Gao, X.; Li, D. Synthesis and Antibacterial Activity of Polyoxometalates with Different Structures. *Bioinorg. Chem. Appl.* **2018**, *2018*, 1–6. https://doi.org/10.1155/2018/9342326.

(33) Heyliger, C. E.; Tahiliani, A. G.; McNeill, J. H. Effect of Vanadate on Elevated Blood Glucose and Depressed Cardiac Performance of Diabetic Rats. *Science* **1985**, *227* (4693), 1474–1477. https://doi.org/10.1126/science.3156405.

(34) Meyerovitch, J.; Farfel, Z.; Sack, J.; Shechter, Y. Oral Administration of Vanadate Normalizes Blood Glucose Levels in Streptozotocin-Treated Rats. *J. Biol. Chem.* **1987**, *262* (14), 6658–6662.

(35) Gao, N.; Sun, H.; Dong, K.; Ren, J.; Duan, T.; Xu, C.; Qu, X. Transition-Metal-Substituted Polyoxometalate Derivatives as Functional Anti-Amyloid Agents for Alzheimer's Disease. *Nat. Commun.* **2014**, *5*, 1–9. https://doi.org/10.1038/ncomms4422.

(36) Chen, Q.; Yang, L.; Zheng, C.; Zheng, W.; Zhang, J.; Zhou, Y.; Liu, J. Mo Polyoxometalate Nanoclusters Capable of Inhibiting the Aggregation of Aβ-Peptide Associated with Alzheimer's Disease. *Nanoscale* **2014**, *6* (12), 6886–6897. https://doi.org/10.1039/c3nr05906e.

(37) Geng, J.; Li, M.; Ren, J.; Wang, E.; Qu, X. Polyoxometalates as Inhibitors of the Aggregation of Amyloid β Peptides Associated with Alzheimer's Disease. *Angew. Chemie - Int. Ed.* **2011**, *50* (18), 4184–4188. https://doi.org/10.1002/anie.201007067.

(38) Wang, X.; Li, F.; Liu, S.; Pope, M. T. New Liposome-Encapsulated-Polyoxometalates: Synthesis and Antitumoral Activity. *J. Inorg. Biochem.* **2005**, *99* (2), 452–457. https://doi.org/10.1016/j.jinorgbio.2004.10.020.

(39) Zhai, F.; Li, D.; Zhang, C.; Wang, X.; Li, R. Synthesis and Characterization of Polyoxometalates Loaded Starch Nanocomplex and Its Antitumoral Activity. *Eur. J. Med. Chem.* **2008**, *43* (9), 1911–1917. https://doi.org/10.1016/j.ejmech.2007.11.032.

(40) Geisberger, G.; Paulus, S.; Carraro, M.; Bonchio, M.; Patzke, G. R. Synthesis, Characterisation and Cytotoxicity of Polyoxometalate/ Carboxymethyl Chitosan Nanocomposites. *Chem. - Eur. J.* **2011**, *17* (16), 4619–4625. https://doi.org/10.1002/chem.201002815.

(41) Pandya, V. M.; Joshi, S. A. Fabrication of Novel Anticancer Polyoxometalate [CoW11O39(CpTi)]7- -Chitosan Nanocomposite, Its Toxicity Reduction, and Sustained Release. *Asian J. Pharm. Clin. Res.* **2017**, *10* (4), 278–282. https://doi.org/10.22159/ajpcr.2017.v10i4.16721.

(42) Guo, R.; Cheng, Y.; Ding, D.; Li, X.; Zhang, L.; Jiang, X.; Liu, B. Synthesis and Antitumoral Activity of Gelatin/Polyoxometalate Hybrid Nanoparticles. *Macromol. Biosci.* **2011**, *11* (6), 839–847. https://doi.org/10.1002/mabi.201000434.

(43) Menon, D.; Thomas, R. T.; Narayanan, S.; Maya, S.; Jayakumar, R.; Hussain, F.; Lakshmanan, V. K.; Nair, S. V. A Novel Chitosan/Polyoxometalate Nano-Complex for Anti-Cancer Applications. *Carbohydr. Polym.* **2011**, *84* (3), 887–893. https://doi.org/10.1016/j.carbpol.2010.12.030.

(44) Geisberger, G.; Gyenge, E. B.; Maake, C.; Patzke, G. R. Trimethyl and Carboxymethyl Chitosan Carriers for Bio-Active Polymer-Inorganic Nanocomposites. *Carbohydr. Polym.* **2013**, *91* (1), 58–67. https://doi.org/10.1016/j.carbpol.2012.08.009.

(45) Shah, H. S.; Joshi, S. A.; Haider, A.; Kortz, U.; Ur-Rehman, N.; Iqbal, J. Synthesis of Chitosan-Coated Polyoxometalate Nanoparticles against Cancer and Its Metastasis. *RSC Adv.* **2015**, *5* (113), 93234–93242. https://doi.org/10.1039/C5RA18489D.

(46) Pérez-Álvarez, L.; Ruiz-Rubio, L.; Artetxe, B.; Vivanco, M. d. M.; Gutiérrez-Zorrilla, J. M.; Vilas-Vilela, J. L. Chitosan Nanogels as Nanocarriers of Polyoxometalates for Breast Cancer Therapies. *Carbohydr. Polym.* **2019**, *213*, 159–167. https://doi.org/10.1016/j.carbpol.2019.02.091.

(47) Azizullah; Nisar-ur-Rehman; Liu, W.; Haider, A.; Kortz, U.; Sohail, M.; Joshi, S. A.; Iqbal, J. Novel Gelatin-Polyoxometalate Based Self-Assembled PH Responsive Hydrogels: Formulation and in Vitro Characterization. *Des. Monomers Polym.* **2016**, *19* (8), 697–705. https://doi.org/10.1080/15685551.2016.1209629.

(48) Azizullah; Nisar-ur-Rehman; Haider, A.; Kortz, U.; Afridi, S. U.; Sohail, M.; Joshi, S. A.; Iqbal, J. Novel PH Responsive Supramolecular Hydrogels of Chitosan

Hydrochloride and Polyoxometalate: In-Vitro, in-Vivo and Preliminary Safety Evaluation. *Int. J. Pharm.* **2017**, *533* (1), 125–137. https://doi.org/10.1016/j.ijpharm.2017.09.034.

(49) Cao, H.; Li, C.; Qi, W.; Meng, X.; Tian, R.; Qi, Y.; Yang, W.; Li, J. Synthesis, Cytotoxicity and Antitumour Mechanism Investigations of Polyoxometalate Doped Silica Nanospheres on Breast Cancer MCF-7 Cells. *PLoS One* **2017**, *12* (7), 1–18. https://doi.org/10.1371/journal.pone.0181018.

(50) Karimian, D.; Yadollahi, B.; Mirkhani, V. Dual Functional Hybrid-Polyoxometalate as a New Approach for Multidrug Delivery. *Microporous Mesoporous Mater.* **2017**, *247*, 23–30. https://doi.org/10.1016/j.micromeso.2017.03.048.

(51) Sun, G.; Chang, Y.; Li, S.; Li, Q.; Xu, R.; Gu, J.; Wang, E. PH-Responsive Controlled Release of Antitumour-Active Polyoxometalate from Mesoporous Silica Materials. *Dalt. Trans.* **2009**, No. 23, 4481. https://doi.org/10.1039/b901133a.

(52) Azizullah; Haider, A.; Kortz, U.; Joshi, S. A.; Iqbal, J. Polyethyleneimine-Polyoxometalate-Based Supramolecular Self-Assembled PH-Responsive Hydrogels: Formulation and in Vitro Evaluation. *ChemistrySelect* **2017**, *2* (21), 5905–5912. https://doi.org/10.1002/slct.201701003.

(53) Li, X.-H.; Chen, W.-L.; Wei, M.; Liu, J.; Di, Y.; Liu, L.; Li, Y.-G.; Wang, E.-B. Polyoxometalates Nanoparticles Improve Anti-Tumor Activity by Maximal Cellular Uptake. *Inorg. Chim. Acta* **2019**, *486*, 104–112. https://doi.org/10.1016/j.ica.2018.10.046.

(54) Yang, H. K.; Cheng, Y. X.; Su, M. M.; Xiao, Y.; Hu, M. B.; Wang, W.; Wang, Q. Polyoxometalate-Biomolecule Conjugates: A New Approach to Create Hybrid Drugs for Cancer Therapeutics. *Bioorg. Med. Chem. Lett.* **2013**, *23* (5), 1462–1466. https://doi.org/10.1016/j.bmcl.2012.12.081.

(55) Bourquin, J.; Milosevic, A.; Hauser, D.; Lehner, R.; Blank, F.; Petri-Fink, A.; Rothen-Rutishauser, B. Biodistribution, Clearance, and Long-Term Fate of Clinically Relevant Nanomaterials. *Adv. Mater.* **2018**, *30* (19), 1–31. https://doi.org/10.1002/adma.201704307.

(56) Li, H.; Jia, Y.; Wang, A.; Cui, W.; Ma, H.; Feng, X.; Li, J. Self-Assembly of Hierarchical Nanostructures from Dopamine and Polyoxometalate for Oral Drug Delivery. *Chem. - Eur. J.* **2014**, *20* (2), 499–504. https://doi.org/10.1002/chem.201302660.

(57) Cheng, L.; Wang, C.; Feng, L.; Yang, K.; Liu, Z. Functional Nanomaterials for Phototherapies of Cancer. *Chem. Rev.* **2014**, *114* (21), 10869–10939. https://doi.org/10.1021/cr400532z.

(58) Chen, J.; Ning, C.; Zhou, Z.; Yu, P.; Zhu, Y.; Tan, G.; Mao, C. Nanomaterials as Photothermal Therapeutic Agents. *Prog. Mater. Sci.* **2019**, *99*, 1–26. https://doi.org/10.1016/j.pmatsci.2018.07.005.

(59) Yong, Y.; Zhou, L.; Zhang, S.; Yan, L.; Gu, Z.; Zhang, G.; Zhao, Y. Gadolinium Polytungstate Nanoclusters: A New Theranostic with Ultrasmall Size and Versatile Properties for Dual-Modal MR/CT Imaging and Photothermal Therapy/Radiotherapy of Cancer. *NPG Asia Mater.* **2016**, *8* (5), 1–11. https://doi.org/10.1038/am.2016.63.

(60) Zhang, C.; Bu, W.; Ni, D.; Zuo, C.; Cheng, C.; Li, Q.; Zhang, L.; Wang, Z.; Shi, J. A Polyoxometalate Cluster Paradigm with Self-Adaptive Electronic Structure for Acidity/Reducibility-Specific Photothermal Conversion. *J. Am. Chem. Soc.* **2016**, *138* (26), 8156–8164. https://doi.org/10.1021/jacs.6b03375.

(61) Ni, D.; Jiang, D.; Valdovinos, H. F.; Ehlerding, E. B.; Yu, B.; Barnhart, T. E.; Huang, P.; Cai, W. Bioresponsive Polyoxometalate Cluster for Redox-Activated Photoacoustic Imaging-Guided Photothermal Cancer Therapy. *Nano Lett.* **2017**, *17* (5), 3282–3289. https://doi.org/10.1021/acs.nanolett.7b00995.

(62) Xu, J.; Han, W.; Cheng, Z.; Yang, P.; Bi, H.; Yang, D.; Niu, N.; He, F.; Gai, S.; Lin, J. Bioresponsive and near Infrared Photon Co-Enhanced Cancer Theranostic Based on Upconversion Nanocapsules. *Chem. Sci.* **2018**, *9* (12), 3233–3247. https://doi.org/10.1039/C7SC05414A.

(63) Yan, Y.; Yang, Q.; Wang, J.; Jin, H.; Wang, J.; Yang, H.; Zhou, Z.; Tian, Q.; Yang, S. Heteropoly Blue Doped Polymer Nanoparticles: An Efficient Theranostic Agent for Targeted Photoacoustic Imaging and near-Infrared Photothermal Therapy in Vivo. *J. Mater. Chem. B* **2017**, *5* (2), 382–387. https://doi.org/10.1039/C6TB02652D.

(64) Zhang, S.; Chen, H.; Zhang, G.; Kong, X.; Yin, S.; Li, B.; Wu, L. An Ultra-Small Thermosensitive Nanocomposite with a Mo 154 -Core as a Comprehensive Platform for NIR-Triggered Photothermal-Chemotherapy. *J. Mater. Chem. B* **2018**, *6* (2), 241–248. https://doi.org/10.1039/C7TB02743E.

(65) Peppas, N. A.; Slaughter, B. V.; Kanzelberger, M. A. Hydrogels. In *Polymer Science: A Comprehensive Reference*; Elsevier: Boston, MA, 2012; pp 385–395. https://doi.org/10.1016/B978-0-444-53349-4.00226-0.

(66) Zhang, Y. S.; Khademhosseini, A. Advances in Engineering Hydrogels. *Science* **2017**, *356* (6337), eaaf3627. https://doi.org/10.1126/science.aaf3627.

(67) Keplinger, C.; Sun, J.-Y.; Foo, C. C.; Rothemund, P.; Whitesides, G. M.; Suo, Z. Stretchable, Transparent, Ionic Conductors. *Science* **2013**, *341* (6149), 984–987. https://doi.org/10.1126/science.1240228.

(68) Lin, S.; Yuk, H.; Zhang, T.; Parada, G. A.; Koo, H.; Yu, C.; Zhao, X. Stretchable Hydrogel Electronics and Devices. *Adv. Mater.* **2016**, *28* (22), 4497–4505. https://doi.org/10.1002/adma.201504152.

(69) Chan, K. W. Y.; Liu, G.; Song, X.; Kim, H.; Yu, T.; Arifin, D. R.; Gilad, A. A.; Hanes, J.; Walczak, P.; Van Zijl, P. C. M.; et al. MRI-Detectable PH Nanosensors Incorporated into Hydrogels for in Vivo Sensing of Transplanted-Cell Viability. *Nat. Mater.* **2013**, *12* (3), 268–275. https://doi.org/10.1038/nmat3525.

(70) Heo, Y. J.; Shibata, H.; Okitsu, T.; Kawanishi, T.; Takeuchi, S. Long-Term in Vivo Glucose Monitoring Using Fluorescent Hydrogel Fibers. *Proc. Natl. Acad. Sci.* **2011**, *108* (33), 13399–13403. https://doi.org/10.1073/pnas.1104954108.

(71) Larson, C.; Peele, B.; Li, S.; Robinson, S.; Totaro, M.; Beccai, L.; Mazzolai, B.; Shepherd, R. Highly Stretchable Electroluminescent Skin for Optical Signaling and Tactile Sensing. *Science* **2016**, *351* (6277), 1071–1074. https://doi.org/10.1126/science.aac5082.

(72) Wang, E.; Desai, M. S.; Lee, S. W. Light-Controlled Graphene-Elastin Composite Hydrogel Actuators. *Nano Lett.* **2013**, *13* (6), 2826–2830. https://doi.org/10.1021/nl401088b.

(73) Kim, J.; Hanna, J. A.; Byun, M.; Santangelo, C. D.; Hayward, R. C. Designing Responsive Buckled Surfaces by Halftone Gel Lithography. *Science* **2012**, *335* (6073), 1201–1205. https://doi.org/10.1126/science.1215309.

(74) Burdick, J. A.; Murphy, W. L. Moving from Static to Dynamic Complexity in Hydrogel Design. *Nat. Commun.* **2012**, *3* (1), 1269. https://doi.org/10.1038/ncomms2271.

(75) Chen, C.; Liu, Y.; Wang, H.; Chen, G.; Wu, X.; Ren, J.; Zhang, H.; Zhao, Y. Multifunctional Chitosan Inverse Opal Particles for Wound Healing. *ACS Nano* **2018**, *12* (10), 10493–10500. https://doi.org/10.1021/acsnano.8b06237.

(76) Zhu, Y.; Zhang, Q.; Shi, X.; Han, D. Hierarchical Hydrogel Composite Interfaces with Robust Mechanical Properties for Biomedical Applications. *Adv. Mater.* **2019**, *1804950*, 1804950. https://doi.org/10.1002/adma.201804950.

(77) Wichterle, O.; Lím, D. Hydrophilic Gels for Biological Use. *Nature* **1960**, 185, 117–118. https://doi.org/10.1038/185117a0.

(78) Guvendiren, M.; Lu, H. D.; Burdick, J. A. Shear-Thinning Hydrogels for Biomedical Applications. *Soft Matter* **2012**, *8* (2), 260–272. https://doi.org/10.1039/C1SM06513K.

(79) Mathew, A. P.; Uthaman, S.; Cho, K. H.; Cho, C. S.; Park, I. K. Injectable Hydrogels for Delivering Biotherapeutic Molecules. *Int. J. Biol. Macromol.* **2018**, *110*, 17–29.

https://doi.org/10.1016/j.ijbiomac.2017.11.113.

(80) Yu, S.; He, C.; Chen, X. Injectable Hydrogels as Unique Platforms for Local Chemotherapeutics-Based Combination Antitumor Therapy. *Macromol. Biosci.* **2018**, *18* (12), 1–13. https://doi.org/10.1002/mabi.201800240.

(81) Mahinroosta, M.; Jomeh Farsangi, Z.; Allahverdi, A.; Shakoori, Z. Hydrogels as Intelligent Materials: A Brief Review of Synthesis, Properties and Applications. *Mater. Today Chem.* **2018**, *8*, 42–55. https://doi.org/10.1016/j.mtchem.2018.02.004.

(82) Ross-Murphy, S. B.; McEvoy, H. Fundamentals of Hydrogels and Gelation. *Br. Polym. J.* **1986**, *18* (1), 2–7. https://doi.org/10.1002/pi.4980180103.

(83) Gulrez, S. K. H.; Al-Assaf, S.; Phillips, G. O. Hydrogels: Methods of Preparation, Characterization and Applications. In *Progress in Molecular and Environmental Bioengineering - From Analysis and Modeling to Technology Applications*; Angelo Carpi (Ed.), Ed.; InTech, 2011; pp 117–150.

(84) Varaprasad, K.; Raghavendra, G. M.; Jayaramudu, T.; Yallapu, M. M.; Sadiku, R. A Mini Review on Hydrogels Classification and Recent Developments in Miscellaneous Applications. *Mater. Sci. Eng. C* **2017**, *79*, 958–971. https://doi.org/10.1016/j.msec.2017.05.096.

(85) Hu, W.; Wang, Z.; Xiao, Y.; Zhang, S.; Wang, J. Advances in Crosslinking Strategies of Biomedical Hydrogels. *Biomater. Sci.* **2019**, *7*, 843–855. https://doi.org/10.1039/c8bm01246f.

(86) Caló, E.; Khutoryanskiy, V. V. Biomedical Applications of Hydrogels: A Review of Patents and Commercial Products. *Eur. Polym. J.* **2015**, *65*, 252–267. https://doi.org/10.1016/j.eurpolymj.2014.11.024.

(87) Liu, Y.; Vrana, N. E.; Cahill, P. A.; McGuinness, G. B. Physically Crosslinked Composite Hydrogels of PVA with Natural Macromolecules: Structure, Mechanical Properties, and Endothelial Cell Compatibility. *J. Biomed. Mater. Res. Part B Appl. Biomater.* **2009**, *90B* (2), 492–502. https://doi.org/10.1002/jbm.b.31310.

(88) Schulze, J.; Hendrikx, S.; Schulz-Siegmund, M.; Aigner, A. Microparticulate Poly(Vinyl Alcohol) Hydrogel Formulations for Embedding and Controlled Release of Polyethylenimine (PEI)-Based Nanoparticles. *Acta Biomater.* **2016**, *45*, 210–222. https://doi.org/10.1016/j.actbio.2016.08.056.

(89) Hennink, W.; De Jong, S.; Bos, G.; Veldhuis, T. F.; van Nostrum, C. Biodegradable Dextran Hydrogels Crosslinked by Stereocomplex Formation for the Controlled Release of Pharmaceutical Proteins. *Int. J. Pharm.* **2004**, *277* (1–2), 99–104. https://doi.org/10.1016/j.ijpharm.2003.02.002.

(90) de Jong, S.; De Smedt, S.; Demeester, J.; van Nostrum, C.; Kettenes-van den Bosch, J.; Hennink, W. Biodegradable Hydrogels Based on Stereocomplex Formation between Lactic Acid Oligomers Grafted to Dextran. *J. Control. Release* **2001**, *72* (1–3), 47–56. https://doi.org/10.1016/S0168-3659(01)00261-9.

(91) Ishii-Mizuno, Y.; Umeki, Y.; Onuki, Y.; Watanabe, H.; Takahashi, Y.; Takakura, Y.; Nishikawa, M. Improved Sustained Release of Antigen from Immunostimulatory DNA Hydrogel by Electrostatic Interaction with Chitosan. *Int. J. Pharm.* **2017**, *516* (1–2), 392–400. https://doi.org/10.1016/j.ijpharm.2016.11.048.

(92) Masruchin, N.; Park, B.-D.; Causin, V. Influence of Sonication Treatment on Supramolecular Cellulose Microfibril-Based Hydrogels Induced by Ionic Interaction. *J. Ind. Eng. Chem.* **2015**, *29*, 265–272. https://doi.org/10.1016/j.jiec.2015.03.034.

(93) Ye, X.; Li, X.; Shen, Y.; Chang, G.; Yang, J.; Gu, Z. Self-Healing PH-Sensitive Cytosine- and Guanosine-Modified Hyaluronic Acid Hydrogels via Hydrogen Bonding. *Polymer* **2017**, *108*, 348–360. https://doi.org/10.1016/j.polymer.2016.11.063.

(94) Feng, W.; Zhou, W.; Dai, Z.; Yasin, A.; Yang, H. Tough Polypseudorotaxane Supramolecular Hydrogels with Dual-Responsive Shape Memory Properties. *J. Mater. Chem. B* **2016**, *4* (11), 1924–1931. https://doi.org/10.1039/C5TB02737C.

(95) Bai, X.; Lü, S.; Cao, Z.; Gao, C.; Duan, H.; Xu, X.; Sun, L.; Gao, N.; Feng, C.; Liu, M. Self-Reinforcing Injectable Hydrogel with Both High Water Content and Mechanical Strength for Bone Repair. *Chem. Eng. J.* **2016**, *288*, 546–556. https://doi.org/10.1016/j.cej.2015.12.021.

(96) Buitrago, J. O.; Patel, K. D.; El-Fiqi, A.; Lee, J.-H.; Kundu, B.; Lee, H.-H.; Kim, H.-W. Silk Fibroin/Collagen Protein Hybrid Cell-Encapsulating Hydrogels with Tunable Gelation and Improved Physical and Biological Properties. *Acta Biomater.* **2018**, *69*, 218–233. https://doi.org/10.1016/j.actbio.2017.12.026.

(97) Parhi, R. Cross-Linked Hydrogel for Pharmaceutical Applications: A Review. *Adv. Pharm. Bull.* **2017**, *7* (4), 515–530. https://doi.org/10.15171/apb.2017.064.

(98) Hennik, W. E.; van Nostrum, C. F. Novel Crosslinking Methods to Design Hydrogels. *Adv. Drug Deliv. Rev.* **2002**, *54*, 13–36. https://doi.org/10.1016/0022-2836(75)90369-1.

(99) Villanueva-Flores, F.; Miranda-Hernández, M.; Flores-Flores, J. O.; Porras-Sanjuanico, A.; Hu, H.; Pérez-Martínez, L.; Ramírez, O. T.; Palomares, L. A. Poly(Vinyl Alcohol Co-Vinyl Acetate) as a Novel Scaffold for Mammalian Cell Culture and Controlled Drug Release. *J. Mater. Sci.* **2019**, *54* (10), 7867–7882.

https://doi.org/10.1007/s10853-019-03402-1.

(100) Chen, X.; Fan, M.; Tan, H.; Ren, B.; Yuan, G.; Jia, Y.; Li, J.; Xiong, D.; Xing, X.; Niu, X.; et al. Magnetic and Self-Healing Chitosan-Alginate Hydrogel Encapsulated Gelatin Microspheres via Covalent Cross-Linking for Drug Delivery. *Mater. Sci. Eng. C* **2019**, *101*, 619–629. https://doi.org/10.1016/j.msec.2019.04.012.

(101) Jayaramudu, T.; Raghavendra, G. M.; Varaprasad, K.; Raju, K. M.; Sadiku, E. R.; Kim, J. 5-Fluorouracil Encapsulated Magnetic Nanohydrogels for Drug-Delivery Applications. *J. Appl. Polym. Sci.* **2016**, *133* (37), 1–10. https://doi.org/10.1002/app.43921.

(102) Varaprasad, K.; Mohan, Y. M.; Ravindra, S.; Reddy, N. N.; Vimala, K.; Monika, K.; Sreedhar, B.; Raju, K. M. Hydrogel-Silver Nanoparticle Composites: A New Generation of Antimicrobials. *J. Appl. Polym. Sci.* **2010**, *115* (2), 1199–1207. https://doi.org/10.1002/app.31249.

(103) Jin, R.; Moreira Teixeira, L. S.; Dijkstra, P. J.; Van Blitterswijk, C. A.; Karperien, M.; Feijen, J. Chondrogenesis in Injectable Enzymatically Crosslinked Heparin/Dextran Hydrogels. *J. Control. Release* **2011**, *152* (1), 186–195. https://doi.org/10.1016/j.jconrel.2011.01.031.

(104) Kuo, K. C.; Lin, R. Z.; Tien, H. W.; Wu, P. Y.; Li, Y. C.; Melero-Martin, J. M.; Chen, Y. C. Bioengineering Vascularized Tissue Constructs Using an Injectable Cell-Laden Enzymatically Crosslinked Collagen Hydrogel Derived from Dermal Extracellular Matrix. *Acta Biomater.* **2015**, *27* (521), 151–166. https://doi.org/10.1016/j.actbio.2015.09.002.

(105) Ajji, Z.; Mirjalili, G.; Alkhatab, A.; Dada, H. Use of Electron Beam for the Production of Hydrogel Dressings. *Radiat. Phys. Chem.* **2008**, *77* (2), 200–202. https://doi.org/10.1016/j.radphyschem.2007.05.016.

(106) Tu, Y.; Chen, N.; Li, C.; Liu, H.; Zhu, R.; Chen, S.; Xiao, Q.; Liu, J.; Ramakrishna, S.; He, L. Advances in Injectable Self-Healing Biomedical Hydrogels. *Acta Biomater.* **2019**, *90*, 1–20. https://doi.org/10.1016/j.actbio.2019.03.057.

(107) Xu, Y.; Li, Y.; Chen, Q.; Fu, L.; Tao, L.; Wei, Y. Injectable and Self-Healing Chitosan Hydrogel Based on Imine Bonds : Design and Therapeutic Applications. *Int. J. Mol. Sci.* **2018**, *19*, 2198. https://doi.org/10.3390/ijms19082198.

(108) Wei, Z.; Hai Yang, J.; Zhou, J.; Xu, F.; Zrínyi, M.; H. Dussault, P.; Osada, Y.; Mei Chen, Y. Self-Healing Gels Based on Constitutional Dynamic Chemistry and Their Potential Applications. *Chem. Soc. Rev.* **2014**, *43*, 8114–8131. https://doi.org/10.1039/C4CS00219A.

(109) Tuncaboylu, D. C.; Sahin, M.; Argun, A.; Oppermann, W.; Okay, O. Dynamics and Large Strain Behavior of Self-Healing Hydrogels with and without Surfactants. *Macromolecules* **2012**, *45*, 1991–2000. https://doi.org/10.1021/ma202672y.

(110) South, A. B.; Lyon, L. A. Autonomic Self-Healing of Hydrogel Thin Films. *Angew. Chemie - Int. Ed.* **2010**, *49*, 767–771. https://doi.org/10.1002/anie.200906040.

(111) Zhang, H.; Xia, H.; Zhao, Y. Poly(Vinyl Alcohol) Hydrogel Can Autonomously Self-Heal. *ACS Macro Lett.* **2012**, *1*, 1233–1236. https://doi.org/https://doi.org/10.1021/mz300451r.

(112) Xu, Y.; Wu, Q.; Sun, Y.; Bai, H.; Shi, G. Three-Dimensional Self-Assembly of Graphene Oxide and DNA into Multifunctional Hydrogels. *ACS Nano* **2010**, *4* (12), 7358–7362.

(113) Harrington, M. J.; Masic, A.; Holten-Andersen, N.; Waite, J. H.; Fratzl, P. Iron-Clad Fibers : A Metal-Based Biological Strategy for Hard Flexible Coatings. *Science* **2010**, *328*, 216–220. https://doi.org/10.1126/science.1181044.

(114) Qu, J.; Zhao, X.; Ma, P. X.; Guo, B. PH-Responsive Self-Healing Injectable Hydrogel Based on N -Carboxyethyl Chitosan for Hepatocellular Carcinoma Therapy. *Acta Biomater.* **2017**, *58*, 168–180. https://doi.org/10.1016/j.actbio.2017.06.001.

(115) Canadell, J.; Goossens, H.; Klumperman, B. Self-Healing Materials Based on Disulfide Links. *Macromolecules* **2011**, *44* (8), 2536–2541. https://doi.org/10.1021/ma2001492.

(116) Deng, G.; Tang, C.; Li, F.; Jiang, H.; Chen, Y. Covalent Cross-Linked Polymer Gels with Reversible Sol - Gel Transition and Self-Healing Properties. *Macromolecules* **2010**, *43* (3), 1191–1194. https://doi.org/10.1021/ma9022197.

(117) Oehlenschlaeger, K. K.; Mueller, J. O.; Brandt, J.; Hilf, S.; Lederer, A.; Wilhelm, M.; Graf, R.; Coote, M. L.; Schmidt, F. G.; Barner-kowollik, C. Adaptable Hetero Diels – Alder Networks for Fast Self-Healing under Mild Conditions. *Adv. Mater.* **2014**, *26* (21), 3561–3566. https://doi.org/10.1002/adma.201306258.

(118) Amamoto, Y.; Otsuka, H.; Takahara, A.; Matyjaszewski, K. Self-Healing of Covalently Cross-Linked Polymers by Reshuffl Ing Thiuram Disulfi de Moieties in Air under Visible Light. *Adv. Mater.* **2012**, *24* (29), 3975–3980. https://doi.org/10.1002/adma.201201928.

(119) He, L.; E. Fullenkamp, D.; G. Rivera, J.; B. Messersmith, P. PH Responsive Self-Healing Hydrogels Formed by Boronate – Catechol Complexation. *ChemComm* **2011**, *47*, 7497–7499. https://doi.org/10.1039/c1cc11928a.

(120) Buwalda, S. J.; Vermonden, T.; Hennink, W. E. Hydrogels for Therapeutic Delivery:

Current Developments and Future Directions. *Biomacromolecules* **2017**, *18* (2), 316–330. https://doi.org/10.1021/acs.biomac.6b01604.

(121) Liu, Y.; Hsu, S. Synthesis and Biomedical Applications of Self-Healing Hydrogels. *Front. Chem.* **2018**, *6*, 1–10. https://doi.org/https://www.frontiersin.org/articles/10.3389/fchem.2018.00449/full.

(122) Fan, H.; Wang, J.; Jin, Z. Tough, Swelling-Resistant, Self-Healing, and Adhesive Dual-Cross-Linked Hydrogels Based on Polymer-Tannic Acid Multiple Hydrogen Bonds. *Macromolecules* **2018**, *51* (5), 1696–1705. https://doi.org/10.1021/acs.macromol.7b02653.

(123) Lin, P.; Ma, S.; Wang, X.; Zhou, F. Molecularly Engineered Dual-Crosslinked Hydrogel with Ultrahigh Mechanical Strength, Toughness, and Good Self-Recovery. *Adv. Mater.* **2015**, *27* (12), 2054–2059. https://doi.org/10.1002/adma.201405022.

(124) Dutta, A.; Das, R. K. Dual Cross-Linked Hydrogels with High Strength, Toughness, and Rapid Self-Recovery Using Dynamic Metal–Ligand Interactions. *Macromol. Mater. Eng.* **2019**, *1900195*, 1900195. https://doi.org/10.1002/mame.201900195.

(125) Li, X.; Zhao, Y.; Li, D.; Zhang, G.; Long, S.; Wang, H. Hybrid Dual Crosslinked Polyacrylic Acid Hydrogels with Ultrahigh Mechanical Strength, Toughness and Self-Healing Properties via Soaking Salt Solution. *Polymer* **2017**, *121*, 55–63. https://doi.org/10.1016/j.polymer.2017.05.070.

(126) Antony, R.; Arun, T.; Manickam, S. T. D. A Review on Applications of Chitosan-Based Schiff Bases. *Int. J. Biol. Macromol.* **2019**, *129*, 615–633. https://doi.org/10.1016/j.ijbiomac.2019.02.047.

(127) Khan, S.; Ullah, A.; Ullah, K.; Rehman, N. U. Insight into Hydrogels. *Des. Monomers Polym.* **2016**, *19* (5), 456–478. https://doi.org/10.1080/15685551.2016.1169380.

(128) Wang, Y.; Adokoh, C. K.; Narain, R. Recent Development and Biomedical Applications of Self-Healing Hydrogels. *Expert Opin. Drug Deliv.* **2018**, *15* (1), 77–91. https://doi.org/http://dx.doi.org/10.1080/17425247.2017.1360865.

(129) Traitel, T.; Goldbart, R.; Kost, J. Smart Polymers for Responsive Drug-Delivery Systems. *J. Biomater. Sci. Polym. Ed.* **2008**, *19* (6), 755–767. https://doi.org/10.1163/156856208784522065.

(130) Rahikkala, A.; Pereira, S. A. P.; Figueiredo, P.; Passos, M. L. C.; Araújo, A. R. T. S.; Saraiva, M. L. M. F. S.; Santos, H. A. Mesoporous Silica Nanoparticles for Targeted and Stimuli-Responsive Delivery of Chemotherapeutics: A Review. *Adv. Biosyst.* **2018**, *2* (7), 1800020. https://doi.org/10.1002/adbi.201800020.

(131) Costa, D. F.; Mendes, L. P.; Torchilin, V. P. The Effect of Low- and High-Penetration

Light on Localized Cancer Therapy. *Adv. Drug Deliv. Rev.* **2019**, *138*, 105–116. https://doi.org/10.1016/j.addr.2018.09.004.

(132) Saneja, A.; Kumar, R.; Arora, D.; Kumar, S.; Panda, A. K.; Jaglan, S. Recent Advances in Near-Infrared Light-Responsive Nanocarriers for Cancer Therapy. *Drug Discov. Today* **2018**, *23* (5), 1115–1125. https://doi.org/10.1016/j.drudis.2018.02.005.

(133) Qiao, Y.; Wan, J.; Zhou, L.; Ma, W.; Yang, Y.; Luo, W.; Yu, Z.; Wang, H. Stimuli-Responsive Nanotherapeutics for Precision Drug Delivery and Cancer Therapy. *Wiley Interdiscip. Rev. Nanomedicine Nanobiotechnology* **2019**, *11* (1), e1527. https://doi.org/10.1002/wnan.1527.

(134) Raza, A.; Hayat, U.; Rasheed, T.; Bilal, M.; Iqbal, H. M. N. “Smart” Materials-Based near-Infrared Light-Responsive Drug Delivery Systems for Cancer Treatment: A Review. *J. Mater. Res. Technol.* **2019**, *8* (1), 1497–1509. https://doi.org/10.1016/j.jmrt.2018.03.007.

(135) Ward, M. A.; Georgiou, T. K. Thermoresponsive Polymers for Biomedical Applications. *Polymers* **2011**, *3*, 1215–1242. https://doi.org/10.3390/polym3031215.

(136) Sánchez-Moreno, P.; de Vicente, J.; Nardecchia, S.; Marchal, J.; Boulaiz, H. Thermo-Sensitive Nanomaterials: Recent Advance in Synthesis and Biomedical Applications. *Nanomaterials* **2018**, *8* (11), 935. https://doi.org/10.3390/nano8110935.

(137) Klouda, L.; Mikos, A. G. Thermoresponsive Hydrogels in Biomedical Applications. *Eur. J. Pharm. Biopharm.* **2008**, *68* (1), 34–45. https://doi.org/10.1016/j.ejpb.2007.02.025.

(138) Scherzinger, C.; Schwarz, A.; Bardow, A.; Leonhard, K.; Richtering, W. Cononsolvency of Poly-N-Isopropyl Acrylamide (PNIPAM): Microgels versus Linear Chains and Macrogels. *Curr. Opin. Colloid Interface Sci.* **2014**, *19* (2), 84–94. https://doi.org/10.1016/j.cocis.2014.03.011.

(139) Bordat, A.; Boissenot, T.; Nicolas, J.; Tsapis, N. Thermoresponsive Polymer Nanocarriers for Biomedical Applications. *Adv. Drug Deliv. Rev.* **2019**, *138*, 167–192. https://doi.org/10.1016/j.addr.2018.10.005.

(140) Chatterjee, S.; Hui, P. C. L.; Kan, C. wai. Thermoresponsive Hydrogels and Their Biomedical Applications: Special Insight into Their Applications in Textile Based Transdermal Therapy. *Polymers* **2018**, *10* (5), 480. https://doi.org/10.3390/polym10050480.

(141) Wagner, A. M.; Spencer, D. S.; Peppas, N. A. Advanced Architectures in the Design of Responsive Polymers for Cancer Nanomedicine. *J. Appl. Polym. Sci.* **2018**, *135*

(24), 46154. https://doi.org/10.1002/app.46154.

(142) Mo, R.; Gu, Z. Tumor Microenvironment and Intracellular Signal-Activated Nanomaterials for Anticancer Drug Delivery. *Mater. Today* **2016**, *19* (5), 274–283. https://doi.org/10.1016/j.mattod.2015.11.025.

(143) Mura, S.; Nicolas, J.; Couvreur, P. Stimuli-Responsive Nanocarriers for Drug Delivery. *Nat. Mater.* **2013**, *12* (11), 991–1003. https://doi.org/10.1038/nmat3776.

(144) Taghizadeh, B.; Taranejoo, S.; Monemian, S. A.; Moghaddam, Z. S.; Daliri, K.; Derakhshankhah, H.; Derakhshani, Z. Classification of Stimuli-Responsive Polymers as Anticancer Drug Delivery Systems. *Drug Deliv.* **2015**, *22* (2), 145–155. https://doi.org/10.3109/10717544.2014.887157.

(145) de Lima, G. G.; Kanwar, D.; Macken, D.; Geever, L.; Devine, D. M.; Nugent, M. J. D. Smart Hydrogels: Therapeutic Advancements in Hydrogel Technology for Smart Drug Delivery Applications. In *Handbook of Polymers for Pharmaceutical Technologies*; Thakur, V. K., Thakur, M. K., Eds.; Scrivener Publishing LLC, 2016; Vol. 4, pp 1–16. https://doi.org/10.1002/9781119041559.ch1.

(146) Traitel, T.; Kost, J. PH-Responsive Hydrogels: Swelling Model. In *Biomaterials. Advances in Experimental Medicine and Biology*; N., H., Hasirci, V., Eds.; Springer, Boston, MA, 2004; pp 29–43. https://doi.org/10.1007/978-0-306-48584-8_3.

(147) Qian, C.; Zhang, T.; Gravesande, J.; Baysah, C.; Song, X.; Xing, J. Injectable and Self-Healing Polysaccharide-Based Hydrogel for PH-Responsive Drug Release. *Int. J. Biol. Macromol.* **2019**, *123*, 140–148. https://doi.org/10.1016/j.ijbiomac.2018.11.048.

(148) Sharma, P. K.; Taneja, S.; Singh, Y. Hydrazone-Linkage-Based Self-Healing and Injectable Xanthan-Poly(Ethylene Glycol) Hydrogels for Controlled Drug Release and 3D Cell Culture. *ACS Appl. Mater. Interfaces* **2018**, *10* (37), 30936–30945. https://doi.org/10.1021/acsami.8b07310.

(149) Rizwan, M.; Yahya, R.; Hassan, A.; Yar, M.; Azzahari, A. D.; Selvanathan, V.; Sonsudin, F.; Abouloula, C. N. PH Sensitive Hydrogels in Drug Delivery: Brief History, Properties, Swelling, and Release Mechanism, Material Selection and Applications. *Polymers* **2017**, *9* (4), 137. https://doi.org/10.3390/polym9040137.

(150) Rinaudo, M. Chitin and Chitosan: Properties and Applications. *Prog. Polym. Sci.* **2006**, *31* (7), 603–632. https://doi.org/10.1016/j.progpolymsci.2006.06.001.

(151) Alves, N. M.; Mano, J. F. Chitosan Derivatives Obtained by Chemical Modifications for Biomedical and Environmental Applications. *Int. J. Biol. Macromol.* **2008**, *43* (5), 401–414. https://doi.org/10.1016/j.ijbiomac.2008.09.007.

(152) Baldrick, P. The Safety of Chitosan as a Pharmaceutical Excipient. *Regul. Toxicol. Pharmacol.* **2010**, *56* (3), 290–299. https://doi.org/10.1016/j.yrtph.2009.09.015.

(153) Kean, T.; Thanou, M. Biodegradation, Biodistribution and Toxicity of Chitosan. *Adv. Drug Deliv. Rev.* **2010**, *62* (1), 3–11. https://doi.org/10.1016/j.addr.2009.09.004.

(154) Bellich, B.; D'Agostino, I.; Semeraro, S.; Gamini, A.; Cesàro, A. *"The Good, the Bad and the Ugly" of Chitosans*; 2016; Vol. 14. https://doi.org/10.3390/md14050099.

(155) Argüelles-Monal, W.; Recillas-Mota, M.; Fernández-Quiroz, D. Chitosan-Based Thermosensitive Materials. In *Biological Activities and Application of Marine Polysaccharides*; InTech, 2017; pp 279–302. https://doi.org/10.5772/65713.

(156) Jiao, J.; Huang, J.; Zhang, Z. Hydrogels Based on Chitosan in Tissue Regeneration: How Do They Work? A Mini Review. *J. Appl. Polym. Sci.* **2019**, *136* (13), 1–9. https://doi.org/10.1002/app.47235.

(157) Liu, S.-W.; Wang, L.; Lin, M.; Liu, Y.; Zhang, L.-N.; Zhang, H. Tumor Photothermal Therapy Employing Photothermal Inorganic Nanoparticles/Polymers Nanocomposites. *Chin. J. Polym. Sci.* **2019**, *37* (2), 115–128. https://doi.org/10.1007/s10118-019-2193-4.

(158) Liu, Y.; Bhattarai, P.; Dai, Z.; Chen, X. Photothermal Therapy and Photoacoustic Imaging: Via Nanotheranostics in Fighting Cancer. *Chem. Soc. Rev.* **2019**, *48* (7), 2053–2108. https://doi.org/10.1039/c8cs00618k.

(159) Chen, J.; Ning, C.; Zhou, Z.; Yu, P.; Zhu, Y.; Tan, G.; Mao, C. Nanomaterials as Photothermal Therapeutic Agents. *Prog. Mater. Sci.* **2019**, *99*, 1–26. https://doi.org/10.1016/j.pmatsci.2018.07.005.

(160) van der Zee, J. Heating the Patient: A Promising Approach? *Ann. Oncol.* **2002**, *13* (8), 1173–1184. https://doi.org/10.1093/annonc/mdf280.

(161) Streffer, C. Molecular and Cellular Mechanisms of Hyperthermia. In *Thermoradiotherapy and Thermochemotherapy. Medical Radiology (Diagnostic Imaging and Radiation Oncology)*; Seegenschmiedt, M. H., Fessenden, P., Vernon, C. C., Eds.; Springer Berlin Heidelberg, 1995; pp 47–74. https://doi.org/10.1007/978-3-642-57858-8_2.

(162) Evans, S. S.; Repasky, E. A.; Fisher, D. T. Fever and the Thermal Regulation of Immunity: The Immune System Feels the Heat. *Nat. Rev. Immunol.* **2015**, *15* (6), 335–349. https://doi.org/10.1038/nri3843.

(163) Das, S. K.; Krickemeyer, E.; Kuhlmann, C.; Dickman, M. H.; Pope, M. T. *Inorganic Syntheses*; Darensbourg, M. Y., Ed.; Inorganic Syntheses; John Wiley & Sons, Inc.: Hoboken, NJ, USA, 1998; Vol. 32. https://doi.org/10.1002/9780470132630.

(164) Mu, M.; Li, X.; Tong, A.; Guo, G. Multi-Functional Chitosan-Based Smart Hydrogels Mediated Biomedical Application. *Expert Opin. Drug Deliv.* **2019**, *16* (3), 239–250. https://doi.org/10.1080/17425247.2019.1580691.

(165) Duan, C.; Zhang, D.; Wang, F.; Zheng, D.; Jia, L.; Feng, F.; Liu, Y.; Wang, Y.; Tian, K.; Wang, F.; et al. Chitosan-g-Poly(N-Isopropylacrylamide) Based Nanogels for Tumor Extracellular Targeting. *Int. J. Pharm.* **2011**, *409* (1–2), 252–259. https://doi.org/10.1016/j.ijpharm.2011.02.050.

(166) Weinhold, M. X.; Sauvageau, J. C. M.; Keddig, N.; Matzke, M.; Tartsch, B.; Grunwald, I.; Kübel, C.; Jastorff, B.; Thöming, J. Strategy to Improve the Characterization of Chitosan for Sustainable Biomedical Applications: SAR Guided Multi-Dimensional Analysis. *Green Chem.* **2009**, *11* (4), 498–509. https://doi.org/10.1039/b809941c.

(167) Vårum, K. M.; Antohonsen, M. W.; Grasdalen, H.; Smidsrød, O. Determination of the Degree of N-Acetylation and the Distribution of N-Acetyl Groups in Partially N-Deacetylated Chitins (Chitosans) by High-Field N.M.R. Spectroscopy. *Carbohydr. Res.* **1991**, *211* (1), 17–23. https://doi.org/10.1016/0008-6215(91)84142-2.

(168) Bao, H.; Li, L.; Leong, W. C.; Gan, L. H. Thermo-Responsive Association of Chitosan-Graft -Poly(N -Isopropylacrylamide) in Aqueous Solutions. *J. Phys. Chem. B* **2010**, *114* (32), 10666–10673. https://doi.org/10.1021/jp105041z.

(169) Jadhav, S. A.; Brunella, V.; Miletto, I.; Berlier, G.; Scalarone, D. Synthesis of Poly N-Isopropylacrylamide) by Distillation Precipitation Polymerization and Quantitative Grafting on Mesoporous Silica. *J. Appl. Polym. Sci.* **2016**, *133* (44), 1–8. https://doi.org/10.1002/app.44181.

(170) Queiroz, M. F.; Melo, K. R. T.; Sabry, D. A.; Sassaki, G. L.; Rocha, H. A. O. Does the Use of Chitosan Contribute to Oxalate Kidney Stone Formation? *Mar. Drugs* **2015**, *13* (1), 141–158. https://doi.org/10.3390/md13010141.

(171) Song, C.; Yu, H.; Zhang, M.; Yang, Y.; Zhang, G. Physicochemical Properties and Antioxidant Activity of Chitosan from the Blowfly Chrysomya Megacephala Larvae. *Int. J. Biol. Macromol.* **2013**, *60*, 347–354. https://doi.org/10.1016/j.ijbiomac.2013.05.039.

(172) Erbil, C.; Kazancioğlu, E.; Uyanik, N. Synthesis, Characterization and Thermoreversible Behaviours of Poly(Dimethyl Siloxane)/Poly(N-Isopropyl Acrylamide) Semi-Interpenetrating Networks. *Eur. Polym. J.* **2004**, *40* (6), 1145–1154. https://doi.org/10.1016/j.eurpolymj.2003.12.024.

(173) Seddiki, N.; Aliouche, D. Synthesis, Rheological Behavior and Swelling Properties of Copolymer Hydrogels Based on Poly(n-Isopropylacrylamide) with Hydrophilic

Monomers. *Bull. Chem. Soc. Ethiop.* **2013**, *27* (3), 447–457. https://doi.org/10.4314/bcse.v27i3.14.

(174) Alvarez-Lorenzo, C.; Concheiro, A.; Dubovik, A. S.; Grinberg, N. V.; Burova, T. V.; Grinberg, V. Y. Temperature-Sensitive Chitosan-Poly(N-Isopropylacrylamide) Interpenetrated Networks with Enhanced Loading Capacity and Controlled Release Properties. *J. Control. Release* **2005**, *102* (3), 629–641. https://doi.org/10.1016/j.jconrel.2004.10.021.

(175) Zhang, Q.; Weber, C.; Schubert, U. S.; Hoogenboom, R. Thermoresponsive Polymers with Lower Critical Solution Temperature: From Fundamental Aspects and Measuring Techniques to Recommended Turbidimetry Conditions. *Mater. Horizons* **2017**, *4* (2), 109–116. https://doi.org/10.1039/c7mh00016b.

(176) Ujhelyi, Z.; Vecsernyés, M.; Fehér, P.; Kósa, D.; Arany, P.; Nemes, D.; Sinka, D.; Vasvári, G.; Fenyvesi, F.; Váradi, J.; et al. Physico-Chemical Characterization of Self-Emulsifying Drug Delivery Systems. *Drug Discov. Today Technol.* **2018**, *27*, 81–86. https://doi.org/10.1016/j.ddtec.2018.06.005.

(177) Bao, H.; Li, L.; Leong, W. C.; Gan, L. H. Thermo-Responsive Association of Chitosan-Graft -Poly (N-Isopropylacrylamide) in Aqueous Solutions. *J. Phys. Chem. B* **2010**, *114*, 10666–10673.

(178) Chen, C.; Liu, M.; Gao, C.; Lü, S.; Chen, J.; Yu, X.; Ding, E.; Yu, C.; Guo, J.; Cui, G. A Convenient Way to Synthesize Comb-Shaped Chitosan-Graft-Poly (N-Isopropylacrylamide) Copolymer. *Carbohydr. Polym.* **2013**, *92* (1), 621–628. https://doi.org/10.1016/j.carbpol.2012.09.014.

(179) Echeverria, C.; Soares, P.; Robalo, A.; Pereira, L.; Novo, C. M. M.; Ferreira, I.; Borges, J. P. One-Pot Synthesis of Dual-Stimuli Responsive Hybrid PNIPAAm-Chitosan Microgels. *Mater. Des.* **2015**, *86*, 745–751. https://doi.org/10.1016/j.matdes.2015.07.170.

(180) Chen, J. P.; Cheng, T. H. Thermo-Responsive Chitosan-Graft-Poly(N-Isopropylacrylamide) Injectable Hydrogel for Cultivation of Chondrocytes and Meniscus Cells. *Macromol. Biosci.* **2006**, *6* (12), 1026–1039. https://doi.org/10.1002/mabi.200600142.

(181) Lutz, J. F.; Weichenhan, K.; Akdemir, Ö.; Hoth, A. About the Phase Transitions in Aqueous Solutions of Thermoresponsive Copolymers and Hydrogels Based on 2-(2-Methoxyethoxy)Ethyl Methacrylate and Oligo(Ethylene Glycol) Methacrylate. *Macromolecules* **2007**, *40* (7), 2503–2508. https://doi.org/10.1021/ma062925q.

(182) Berger, J.; Reist, M.; Mayer, J. M.; Felt, O.; Peppas, N. A.; Gurny, R. Structure and

Interactions in Covalently and Ionically Crosslinked Chitosan Hydrogels for Biomedical Applications. *Eur. J. Pharm. Biopharm.* **2004**, *57* (1), 19–34. https://doi.org/10.1016/S0939-6411(03)00161-9.

(183) Giri, T. K.; Thakur, A.; Alexander, A.; Ajazuddin; Badwaik, H.; Tripathi, D. K. Modified Chitosan Hydrogels as Drug Delivery and Tissue Engineering Systems: Present Status and Applications. *Acta Pharm. Sin. B* **2012**, *2* (5), 439–449. https://doi.org/10.1016/j.apsb.2012.07.004.

(184) Oryan, A.; Kamali, A.; Moshiri, A.; Baharvand, H.; Daemi, H. Chemical Crosslinking of Biopolymeric Scaffolds: Current Knowledge and Future Directions of Crosslinked Engineered Bone Scaffolds. *Int. J. Biol. Macromol.* **2018**, *107* (PartA), 678–688. https://doi.org/10.1016/j.ijbiomac.2017.08.184.

(185) Murata-Kamiya, N.; Kamiya, H.; Kaji, H.; Kasai, H. Glyoxal, a Major Product of DNA Oxidation, Induces Mutations at G:C Sites on a Shuttle Vector Plasmid Replicated in Mammalian Cells. *Nucleic Acids Res.* **1997**, *25* (10), 1897–1902. https://doi.org/10.1093/nar/25.10.1897.

(186) Morgan, K. T.; Clarke, D. O.; Beauchamp, R. O.; St Clair, M. B. G.; Fennell, T. R.; Karl, F. W. A Critical Review of the Toxicology of Glutaraldehyde. *Crit. Rev. Toxicol.* **2008**, *22* (3–4), 143–174. https://doi.org/10.3109/10408449209145322.

(187) Takigawa, T.; Endo, Y. Effects of Glutaraldehyde Exposure on Human Health. *J. Occup. Health* **2006**, *48*, 75–87. https://doi.org/10.1539/joh.48.75.

(188) Veronese, F. M.; Pasut, G. PEGylation, Successful Approach to Drug Delivery. *Drug Discov. Today* **2005**, *10* (21), 1451–1458. https://doi.org/10.1016/S1359-6446(05)03575-0.

(189) Knop, K.; Hoogenboom, R.; Fischer, D.; Schubert, U. S. Poly(Ethylene Glycol) in Drug Delivery: Pros and Cons as Well as Potential Alternatives. *Angew. Chemie - Int. Ed.* **2010**, *49* (36), 6288–6308. https://doi.org/10.1002/anie.200902672.

(190) Zhang, Y.; Tao, L.; Li, S.; Wei, Y. Synthesis of Multiresponsive and Dynamic Chitosan-Based Hydrogels for Controlled Release of Bioactive Molecules. *Biomacromolecules* **2011**, *12* (8), 2894–2901. https://doi.org/10.1021/bm200423f.

(191) Anacona, J. R.; Marquez, V. E.; Jimenez, Y. Synthesis and Characterization of Manganese(II), Nickel(II), Copper(II) and Zinc(II) Schiff-Base Complexes Derived from 1,10-Phenanthroline-2,9- Dicarboxaldehyde and 2-Mercaptoethylamine. *J. Coord. Chem.* **2009**, *62* (7), 1172–1179. https://doi.org/10.1080/00958970802382768.

(192) Dust, J. M.; Fang, Z. H.; Harris, J. M. Proton NMR Characterization of Poly(Ethylene

Glycols) and Derivatives. *Macromolecules* **1990**, *23* (16), 3742–3746. https://doi.org/10.1021/ma00218a005.

(193) Shameli, K.; Ahmad, M. Bin; Jazayeri, S. D.; Sedaghat, S.; Shabanzadeh, P.; Jahangirian, H.; Mahdavi, M.; Abdollahi, Y. Synthesis and Characterization of Polyethylene Glycol Mediated Silver Nanoparticles by the Green Method. *Int. J. Mol. Sci.* **2012**, *13*, 6639–6650. https://doi.org/10.3390/ijms13066639.

(194) Milichovsky, M. Water—A Key Substance to Comprehension of Stimuli-Responsive Hydrated Reticular Systems. *J. Biomater. Nanobiotechnol.* **2010**, *01* (01), 17–30. https://doi.org/10.4236/jbnb.2010.11003.

(195) Yan, Y.; Huang, L.; Zhang, Q.; Zhou, H. Concentration Effect on Aggregation and Dissolution Behavior of Poly(N-Isopropylacrylamide) in Water. *J. Appl. Polym. Sci.* **2015**, *132* (12), 1–8. https://doi.org/10.1002/app.41669.

(196) Zuidema, J. M.; Rivet, C. J.; Gilbert, R. J.; Morrison, F. A. A Protocol for Rheological Characterization of Hydrogels for Tissue Engineering Strategies. *J. Biomed. Mater. Res. Part B Appl. Biomater.* **2014**, *102* (5), 1063–1073. https://doi.org/10.1002/jbm.b.33088.

(197) Ghosh, K.; Shu, X. Z.; Mou, R.; Lombardi, J.; Prestwich, G. D.; Rafailovich, M. H.; Clark, R. A. F. Rheological Characterization of in Situ Cross-Linkable Hysluronan Hydrogels. *Biomacromolecules* **2005**, *6* (5), 2857–2865. https://doi.org/10.1021/bm050361c.

(198) Zhang, Y.; Fu, C.; Li, Y.; Wang, K.; Wang, X.; Wei, Y.; Tao, L. Synthesis of an Injectable, Self-Healable and Dual Responsive Hydrogel for Drug Delivery and 3D Cell Cultivation. *Polym. Chem.* **2017**, *8* (3), 537–544. https://doi.org/10.1039/c6py01704e.

(199) Huang, W.; Wang, Y.; Chen, Y.; Zhao, Y.; Zhang, Q.; Zheng, X.; Chen, L.; Zhang, L. Strong and Rapidly Self-Healing Hydrogels: Potential Hemostatic Materials. *Adv. Healthc. Mater.* **2016**, *5* (21), 2813–2822. https://doi.org/10.1002/adhm.201600720.

(200) Yang, L.; Li, Y.; Gou, Y.; Wang, X.; Zhao, X.; Tao, L. Improving Tumor Chemotherapy Effect Using an Injectable Self-Healing Hydrogel as Drug Carrier. *Polym. Chem.* **2017**, *8* (34), 5071–5076. https://doi.org/10.1039/c7py00112f.

(201) A Basic Introduction to Rheology - Malvern Instruments. **2016**.

(202) Ding, F.; Wu, S.; Wang, S.; Xiong, Y.; Li, Y.; Li, B.; Deng, H.; Du, Y.; Xiao, L.; Shi, X. A Dynamic and Self-Crosslinked Polysaccharide Hydrogel with Autonomous Self-Healing Ability. *Soft Matter* **2015**, *11* (20), 3971–3976.

https://doi.org/10.1039/c5sm00587f.

(203) National Center for Biotechnology Information. PubChem Database. Doxorubicin, CID=31703 https://pubchem.ncbi.nlm.nih.gov/compound/Doxorubicin (accessed Aug 26, 2019).

(204) Shin, B.; Kim, J.; Vales, T. P.; Yang, S. K.; Kim, J. K.; Sohn, H.; Kim, H. J. Thermoresponsive Drug Controlled Release from Chitosan-Based Hydrogel Embedded with Poly(N-Isopropylacrylamide) Nanogels. *J. Polym. Sci. Part A Polym. Chem.* **2018**, *56* (17), 1907–1914. https://doi.org/10.1002/pola.29073.

(205) Garrett, W. S.; Mellman, I. Studies of Endocytosis. In *Dendritic Cells: Biology and Clinical Applications*; Lotze, M., Thomson, A., Eds.; Academic Press, 2001; pp 213–229. https://doi.org/10.1016/B978-0-12-455851-9.50055-9.

(206) Veitch, N. C. Horseradish Peroxidase : A Modern View of a Classic Enzyme. *Phytochemistry* **2004**, *65*, 249–259. https://doi.org/10.1016/j.phytochem.2003.10.022.

(207) Ribatti, D. The Discovery of the Blood–Thymus Barrier. In *Milestones in Immunology*; Ribatti, D., Ed.; Elsevier, 2017; pp 37–46. https://doi.org/10.1016/B978-0-12-811313-4.00003-6.

(208) Ritthidej, G. C. Nasal Delivery of Peptides and Proteins with Chitosan and Related Mucoadhesive Polymers. In *Peptide and Protein Delivery*; Walle, C. Van Der, Ed.; Elsevier, 2011; pp 47–68. https://doi.org/10.1016/B978-0-12-384935-9.10003-3.

(209) Cooperstein, M. A.; Canavan, H. E. Assessment of Cytotoxicity of (N-Isopropyl Acrylamide) and Poly(N-Isopropyl Acrylamide)-Coated Surfaces. *Biointerphases* **2013**, *8* (1), 1–12. https://doi.org/10.1186/1559-4106-8-19.

(210) Liu, C.; Ruan, C.; Shi, R.; Jiang, B.; Ji, S.; Shen, X. A near Infrared-Modulated Thermosensitive Hydrogel for Stabilization of Indocyanine Green and Combinatorial Anticancer Phototherapy. *Biomater. Sci.* **2019**, *7*, 1705–1715. https://doi.org/10.1039/c8bm01541d.

(211) Ruan, C.; Liu, C.; Hu, H.; Guo, X.; Jiang, B.; Liang, H.; Shen, X. NIR-II Light-Modulated Thermosensitive Hydrogel for Light-Triggered Cisplatin Release and Repeatable Chemo-Photothermal Therapy. *Chem. Sci.* **2019**, *10*, 4699–4706. https://doi.org/10.1039/c9sc00375d.

(212) Fu, J.; Wu, B.; Wei, M.; Huang, Y.; Zhou, Y.; Zhang, Q.; Du, L. Prussian Blue Nanosphere-Embedded in Situ Hydrogel for Photothermal Therapy by Peritumoral Administration. *Acta Pharm. Sin. B* **2019**, *9* (3), 604–614. https://doi.org/10.1016/j.apsb.2018.12.005.

(213) Wang, C.; Wang, X.; Dong, K.; Luo, J.; Zhang, Q.; Cheng, Y. Injectable and Responsively Degradable Hydrogel for Personalized Photothermal Therapy. *Biomaterials* **2016**, *104*, 129–137. https://doi.org/10.1016/j.biomaterials.2016.07.013.

(214) Nanobiotechnol, J.; Fu, J.; Chen, M.; Li, J.; Zhou, J.; Xie, S.; Yuan, P.; Tang, B. Injectable Hydrogel Encapsulating - Cu 2 MnS 2 Nanoplates for Photothermal Therapy against Breast Cancer. *J. Nanobiotechnol.* **2018**, *16* (83), 1–15. https://doi.org/https://doi.org/10.1186/s12951-018-0409-3.

(215) Stieger, M. The Rheology Handbook - For Users of Rotational and Oscillatory Rheometers. *Appl. Rheol.* **2002**, *12* (5), 232–232. https://doi.org/10.1515/arh-2002-0029.

(216) Präbst, K.; Engelhardt, H.; Ringgeler, S.; Hübner, H. Basic Colorimetric Proliferation Assays: MTT, WST, and Resazurin. In *Cell Viability Assays*; Gilbert, D. F., Friedrich, O., Eds.; Methods in Molecular Biology; Springer New York: New York, NY, 2017; Vol. 1601, pp 1–18. https://doi.org/10.1007/978-1-4939-6960-9.

(217) Rodríguez-Corrales, J. Á.; Josan, J. S. Resazurin Live Cell Assay: Setup and Fine-Tuning for Reliable Cytotoxicity Results. In *Proteomics for Drug Discovery: Methods and Protocols*; Lazar, I. M., Ed.; Springer Science+Business Media, 2017; Vol. 1647, pp 207–219. https://doi.org/10.1007/978-1-4939-7201-2_14.

(218) Aslantürk, Ö. S. In Vitro Cytotoxicity and Cell Viability Assays: Principles, Advantages, and Disadvantages. In *Genotoxicity - A Predictable Risk to Our Actual World*; Larramendy, M. L., Soloneski, S., Eds.; InTech, 2018; Vol. i, p 13. https://doi.org/10.5772/intechopen.71923.

7. Appendix

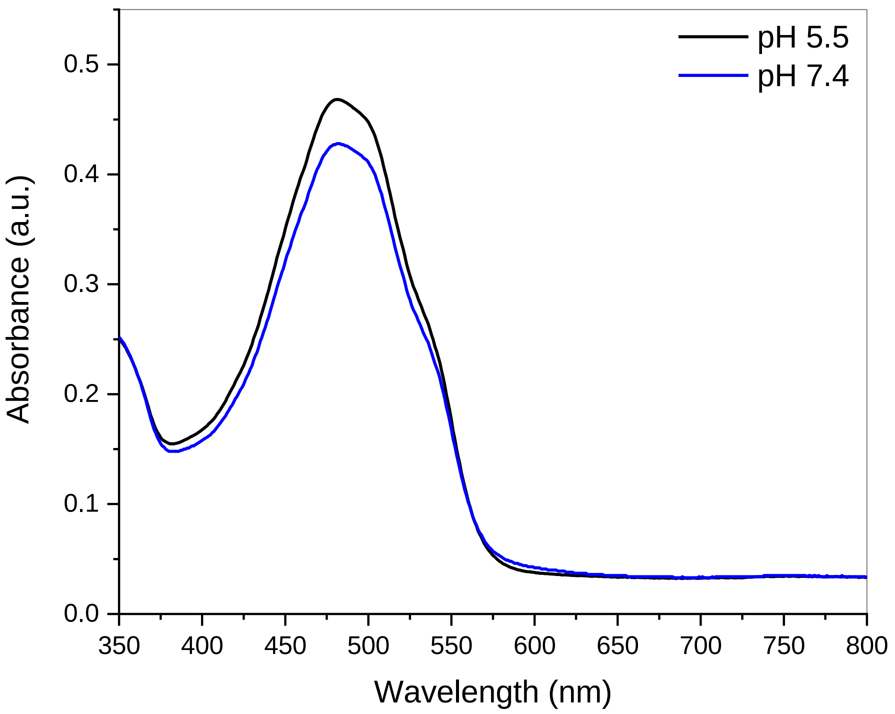

Appendix 1 – UV-Vis spectra of DOX aqueous solution with pH 5.5 and 7.4.

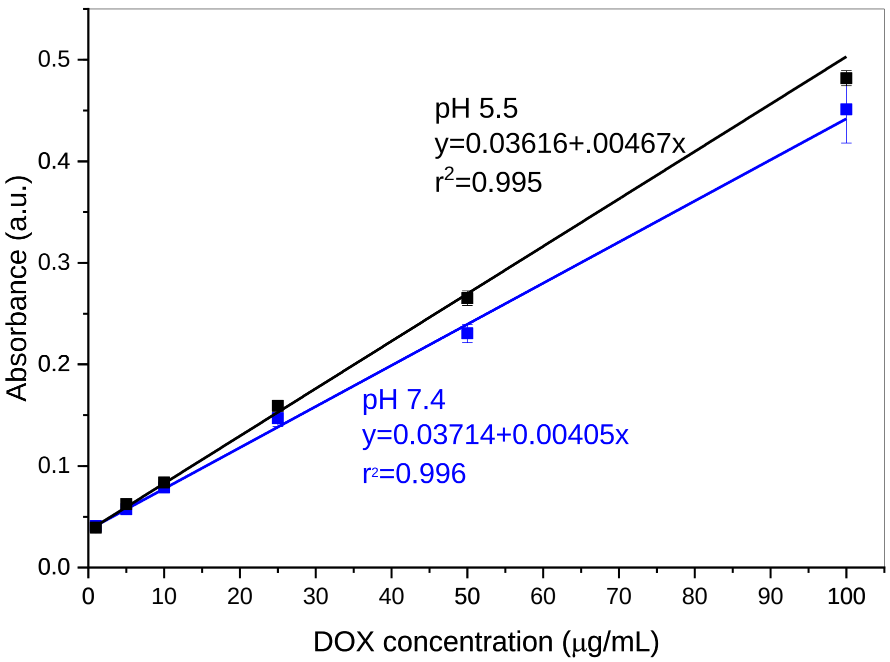

Appendix 2 – DOX calibration curve obtained by measurement of the absorbance at pH 5.5 (black) and 7.4 (blue).

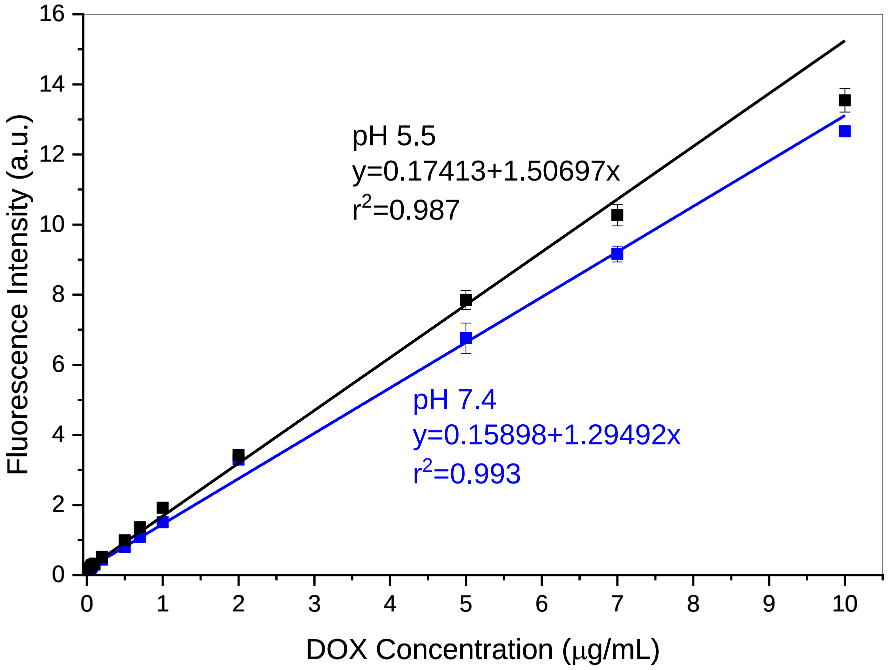

Appendix 3 – DOX calibration curve obtained by measurement of the fluorescence at pH 5.5 (black) and 7.4 (blue).

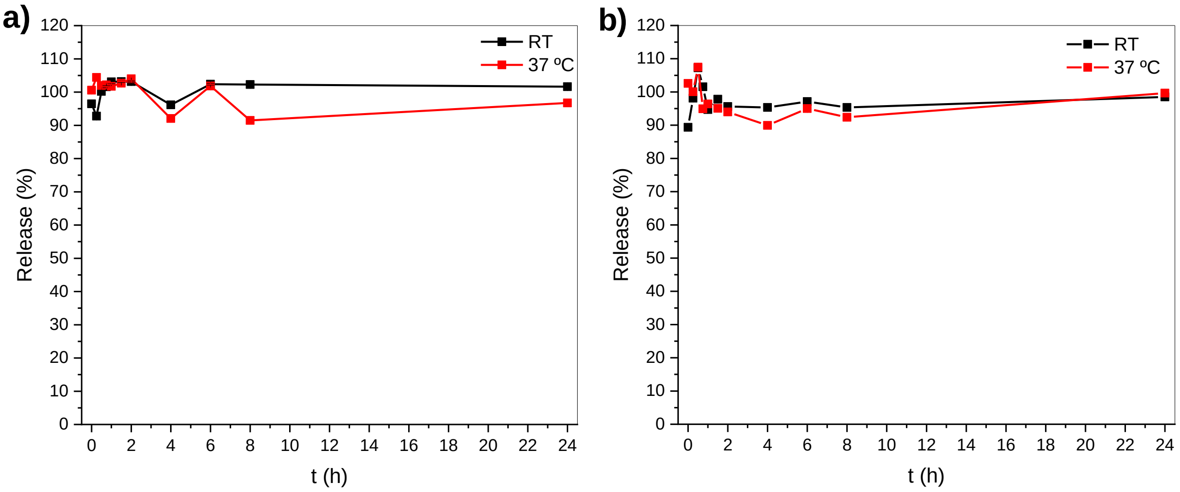

Appendix 4 – In vitro DOX release profiles from DOX solutions (controls) at a) pH 7.4 and b) pH 5.5, and different temperatures (RT and 37 ºC).

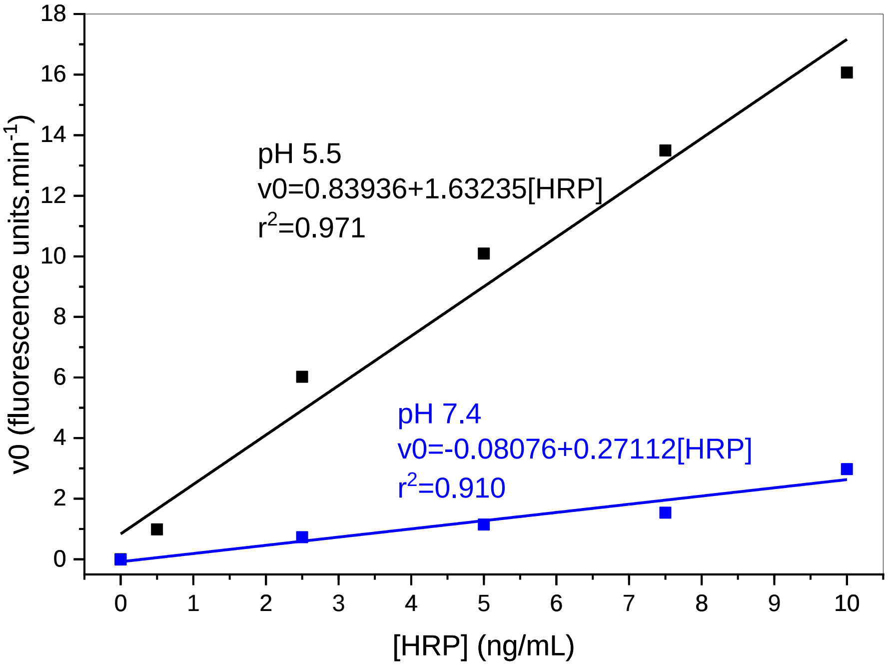

Appendix 5 – HRP calibration curve obtained from the relation between v0 and HRP concentration deduced from the Michaelis-Menten equation, at pH 5.5 (black) and 7.4 (blue).

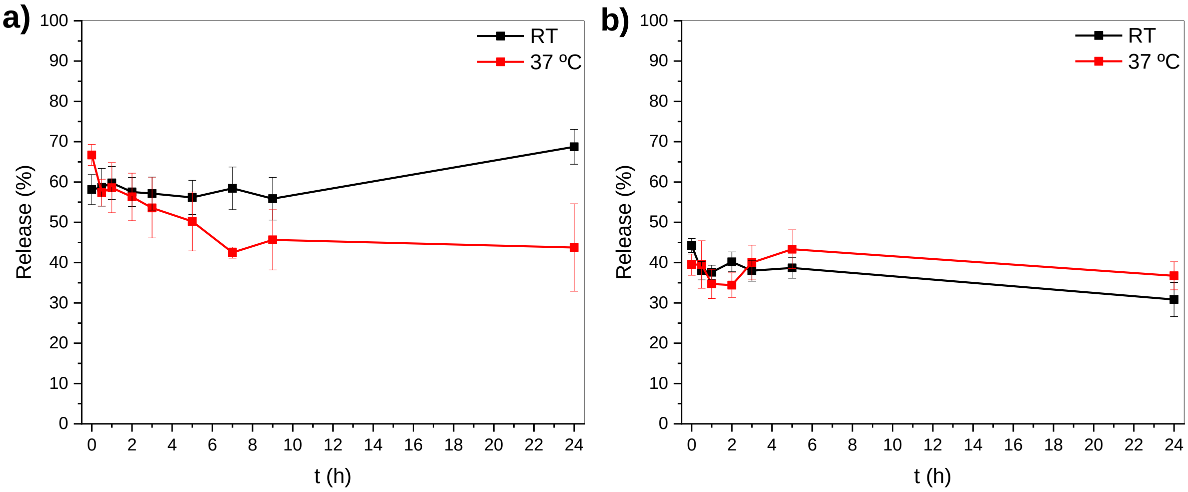

Appendix 6 – In vitro HRP release profiles from HRP solutions (controls) at a) pH 7.4 and b) pH 5.5, and different temperatures (RT and 37 ºC).